Structural Investigation of *Plasmodium falciparum* Chloroquine Resistance Transporter in the Context of Anti-Malarial Drug Resistance

Jonathan Kim

Submitted in partial fulfillment of the
requirements for the degree of
Doctor of Philosophy
in the Graduate School of Arts and Sciences

COLUMBIA UNIVERSITY

2019

ABSTRACT

Structural Investigation of *Plasmodium falciparum* Chloroquine Resistance Transporter in the Context of Anti-Malarial Drug Resistance

Jonathan Kim

Malaria is a mosquito borne infectious disease caused by a unicellular Apicomplexan parasite of the *Plasmodia* genus. The emergence and subsequent spread of drug resistance in the highly virulent *Plasmodium falciparum* parasite has been a major setback in eradicating malaria, which affects an estimated 216 million individuals and causes 445,000 deaths annually worldwide. Chloroquine (CQ) was once used as the first-line antimalarial drug treatment, until CQ-resistant parasites emerged in endemic regions including Africa, Southeast Asia, and South America. More recently, parasites have developed resistance to the current first line drug piperaquine (PPQ), used in combination with dihydroartemisinin (DHA) in Southeast Asia.

Plasmodium falciparum chloroquine resistance transporter (PfCRT), a member of the drug/metabolite transporter (DMT) superfamily, is a 49-kDa integral transmembrane protein localized in the digestive vacuole (DV) of the pathogenic parasite. Mutations in PfCRT have been identified as the core determinants of Plasmodium falciparum resistance to CQ and PPQ by mediating the efflux of these antimalarial drugs. All CQ resistance-conferring PfCRT isoforms share the K76T mutation, which is widely used as a molecular marker for CQ resistance. Despite the significance in the impact of drug-resistant malaria, a detailed understanding of PfCRT physiological function and the molecular basis of PfCRT-mediated drug resistance have been hampered by a lack of high-resolution structural information. This dissertation describes the first structure of PfCRT and reveals the interaction of drugs with the purified and reconstituted protein.

We determined the structure of the 49-kDa PfCRT 7G8, a clinically relevant CQ-resistant isoform found in South America, to 3.2 Å resolution by single-particle cryo-electron microscopy (cryo-EM), in complex with a specific antigen-binding fragment (Fab) to overcome current size limitations in cryo-EM. Our PfCRT structure displays an inward-open conformation, consists of 10 transmembrane (TM) helices with an inverted topology, and has unique elements including two juxtamembrane helices and a highly conserved cysteine-rich loop between TM helix 7 and 8. The architecture of PfCRT is similar to other members of the DMT superfamily. TM helices 1-4 and 6-9 in PfCRT form a central cavity which is a potential binding site for both CQ and PPQ. A striking feature is that virtually all the CQ resistance mutations, identified from decades of investigation into PfCRT variants that have evolved independently across the malaria-endemic world, map around this central, negatively-charged cavity. Distinct mutations that have been proposed to cause high-level PPQ resistance in parasites, which cause a loss of CQ resistance, form a planar ring that also lines this cavity. Functional experiments with various purified PfCRT isoforms or mutants provide evidence that drug resistance is possibly due to pH- and membrane potential-dependent drug transport. We also show that PfCRT CQ-resistant isoforms bind and transport arginine, suggesting that positively charged amino acids may be putative transport substrates for CQ-resistant PfCRT. This work provides a structural and functional framework to understand the mechanism of PfCRT-mediated drug resistance in the malaria parasite.

TABLE OF CONTENTS

LIST OF FIGURES iv

LIST OF TABLES vi

ACKNOWLEDGEMENTS vii

DEDICATION x

CHAPTER 1

MALARIA: BACKGROUND AND SIGNIFICANCE 1

1.1 Introduction 1

1.2 The *Plasmodium* Life Cycle and its relationship to Human Diseases 3

1.3 The Digestive vacuole 5

1.4 Antimalarial drugs 6

1.4.1 4-aminoquinolines 6

1.4.2 Chloroquine 7

1.4.3 Artemisinin-based Combination Therapies (ACTs) 8

1.5 *Plasmodium falciparum* Chloroquine Resistance Transporter PfCRT 12

1.6 Significant work presented in this dissertation 15

References 16

CHAPTER 2

MEMBRANE PROTEIN STRUCTURE 20

2.1 Membrane protein: Introduction 20

2.2 Structural Determination Technique: Single-Particle Cryo-Electron Microscopy (Cryo-EM) 23

2.2.1 Sample preparation 23

2.2.2 Sample Vitrification 24

2.2.3 Imaging 24

2.2.4 Reconstruction 25

References 26

CHAPTER 3

STRUCTURAL ELUCIDATION OF PfCRT 7G8 29

3.1 Introduction 29

3.2 Expression Screen of Chloroquine Resistance Transporter (CRT) Variants 30

3.3 Detergent and Stability Screen of PfCRT 7G8 34

3.4 Reconstitution of PfCRT 7G8 into Nanodiscs 35

3.5 Structural Elucidation of PfCRT 7G8 36

References 38

Structure of the Plasmodium falciparum Pleiotropic Drug Resistance Transporter PfCRT 39

CHAPTER 4

ON-GOING STUDIES AND FUTURE DIRECTIONS 76

4.1 Introduction 76

4.2 Investigating the physiological function of PfCRT 76

4.3 Elucidating the mechanism of PfCRT-mediated drug resistance..... 79

4.4 Determining the structures of PfCRT 7G8 in complex with CQ and PPQ..... 81

4.5 Determining the structure of PfCRT 7G8 in other conformations 85

4.6 Conclusions..... 86

References 86

LIST OF FIGURES

Figure 1.1 Incidence of Malaria 2

Figure 1.2 The *Plasmodium* Life Cycle..... 4

Figure 1.3 Hemoglobin degradation in the digestive vacuole of the asexual blood stage *Plasmodium* parasite 6

Figure 1.4 The mechanism of 4-aminoquinoline action in the digestive vacuole (DV) of asexual blood stage (ABS) parasite 8

Figure 1.5 Chemical structures of Artemisinin derivatives and partner drugs..... 10

Figure 1.6 Recent reductions in the global malaria burden since 2000 12

Figure 1.7 Topology of PCRT and location of residues involved in chloroquine (CQ) or piperaquine (PPQ) drug resistance phenotypes..... 13

Figure 2.1 Membrane protein structural determination over time 21

Figure 2.2 Structure determination workflow by single particle cryo-EM 26

Figure 3.1 Schematic representation of COMPPÅ pipeline..... 30

Figure 3.2 Expression and detergent stability screens of CRT variants..... 32

Figure 3.3 PfCRT 7G8 expression optimization 33

Figure 3.4 Detergent Screen for PfCRT 7G8..... 35

Figure 3.5 Schematic representation of nanodisc assembly 36

Figure 4.1 Substrates of PfCRT 7G8 isoform 78

Figure 4.2 Purification of PfCRT variants..... 80

Figure 4.3 PfCRT variants uptake assay 81

Figure 4.4 PfCRT 7G8 complex with PTC Fabs in the presence of drugs 82

Figure 4.5 Competition binding assay between CQ and mouse monoclonal antibody Fabs 83

Figure 4.6 Cryo-EM analysis of the PfCRT+3H10 Fab complex 84

LIST OF TABLES

Table 1.1 Features of antimalarial drugs 7

Table 1.2 Current Artemisinin-based Combination Therapies (ACTs) for Clinical Use 11

Table 1.3 Core PfCRT haplotypes in Southeast Asia, Africa and South America 14

Table 3.1 CRT variants cloned and tested for expression 31

ACKNOWLEDGEMENTS

First, I would like to thank my advisor, Dr. Filippo Mancia, for his invaluable mentorship and training. He has led me into and guided me through the field of structural biology of membrane proteins and has provided me with an admirable scientific environment where my intellectual growth has been enabled and I have learned the value of collaboration. Filippo inspired me with the confidence and encouragement to endure and embrace the scientific challenges throughout this project. He stimulated me to think like a scientist and taught me how to be resilient in solving the intricacies and complexities of the field of study. I have come to appreciate the time, trust, and laugh we have shared together during my time in his lab. I am truly grateful for everything that he has done for me during my Ph.D. career. His energy and passion towards science will continue be an immeasurable source of motivation and persistence in my future career.

I am sincerely indebted to my thesis committee: Dr. Wayne Hendrickson, Dr. David Fidock, Dr. Matthias Quick, and Dr. Oliver Clarke. I am privileged to have Dr. Wayne Hendrickson on my committee and for his encouragement and expertise. His pioneer work and contribution in the field of structural biology is tremendously inspiring for the younger generation including myself. I would like to thank Dr. David Fidock, a pioneer in malaria research, whose discovery of the mutations in PfCRT that mediate drug resistance paved the path for me to pursue my studies on this particular molecule. I was fortunate to work side-by-side with David and have obtained invaluable knowledge of PfCRT from him. I thank Dr. Matthias Quick for his support and guidance in collaborating on this project, and for his valuable time and sharing expertise for the functional experiments. I have gained a substantial amount of

knowledge and understanding in the mechanism of transport from the meetings with Matthias. Last but not least, I thank Dr. Oliver Clarke for his enthusiasm and guidance in cryo-EM data processing and analyses for this project.

I was fortunate to be a part of the structural biology community at Columbia University in New York City. I would like to thank everyone in the Center on Membrane Protein Production and Analysis (COMPPÅ) and the Simons Electron Microscopy Center (SEMC) at the New York Structural Biology Center (NYSBC), especially Dr. Bridget Carragher, Dr. Clint Potter, Dr. Brian Kloss, Dr. Renato Bruni, Dr. Ravi Kalathur, Dr. Ed Eng, Dr. Bill Rice, Laura Kim, and Dr. Venkat Dandey.

I would also like to thank all the collaborators who made this project even more exciting. I thank Dr. Anthony Kossiakoff and Dr. Satchal Erramilli from University of Chicago who have generated a PfCRT-specific Fab that was essential in allowing us to determine the structure of PfCRT using cryo-EM. I thank Dr. Kathryn Wicht, Dr. Satish Dhingra, Dr. John Okombo and Laura Hagenah from the Fidock Lab at Columbia University. I also thank Audrey Warren from the Quick Lab at Columbia University. I also had the pleasure of working with Dr. Jeremie Vendome who has been an excellent and optimistic collaborator on this project.

I would like to thank everyone, both past and present, from the Russ Berrie 5th floor and the Department of Physiology and Cellular Biophysics, including Dr. Andrew Marks, Dr. Henry Colecraft, Castalia Sanchez, Karen Allis, Matthew Wallace, Janice Savage, Dawn LaSalle and Dionida Ryce. Thanks to all my fellow Physiology graduate students, especially Dr. John Smerdon and Dr. Mike Holsey.

Special shout out to my high school buddies from New Jersey (arguably the best state in the United States), and friends from Syracuse/NYC/Korea. I would like to thank C with my upmost sincerity for being an immense support and strength, and for making me breathe during

the toughest time of my Ph.D. career. Also, I would like to thank K-town for supplying me with enough alcoholic beverages for me to survive throughout my time as a graduate student at Columbia University.

I was gifted with a wonderful group of people and would like to thank the entire #ManciaLab family for all the supports, psychotherapy sessions, gossips, drama, chocolates, cakes and laughs, making my Ph.D. the best time of my life. I would not have been able to do this without you guys. I thank the past members: Dr. Yunting Chen, Dr. Guiliano Sciara, Sabrina Giacometti, Dr. Meagan Dufrisne, Dr. Vasileios Petrou, Dr. Zahra Assur, Dr. Chiara Ardiccioni, David Tomasek, Minah Kim, Dr. Rushelle Byfield, Dr. Jessica Chukwu, and Dr. Francis Insaidoo. I thank the present members, Dr. Yong Zi Tan, Dr. Rie Nygaard, Dr. Rosemary Cater, Brianna Costabile, Dr. Khuram Ashraf, Dr. Giacomo Parisi, Dr. Yaqi Liu, and Brendon Choy. I would like to thank our best lab manager, Leora Hamberger-Elliot, and the Romans, Dr. Beatrice Vallone, Dr. Linda Montemiglio, Gabriele Cerutti, and Silvia Corradi.

Lastly, I would like to thank my family for their unconditional love and support throughout my studies. I wouldn't be where I am today without my family. Thank you.

To my family.

Chapter 1 MALARIA: BACKGROUND AND SIGNIFICANCE

1.1 Introduction

Malaria is a life-threatening infectious disease that has co-evolved with humans over the course of history. The disease has affected an estimated 216 million individuals, disproportionately children, and causes 445,000 deaths annually worldwide - making it a major public health concern [1]. While malaria is most prevalent in sub-Saharan Africa, it also occurs in other endemic regions including Southeast Asia, Central, and South America (**Fig. 1.1**) [2]. Evidence of malaria fever can be found as early as 2700 BC in ancient Chinese documents, however, our understanding of the disease and its causes have radically shifted over the past two millennia.

Initially, malaria was attributed to miasmas - foul or poisonous vapors - from swamps. In fact, the word malaria is derived from the medieval Italian term “mal aria”, which means "bad air." However, in 1676, Antonie van Leeuwenhoek's observations and discoveries of protozoa using a single-lensed light microscope set the pretext for new ways to understand disease from the emerging perspective of microbiology. In the late 1870s, Louis Pasteur and Robert Koch developed and provided evidence for the germ theory of disease, hypothesizing that unseen microorganisms were disease causing agents, and their discoveries paved the way for more thorough investigations into the biological causes of malaria [3]. In 1880, a French military physician Charles Louis Alphonse Lavern discovered various parasitic protozoans that cause disease in humans, including those that give rise to malaria [4]. In 1897, Ronald Ross, a British-Indian medical scientist, found malarial parasites in the mosquito salivary gland and demonstrated that malarial parasites can be transmitted from mosquitoes to birds, identifying the

mosquito to be a vector for disease transmission [5]. At around the same time, Giovanni Battista Grassi, an Italian physician and zoologist, and his colleagues described the transmission of malaria parasite to humans [3]. These discoveries laid the groundwork for understanding the interactions between the parasite and mosquito vectors that affect the transmission of the malaria parasite into humans [6]. Today, five species of unicellular Apicomplexa parasites of the Plasmodium genus have been identified to infect humans and cause malaria including *P. falciparum, P. vivax, P. malariae, P. ovale and P. knowlesi.* Among these, *P. falciparum* is the most virulent species, leading to the highest number of casualties [1]. Genetic studies have demonstrated that essential *P. falciparum* genes were highly conserved across *Plasmodium* species suggesting as the potential therapeutic targets [7-9].

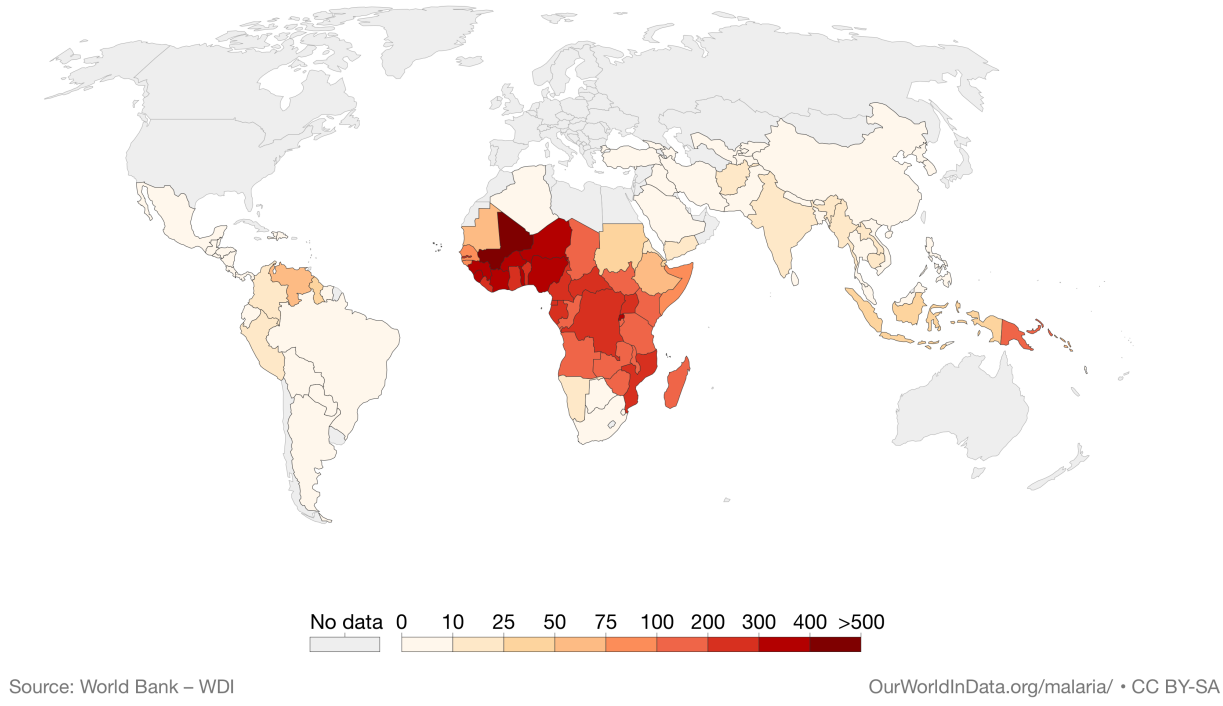

Figure 1.1 Incidence of Malaria. The map demonstrates the number of malaria cases per 1,000 people across the world. Figure adapted from World Bank (https://ourworldindata.org/grapher/incidence-of-

malaria). Among endemic regions, the highest number of malaria cases occurs in Africa (88%) followed by Southeast Asia (10%), Eastern Mediterranean region (2%) and Central to South America (<1%) [2].

1.2 The *Plasmodium* Life Cycle and its relationship to Human Diseases

The transmission of *Plasmodium* parasites occurs when an infected female *Anopheles* mosquito bites and feeds on blood from humans, simultaneously releasing parasites in the form of sporozoites into the bloodstream of its new host [10]. These sporozoites migrate to the host's liver within hours and rapidly invade hepatocytes. The sporozoites multiply and mature into merozoites, which in turn burst the hepatocytes and are released into the host's circulatory system. The merozoites then invade red blood cells (RBCs) initiating a 48-hour intraerythrocytic, asexual cycle inside a parasitophorous vacuole (PV) (**Fig. 1.2**) [11]. During the asexual blood stage (ABS), the parasite undergoes three developing stages: ring (0 to 24 hours post invasion), trophozoite (24 to 36 hours post invasion) and schizont (40 to 48 hours post invasion). At the end of the cycle, one merozoite has replicated into 16-32 daughter merozoites. These merozoites rupture the RBC membranes and are released back into circulation where each new merozoite infects a new RBC and repeats the cycle [12, 13]. The lysing of RBCs every 48 hours during the ABS cycle leads to the clinical symptoms experienced by malaria patients such as fever, chill, sweat and fatigue [14]. Fatalities can occur once the patient reaches hyper-parasitemia, meaning 5% or greater of all RBCs in the body are infected, leading to hemolytic anemia. Patients can also develop cerebral malaria, thought to be caused by parasitized RBCs sequestered in the brain. Cerebral malaria leads to intracranial swelling, respiratory arrest, coma, and often death [14, 15]. Because the majority of disease symptoms derive from parasite replication in the ABS, all current anti-malarials target this point of the parasite life cycle.

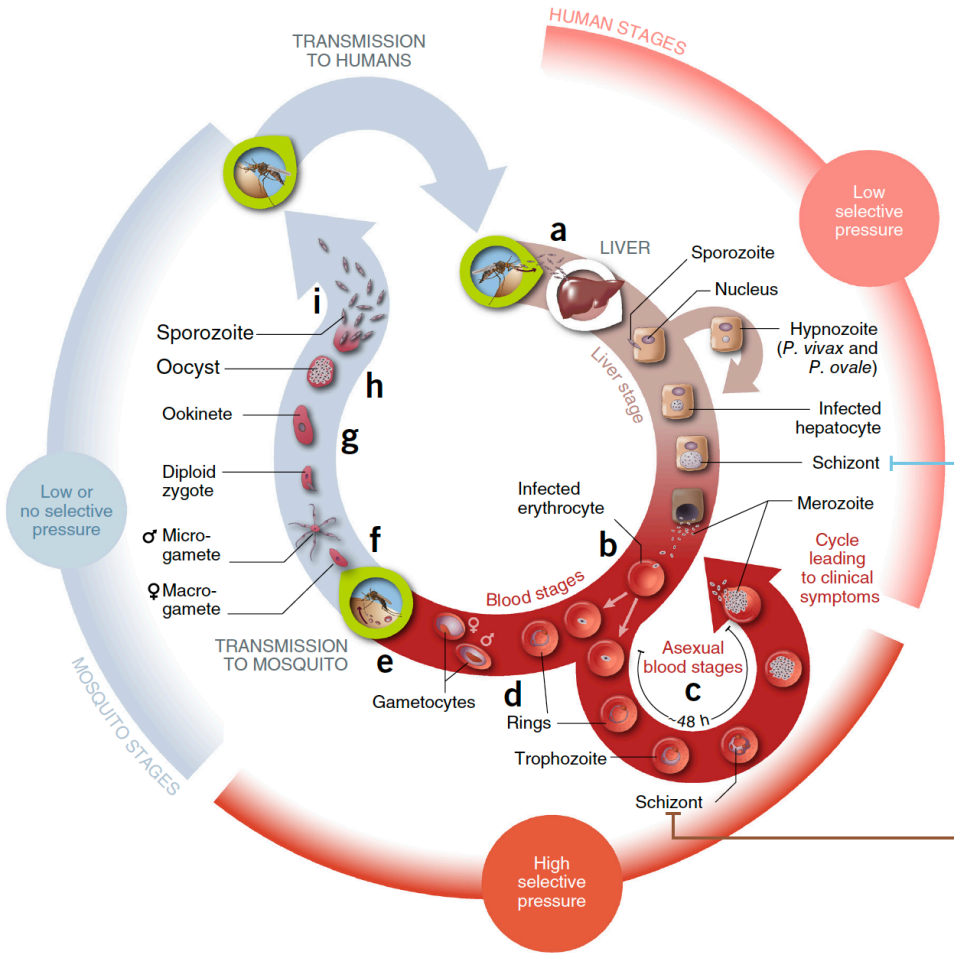

Figure 1.2 The *Plasmodium* Life Cycle. (a-d) Female *Anopheles* mosquito releases sporozoites (the motile form of malaria parasite) during blood feeding. The sporozoites invade hepatocytes, maturing into merozoites that are then released back into circulation where they infect red blood cells (RBCs) and multiply as asexual blood stages (ABS) inside a parasitophorous vacuole (PV). **(e-i)** Sexual development takes approximately 10 to 12 days for the maturation of both male and female gametocytes which in turn are ingested by *Anopheles* female mosquito during blood feeding. Once in the mosquito, the gametocytes undergo meiotic and mitotic replication to produce 10^3-10^4 sporozoites which migrate to salivary glands and can infect another human host.

While the majority of parasites in the body exist in the ABS, approximately 1-2% of intraerythrocytic parasites undergo a sexual development, in which they mature to male and female gametocytes that can be ingested by *Anopheles* female mosquitoes during blood feeding (**Fig. 1.2**) [11, 12]. Gametocytes are an essential bridge between the human host and the mosquito vector to facilitate the transmission of *Plasmodium*. Once ingested by the mosquito

host, male and female gametocytes fuse in the gut of the mosquito and undergo genetic recombination in the salivary glands of the mosquito, resulting in the production of sporozoites that can be transmitted to a new human host (**Fig. 1.2**).

1.3 The Digestive vacuole

At the start of the intraerythrocytic asexual cycle, the parasite forms a parasitophorous vacuole (PV) within the human red blood cell to enclose and protect it from the host immune system. *Plasmodium* exports hundreds of proteins across the parasitophorous vacuolar membrane (PVM) into the cytosol of host RBCs. The exported *Plasmodium* proteins of the malaria parasite interact with proteins of the RBC membrane to remodel both the morphological structure and the function of the host RBC to promote survival of the parasite [13, 16]. To facilitate its maturation within the PV, the parasite takes up a large portion of the host cell cytosol and forms an acidic organelle called the digestive vacuole (DV). The formation of the DV begins during the mid-ring stage when the cytosol of the host erythrocyte is internalized via cytostome-mediated invagination resulting in a double-membrane vesicles between the PVM and the plasma membrane (PPM) in the parasite cytosol [17]. Acidification occurs immediately, as a V-type H^+-ATPase and a H^+-pyrophosphatase, transferred from the PPM to the DV membrane via endocytosis, begin to pump protons into the DV [17, 18]. During the trophozoite stage, the DV further matures and increases in size.

A main function of the DV is to carry out the important catabolic process of hemoglobin (Hb) degradation. The parasite has a limited ability to synthesize its own amino acids and therefore must obtain these molecules from its host for protein synthesis and survival. It does this during the intraerythrocytic asexual stage by breaking down host Hb in the acidic environment of

the DV. This provides the parasite with all the essential amino acids, except isoleucine (which is obtained from an exogenous source in the host cell) [19, 20]. However, this essential process also results in a toxic by-product, free heme (or iron protoporphyrin IX), which can destabilize the vacuolar membrane and trigger oxidative stress [11, 21]. Heme is detoxified in the DV by forming the chemically inert molecule hemozoin – a crystal lattice of dimeric heme (β-hematin) (**Fig. 1.3**) [22, 23].

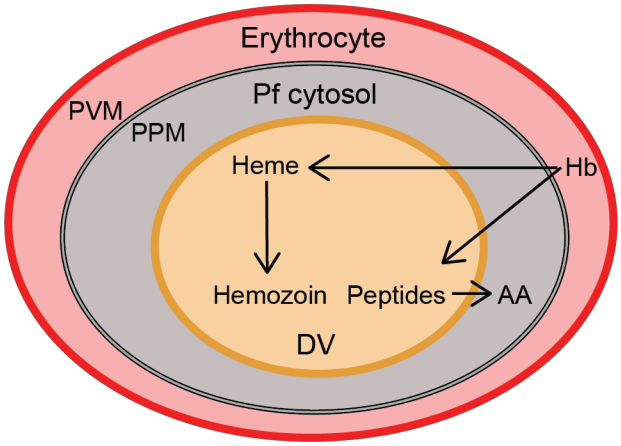

Figure 1.3 Hemoglobin degradation in the digestive vacuole of the asexual blood stage *Plasmodium* parasite. Host hemoglobin (Hb) is degraded into peptides and amino acids that are essential for parasite protein synthesis. Additionally, Hb produces toxic heme, which becomes detoxified via hemozin formation. Hb, hemoglobin; Pf, *Plasmodium falciparum*, PVM, parasitophorous vacuolar membrane; PPM, parasite plasma membrane; DV, digestive vacuole; AA, amino acids.

1.4 Antimalarial drugs

1.4.1 4-aminoquinolines

Quinoline-containing chemical compounds, like quinine (QN) extracted from the cinchona tree, have been used for malaria treatment since the 17th century [24]. However, the complexity of QN production, potential side effects, and a supply shortage during World War I led both British and German scientists to begin developing synthetic quinoline-like substitutions for QN. Subsequently, 4-aminoquinolines, such as chloroquine (CQ), amodiaquine (ADQ),

piperaquine (PPQ) and pyronaridine (PA), and new arylamino alcohols (chemically modified versions of QN) including mefloquine (MQ) and lumefantrine (LMF), have led to more affordable, safe and efficient malaria treatments (**Table 1.1**). 4-aminoquinolines are thought to prevent the formation of hemozoin in the DV of ABS parasites, thus, inhibiting the detoxification of the toxic heme [11].

Table 1.1 Features of antimalarial drugs

Name	Chemical class	ACT Drug?	Primary clinical use	Primary target	Resistance determinants
Chloroquine (CQ)	4-aminoquinoline	No	P. vivax malaria + unofficial use for P. falciparum	Heme/hemozoin	PfCRT point mutations, secondary role for PfMDR1
Piperaquine (PPQ)	Bis-quinoline	Yes (DHA+PPQ)	First-line partner drug in most of SE Asia	Heme/hemozoin	PfCRT mutations, minor role for plasmepsin II
Amodiaquine (ADQ)	4-aminoquinoline	Yes	First-line partner drug in	Heme/hemozoin	PfCRT and PfMDR1 point
Lumefantrine (LMF)	Arylaminoalcohol	Yes (ATM+LMF)	First-line partner drug in Africa and parts of SE Asia	Hemoglobin import?	PfMDR1, secondary role for wild-type PfCRT
Artemisinin	Endoperoxides	Yes	First-line therapy worldwide	Unknown	Mutations in K13
Quinine (QN)	Arylaminoalcohol	No	Second line, severe malaria	Heme/hemozoin	PfCRT and PfMDR1

1.4.2 Chloroquine

Chloroquine (CQ), a 4-aminoquinoline drug, was first discovered in 1934 and was originally named Resochin by Hans Andersag and his colleagues at the Bayer laboratories. CQ showed minimal adverse effects during a 1943 clinical trial, and was since widely used among endemic regions as an affordable and effective first-line antimalarial treatment during the 1950s and 1960s [24].

As a weak base, CQ freely diffuses into the acidic DV of parasites (approximately 5.3), where it becomes protonated and subsequently trapped within the DV. Inside the DV, di-protonated CQ binds to reactive dimeric heme, β-hematin, and caps further growth of chemically inert hemozoin crystals (**Fig. 1.4**), causing a toxic accumulation of free heme or heme-drug adducts [11, 23, 25].

Resistance to the former first-line CQ was first observed in the 1950s near the Thai-Cambodian border and in South America. As resistance spread from Asia into Africa, it had a devastating impact with reports of up to 6–fold increases in regional malaria mortality rates [26].

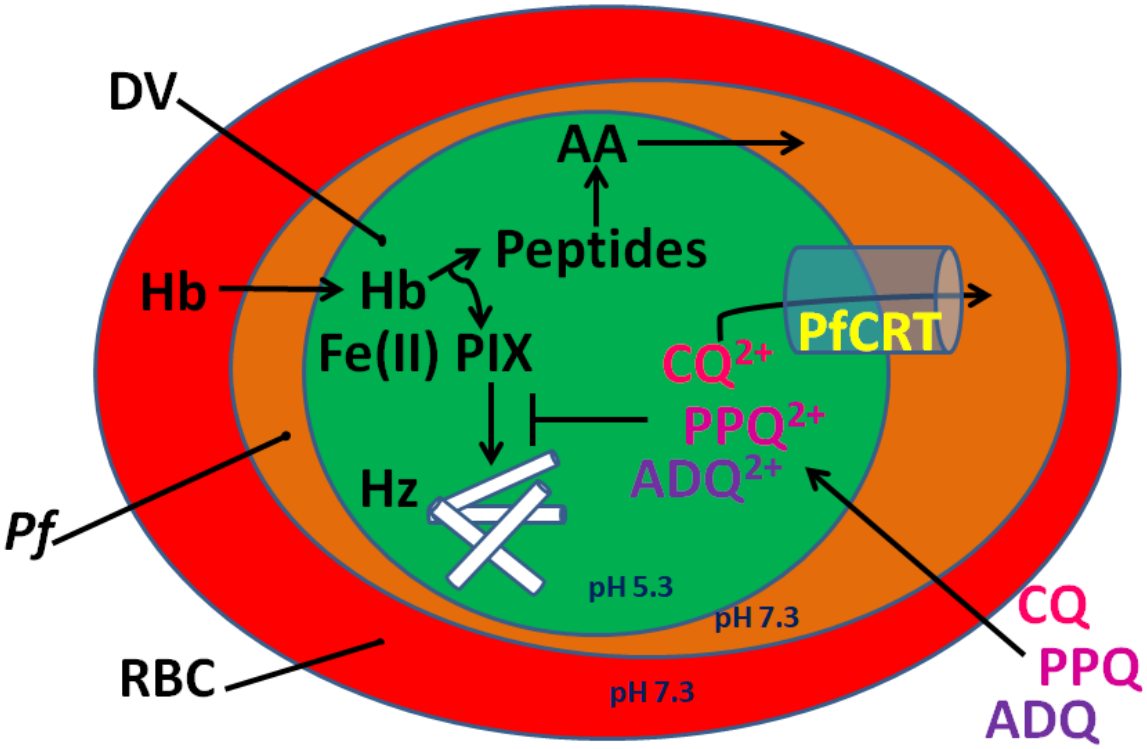

Figure 1.4 The mechanism of 4-aminoquinoline action in the digestive vacuole (DV) of asexual blood stage (ABS) parasite. 4-aminoquinoline antimalarials becomes protonated in the acidic DV and are thought to bind heme (iron protoporphyrin IX or Fe(II)PIX) preventing its incorporation into inert hemozoin. AA, amino acids; ADQ, amodiaquine; CQ, chloroquine; DV, digestive vacuole; Hb, hemoglobin; Hz, hemozoin; Pf, *Plasmodium falciparum*; PfCRT, *Plasmodium falciparum* chloroquine resistance transporter; PPQ, piperaquine; RBC, red blood cell.

1.4.3 Artemisinin-based Combination Therapies (ACTs)

The currently available antimalarial drugs mostly target the asexual blood stage (ABS) of parasites as this stage is responsible for the disease symptoms. The emergence and spread of resistance to CQ has spurred the adoption of artemisinin-based combination therapies (ACTs)

since the early 2000s. ACTs consist of a fast-acting artemisinin derivative (ART) with a longer-acting partner antimalarial drug.

The Chinese wormwood *Artemsia annua* was used in treating malaria symptoms for hundreds of years as documented in Ge Hong's *A Handbook of Prescription for Emergencies* which was written in approximately 300 BC [27]. Artemisinin was extracted and isolated from the *Artemsia annua* in the 1970s and has been shown to alleviate malaria fever and reduce the number of parasites in the blood [27]. Subsequently, other artemisinin derivatives have been introduced with improved stability, higher efficacy, improved oral bioavailability and a faster parasite clearance rate compared to the original artemisinin compound [27, 28] (**Fig. 1.5**). Artemisinin and its derivatives (ARTs) become activated once inside the ABS parasites due to the reductive scission of their endoperoxide bridge by heme. This activated form of artemisinin generates free radicals, resulting in the alkylation of biomolecules. This leads to parasite death due to oxidative stress and cellular damage [11, 28, 29]. The artemisinin derivatives are fast acting against the ABS malaria parasites resulting in rapid clearance; however, they have a short *in vivo* half-life of 1 to 3 hours in human patients [28, 30].

To supplement the poor pharmacokinetic properties of artemisinin and its derivatives, combination therapy has been implemented where ARTs are combined with a partner antimalarial, such as a 4-aminoquinoline or arylamino alcohol drug. The World Health Organization (WHO) currently recommends six different ACTs as the first line treatment depending on geographical resistance profile: Artesunate + amodiaquine (ASAQ); artesunate + mefloquine (ASMQ); artesunate + sulfadoxine-pyrimethamine (ASSP); artesunate + pyronaridine (PA), artemether + lumefantrine (AL); dihydroartemisinin + piperaquine (DHA-

PPQ) (**Table 1.2**). The partner drugs have longer half-lives compared to ARTs, aid in clearing any remaining parasites in the bloodstream, and help prevent recrudescence of disease [31].

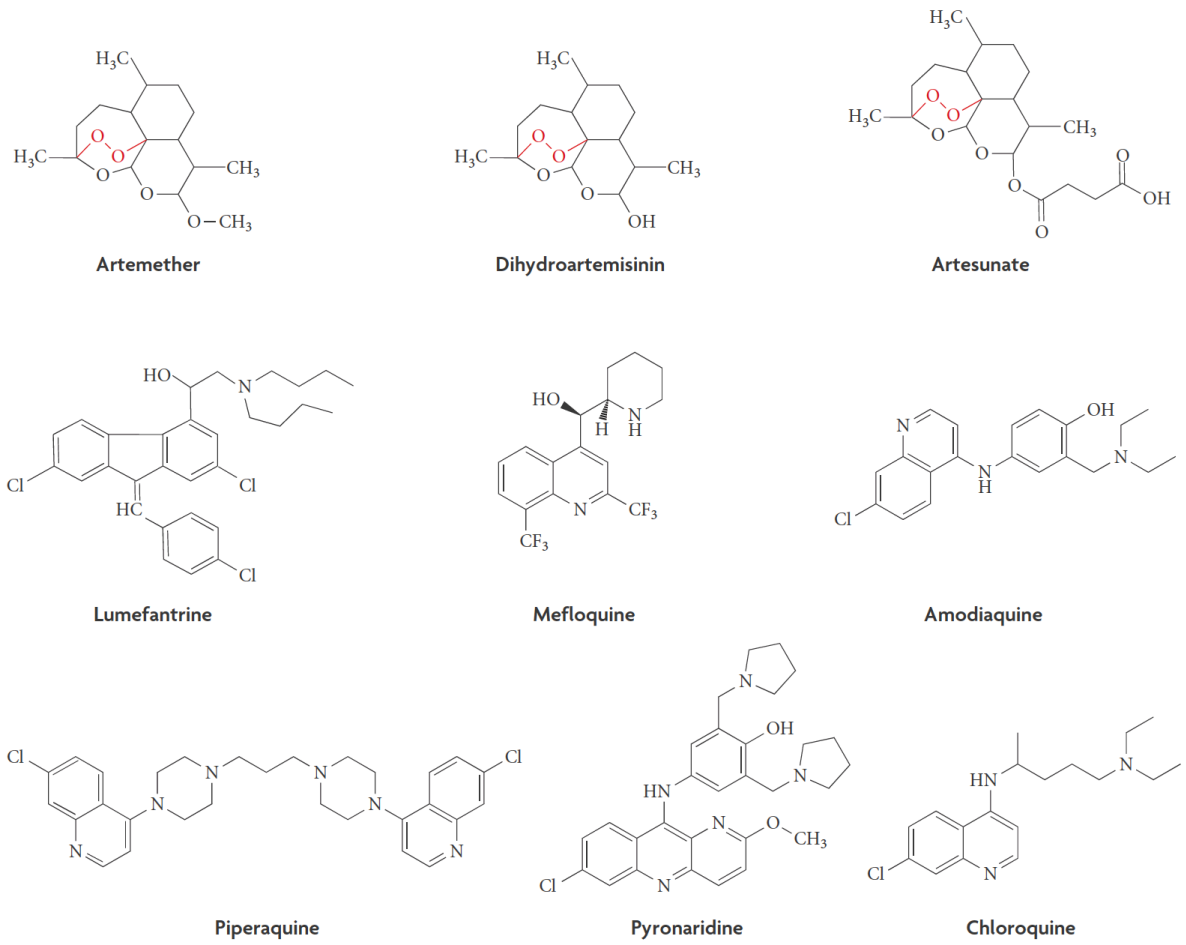

Figure 1.5 Chemical structures of Artemisinin derivatives and partner drugs. Figure adapted from [28].

Table 1.2 Current Artemisinin-based Combination Therapies (ACTs) for Clinical Use. Table adapted from [11].

Combination*	Abbreviation	Geographic use
Artemether + lumefantrine	AL	Most widely used ACT in Africa
Artesunate + amodiaquine	ASAQ	Used mostly in western Africa
Dihydroartemisinin + piperaquine	DHA–PPQ	First-line in several Southeast Asian countries#
Artesunate + mefloquine	ASMQ	Preceded DHA-PPQ in Southeast Asia
Artesunate + sulfadoxine–pyrimethamine	ASSP	Used in India and some Middle Eastern and eastern African countries
Artesunate + pyronaridine	PA	Recently received a positive scientific opinion under Article 58 by the EMA, currently being registered in both Africa and Asia

Asterisk (*) notes that these combinations are all therapeutically indicated for the treatment of uncomplicated *P. falciparum* or *P. vivax* malaria. Artesunate is recommended for the treatment of severe malaria[2]. Pound sign (#) indicates that DHA–PPQ is also being widely tested in Africa for mass drug administration and for intermittent preventive treatment of malaria in pregnancy.

ACTs have become the first-line treatment for malaria since the early 2000s. The incidence of malaria in the past 15 years has reduced substantially with the global adoption of ACTs as the first-line treatment, with mortality rates declining 60% between 2000 and 2015 (**Fig.1.6**). However, artemisinin (ART) resistance has also developed over time. In recent years, the reduction of malaria death rate has stalled (**Fig. 1.6**), due mainly to parasite and *Anopheles* vector resistance. The first case of resistance to artemisinin *in vivo* was observed in western Cambodia, where a patient exhibited a prolonged parasite clearance rate [32, 33]. Sequence analysis studies revealed mutations in the Kelch-like protein K13 as the primary determinant of ART resistance [34, 35]. Although the mechanism of how individual mutations in the *k13* gene lead to ART resistance is still unclear, the resistance mutations are thought to enhance the cellular response to oxidative stress caused by ART [11, 29, 35].

Resistance has also emerged against the partner drugs of ACTs. For example, a recent failure of the first-line treatment, DHA-PPQ, in Cambodia resulted from the resistance to PPQ

[36, 37]. The genetic analyses and studies suggest that PPQ resistance is linked to mutations in *pfcrt* [38-40] and k13 genes [41].

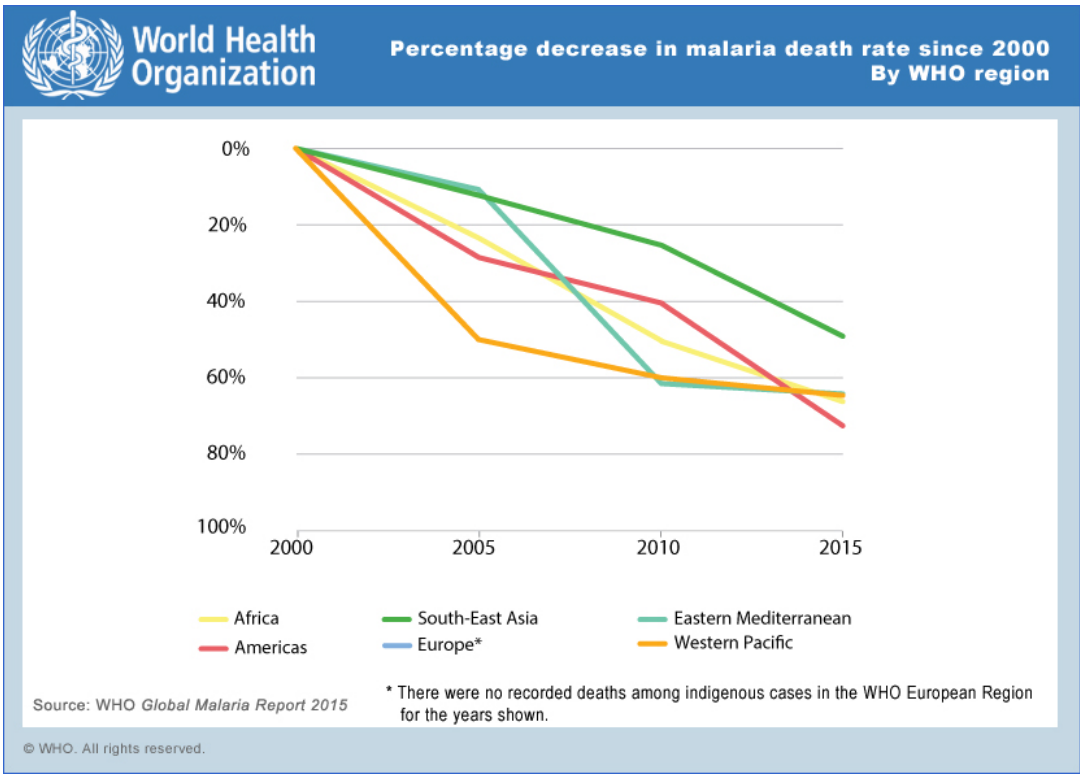

Figure 1.6 Recent reductions in the global malaria burden since 2000. Graph shows the recent decrease in the percentage of death rate due to malaria among different regions. Figure adapted from [1].

1.5 *Plasmodium falciparum* Chloroquine Resistance Transporter PfCRT

In 2000, it was discovered that CQ resistant parasites had certain point mutations in a transmembrane protein residing on the DV membrane - a protein now known as *Plasmodium falciparum* chloroquine resistance transporter (PfCRT) [42]. PfCRT, a member of the drug/metabolite transporter (DMT) superfamily [43], is a 49 kDa integral membrane protein, consisting of 424 total amino acids, that localizes to the DV membrane of parasite in the trophozoite stage (**Fig. 1.7**). The DMT superfamily represents a large group of membrane transporters widely existing in eukaryotes, bacteria and archaea, and comprises 14 phylogenetic

families [44]. The DMT proteins maintain cellular homeostasis by exporting essential nutrients and metabolites including amino acids and sugars that can be detrimental at high concentrations [44]. Structurally, DMT superfamily proteins, including PfCRT, are predicted to have 10 transmembrane (TM) helices [43, 44].

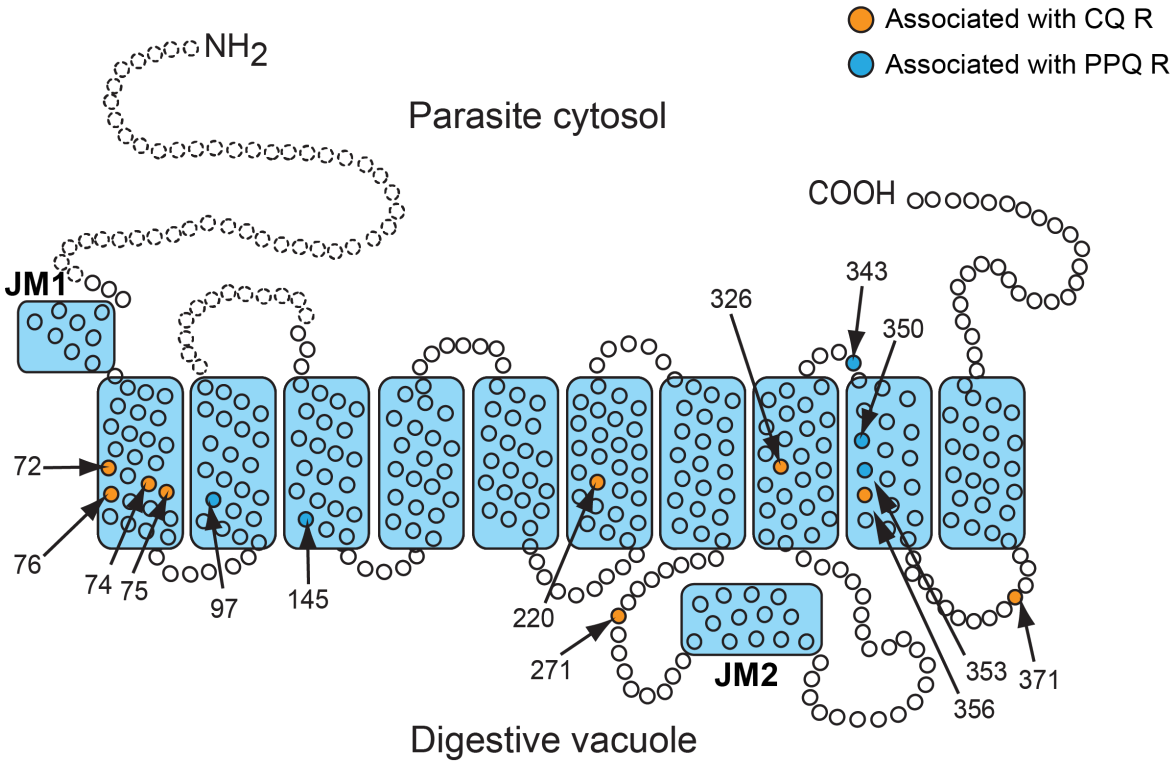

Figure 1.7 Topology of PCRT and location of residues involved in chloroquine (CQ) or piperaquine (PPQ) drug resistance phenotypes. Localization of PfCRT mutations associated with CQ or PPQ resistance. JM, juxtamembrane.

Point mutations in PfCRT are the primary determinants of CQ and PPQ resistance and treatment failure (**Fig. 1.7**) [42, 45, 46]. Subsequent studies identified multiple PfCRT isoforms that have evolved in distinct geographic regions with varying drug susceptibility (**Table 1.3**) [39, 47-50]. Notably, all CQ resistance conferring mutant isoforms share the K76T mutation, which has been used as a molecular marker for CQ resistance [51]. Studies have demonstrated that CQ

resistant PfCRT mutants can pump CQ out of the DV into the cytosol. This proton motive-force dependent CQ efflux has been shown to mediate CQ resistance in the mutant parasites [52-56]. The inhibition of the H^+-pumping V-type ATPase by concanamycin A further demonstrates that the efflux of CQ and proton from the DV in CQ-resistant parasites [57].

Table 1.3 Core PfCRT haplotypes in Southeast Asia, Africa and South America.

		PfCRT haplotype								
Strain or Type	Region	72	74	75	76	220	271	326	356	371
Dd2	SE Asia	C	I	E	T	S	E	S	T	I
Cam783	Africa	C	I	E	T	S	E	N	T	I
GB4	SE Asia, Africa	C	I	E	T	S	E	N	I	I
7G8	S. America	S	M	N	T	S	Q	D	L	R
Hb3 (wild-type)	Africa	C	M	N	K	A	Q	N	I	R

Mutations in the Dd2 allele are shown in light grey. Others are in dark grey.

PfCRT is also a major determinant of *Plasmodium falciparum* resistance to the ACT partner drugs PPQ and ADQ, as well as the second-line drug quinine (QN) (**Table 1.1**) [38, 39, 47, 58]. It was believed that the amplification of *plasmepsins 2 and 3* which encode an Hb digesting protease was the mediator of resistance to PPQ [59, 60]. However, novel mutations, such as T93S, H97Y, F145I, I218F, M343L and G353V, have emerged from the PfCRT Dd2 isoform in Cambodia mediating high- and low-grade resistance to PPQ used in combination with dihydroartemisinin (DHA) [39, 61, 62]. Interestingly, the same study further demonstrates that these particular mutations which increase resistance to PPQ, increase sensitivity to CQ, ADQ and QN, highlighting the possibility of different drug resistance mechanisms mediated by PfCRT among the partner drugs of ACTs [39]. In French Guiana, a novel C350R mutation in the 7G8

isoform has also appeared to show a similar phenotype in which the C350R mutation reverses the CQ hypersensitivity while conferring resistance to PPQ [63]. Moreover, PfCRT 7G8, a CQ-resistant isoform in South America, also mediates resistance to ADQ and its active metabolite monodesethyl amodiaquine (MDADQ), suggesting an important driving force for selection [47, 58].

The Ca^{2+} channel blocker verapamil (VP) reduces the efflux of CQ while enhances the accumulation of CQ in the DV [64]. The role of PfCRT in verapamil-reversible CQR suggests that PfCRT as a therapeutic target for new drugs by leveraging the resistance reversibility [50]. Despite of ample evidence in PfCRT as a drug transporter, our understanding on its natural substrate under physiological condition still remains elusive. To date, PfCRT has been proposed to transport amino acid, peptides and glutathione [55, 65-67].

1.6 Significant work presented in this dissertation

Defining the susceptibility profiles of newly emerging drug resistant PfCRT isoforms and predicting their impact on clinically employed antimalarials is crucial in developing effective treatments for malaria. However, a major limitation in our understanding of PfCRT up to date has been the lack of mechanistic insight into its structure and function. This information can help explain modes of action of CQ, PPQ, and other related antimalarial drugs, and *Plasmodium falciparum* susceptibility to them.

The importance of PfCRT as a mediator of antimalarial drug resistance and the hope for developing more effective treatment to save many lives, especially children, motivated me to commit to this project. In this dissertation, I will present the first structure of PfCRT which

provides greater insight into the molecular mechanism of this key mediator of antimalarial resistance.

In the next chapter, I will discuss general challenges present in the structural studies of membrane proteins at the current stage. Then, I will discuss specific problems I faced during my thesis project and address how I overcame them. I will then present the manuscript that has been submitted for review recently which describes the first structure of PfCRT and reports on functional characterization of the protein with detailed experimental procedures. In the last chapter, I will present ongoing experiments to provide further explanation on how PfCRT mediates drug resistance, and propose future plans regarding the project.

References

1. World Health Organization, *World Malaria Report 2018*. 2018: Geneva: World Health Organization.
2. Phillips, M.A., et al., *Malaria.* Nat Rev Dis Primers, 2017. **3**: p. 17050.
3. Cox, F.E., *History of the discovery of the malaria parasites and their vectors.* Parasit Vectors, 2010. **3**(1): p. 5.
4. Nye, E.R., *Alphonse Laveran (1845-1922): discoverer of the malarial parasite and Nobel laureate, 1907.* J Med Biogr, 2002. **10**(2): p. 81-7.
5. Bynum, W.F., *Portraits of science. Mosquitoes bite more than once.* Science, 2002. **295**(5552): p. 47-8.
6. Beier, J.C., *Malaria parasite development in mosquitoes.* Annu Rev Entomol, 1998. **43**: p. 519-43.
7. Zhang, M., et al., *Uncovering the essential genes of the human malaria parasite Plasmodium falciparum by saturation mutagenesis.* Science, 2018. **360**(6388).
8. Bushell, E., et al., *Functional Profiling of a Plasmodium Genome Reveals an Abundance of Essential Genes.* Cell, 2017. **170**(2): p. 260-272 e8.
9. Ecker, A., et al., *Tricks in Plasmodium's molecular repertoire--escaping 3'UTR excision-based conditional silencing of the chloroquine resistance transporter gene.* Int J Parasitol, 2012. **42**(11): p. 969-74.
10. Bannister, L. and G. Mitchell, *The ins, outs and roundabouts of malaria.* Trends Parasitol, 2003. **19**(5): p. 209-13.
11. Blasco, B., D. Leroy, and D.A. Fidock, *Antimalarial drug resistance: linking Plasmodium falciparum parasite biology to the clinic.* Nat Med, 2017. **23**(8): p. 917-928.

12. Lee, A.H., L.S. Symington, and D.A. Fidock, *DNA repair mechanisms and their biological roles in the malaria parasite Plasmodium falciparum.* Microbiol Mol Biol Rev, 2014. **78**(3): p. 469-86.
13. Maier, A.G., et al., *Malaria parasite proteins that remodel the host erythrocyte.* Nat Rev Microbiol, 2009. **7**(5): p. 341-54.
14. Hora, R., et al., *Cerebral malaria--clinical manifestations and pathogenesis.* Metab Brain Dis, 2016. **31**(2): p. 225-37.
15. Miller, L.H., et al., *The pathogenic basis of malaria.* Nature, 2002. **415**(6872): p. 673-9.
16. Hiller, N.L., et al., *A host-targeting signal in virulence proteins reveals a secretome in malarial infection.* Science, 2004. **306**(5703): p. 1934-7.
17. Abu Bakar, N., et al., *Digestive-vacuole genesis and endocytic processes in the early intraerythrocytic stages of Plasmodium falciparum.* J Cell Sci, 2010. **123**(Pt 3): p. 441-50.
18. Saliba, K.J., et al., *Acidification of the malaria parasite's digestive vacuole by a H+-ATPase and a H+-pyrophosphatase.* J Biol Chem, 2003. **278**(8): p. 5605-12.
19. Liu, J., et al., *Plasmodium falciparum ensures its amino acid supply with multiple acquisition pathways and redundant proteolytic enzyme systems.* Proc Natl Acad Sci U S A, 2006. **103**(23): p. 8840-5.
20. Istvan, E.S., et al., *Validation of isoleucine utilization targets in Plasmodium falciparum.* Proc Natl Acad Sci U S A, 2011. **108**(4): p. 1627-32.
21. Goldberg, D.E., *Complex nature of malaria parasite hemoglobin degradation [corrected].* Proc Natl Acad Sci U S A, 2013. **110**(14): p. 5283-4.
22. Egan, T.J., et al., *Fate of haem iron in the malaria parasite Plasmodium falciparum.* Biochem J, 2002. **365**(Pt 2): p. 343-7.
23. Pagola, S., et al., *The structure of malaria pigment beta-haematin.* Nature, 2000. **404**(6775): p. 307-10.
24. Foley, M. and L. Tilley, *Quinoline antimalarials: mechanisms of action and resistance and prospects for new agents.* Pharmacol Ther, 1998. **79**(1): p. 55-87.
25. Combrinck, J.M., et al., *Insights into the role of heme in the mechanism of action of antimalarials.* ACS Chem Biol, 2013. **8**(1): p. 133-7.
26. Miller, L.H., et al., *Malaria biology and disease pathogenesis: insights for new treatments.* Nat Med, 2013. **19**(2): p. 156-67.
27. Tu, Y., *The discovery of artemisinin (qinghaosu) and gifts from Chinese medicine.* Nat Med, 2011. **17**(10): p. 1217-20.
28. Eastman, R.T. and D.A. Fidock, *Artemisinin-based combination therapies: a vital tool in efforts to eliminate malaria.* Nat Rev Microbiol, 2009. **7**(12): p. 864-74.
29. Tilley, L., et al., *Artemisinin Action and Resistance in Plasmodium falciparum.* Trends Parasitol, 2016. **32**(9): p. 682-696.
30. White, N.J., *Qinghaosu (artemisinin): the price of success.* Science, 2008. **320**(5874): p. 330-4.
31. Enserink, M., *Malaria's drug miracle in danger.* Science, 2010. **328**(5980): p. 844-6.
32. Noedl, H., et al., *Evidence of artemisinin-resistant malaria in western Cambodia.* N Engl J Med, 2008. **359**(24): p. 2619-20.
33. Dondorp, A.M., et al., *Artemisinin resistance in Plasmodium falciparum malaria.* N Engl J Med, 2009. **361**(5): p. 455-67.

34. Ariey, F., et al., *A molecular marker of artemisinin-resistant Plasmodium falciparum malaria.* Nature, 2014. **505**(7481): p. 50-5.
35. Straimer, J., et al., *Drug resistance. K13-propeller mutations confer artemisinin resistance in Plasmodium falciparum clinical isolates.* Science, 2015. **347**(6220): p. 428-31.
36. Amaratunga, C., et al., *Dihydroartemisinin-piperaquine resistance in Plasmodium falciparum malaria in Cambodia: a multisite prospective cohort study.* Lancet Infect Dis, 2016. **16**(3): p. 357-65.
37. Leang, R., et al., *Evidence of Plasmodium falciparum Malaria Multidrug Resistance to Artemisinin and Piperaquine in Western Cambodia: Dihydroartemisinin-Piperaquine Open-Label Multicenter Clinical Assessment.* Antimicrob Agents Chemother, 2015. **59**(8): p. 4719-26.
38. Dhingra, S.K., et al., *A Variant PfCRT Isoform Can Contribute to Plasmodium falciparum Resistance to the First-Line Partner Drug Piperaquine.* MBio, 2017. **8**(3).
39. Ross, L.S., et al., *Emerging Southeast Asian PfCRT mutations confer Plasmodium falciparum resistance to the first-line antimalarial piperaquine.* Nat Commun, 2018. **9**(1): p. 3314.
40. Agrawal, S., et al., *Association of a Novel Mutation in the Plasmodium falciparum Chloroquine Resistance Transporter With Decreased Piperaquine Sensitivity.* J Infect Dis, 2017. **216**(4): p. 468-476.
41. Duru, V., et al., *Plasmodium falciparum dihydroartemisinin-piperaquine failures in Cambodia are associated with mutant K13 parasites presenting high survival rates in novel piperaquine in vitro assays: retrospective and prospective investigations.* BMC Med, 2015. **13**: p. 305.
42. Fidock, D.A., et al., *Mutations in the P. falciparum digestive vacuole transmembrane protein PfCRT and evidence for their role in chloroquine resistance.* Mol Cell, 2000. **6**(4): p. 861-71.
43. Martin, R.E. and K. Kirk, *The malaria parasite's chloroquine resistance transporter is a member of the drug/metabolite transporter superfamily.* Mol Biol Evol, 2004. **21**(10): p. 1938-49.
44. Jack, D.L., N.M. Yang, and M.H. Saier, Jr., *The drug/metabolite transporter superfamily.* Eur J Biochem, 2001. **268**(13): p. 3620-39.
45. Djimde, A., et al., *A molecular marker for chloroquine-resistant falciparum malaria.* N Engl J Med, 2001. **344**(4): p. 257-63.
46. Sidhu, A.B., D. Verdier-Pinard, and D.A. Fidock, *Chloroquine resistance in Plasmodium falciparum malaria parasites conferred by pfcrt mutations.* Science, 2002. **298**(5591): p. 210-3.
47. Sa, J.M., et al., *Geographic patterns of Plasmodium falciparum drug resistance distinguished by differential responses to amodiaquine and chloroquine.* Proc Natl Acad Sci U S A, 2009. **106**(45): p. 18883-9.
48. Callaghan, P.S., M.R. Hassett, and P.D. Roepe, *Functional Comparison of 45 Naturally Occurring Isoforms of the Plasmodium falciparum Chloroquine Resistance Transporter (PfCRT).* Biochemistry, 2015. **54**(32): p. 5083-94.
49. Petersen, I., et al., *Balancing drug resistance and growth rates via compensatory mutations in the Plasmodium falciparum chloroquine resistance transporter.* Mol Microbiol, 2015. **97**(2): p. 381-95.

50. Ecker, A., et al., *PfCRT and its role in antimalarial drug resistance.* Trends Parasitol, 2012. **28**(11): p. 504-14.
51. Lakshmanan, V., et al., *A critical role for PfCRT K76T in Plasmodium falciparum verapamil-reversible chloroquine resistance.* EMBO J, 2005. **24**(13): p. 2294-305.
52. Bray, P.G., et al., *Defining the role of PfCRT in Plasmodium falciparum chloroquine resistance.* Mol Microbiol, 2005. **56**(2): p. 323-33.
53. Paguio, M.F., M. Cabrera, and P.D. Roepe, *Chloroquine transport in Plasmodium falciparum. 2. Analysis of PfCRT-mediated drug transport using proteoliposomes and a fluorescent chloroquine probe.* Biochemistry, 2009. **48**(40): p. 9482-91.
54. Zhang, H., M. Paguio, and P.D. Roepe, *The antimalarial drug resistance protein Plasmodium falciparum chloroquine resistance transporter binds chloroquine.* Biochemistry, 2004. **43**(26): p. 8290-6.
55. Martin, R.E., et al., *Chloroquine transport via the malaria parasite's chloroquine resistance transporter.* Science, 2009. **325**(5948): p. 1680-2.
56. Juge, N., et al., *Plasmodium falciparum chloroquine resistance transporter is a H+-coupled polyspecific nutrient and drug exporter.* Proc Natl Acad Sci U S A, 2015. **112**(11): p. 3356-61.
57. Lehane, A.M., et al., *A verapamil-sensitive chloroquine-associated H+ leak from the digestive vacuole in chloroquine-resistant malaria parasites.* J Cell Sci, 2008. **121**(Pt 10): p. 1624-32.
58. Gabryszewski, S.J., et al., *Combinatorial Genetic Modeling of pfcrt-Mediated Drug Resistance Evolution in Plasmodium falciparum.* Mol Biol Evol, 2016. **33**(6): p. 1554-70.
59. Amato, R., et al., *Genetic markers associated with dihydroartemisinin-piperaquine failure in Plasmodium falciparum malaria in Cambodia: a genotype-phenotype association study.* Lancet Infect Dis, 2017. **17**(2): p. 164-173.
60. Witkowski, B., et al., *A surrogate marker of piperaquine-resistant Plasmodium falciparum malaria: a phenotype-genotype association study.* Lancet Infect Dis, 2017. **17**(2): p. 174-183.
61. van der Pluijm, R.W., et al., *Determinants of dihydroartemisinin-piperaquine treatment failure in Plasmodium falciparum malaria in Cambodia, Thailand, and Vietnam: a prospective clinical, pharmacological, and genetic study.* Lancet Infect Dis, 2019.
62. Hamilton, W.L., et al., *Evolution and expansion of multidrug-resistant malaria in southeast Asia: a genomic epidemiology study.* Lancet Infect Dis, 2019.
63. Pelleau, S., et al., *Adaptive evolution of malaria parasites in French Guiana: Reversal of chloroquine resistance by acquisition of a mutation in pfcrt.* Proc Natl Acad Sci U S A, 2015. **112**(37): p. 11672-7.
64. Krogstad, D.J., et al., *Efflux of chloroquine from Plasmodium falciparum: mechanism of chloroquine resistance.* Science, 1987. **238**(4831): p. 1283-5.
65. Lewis, I.A., et al., *Metabolic QTL analysis links chloroquine resistance in Plasmodium falciparum to impaired hemoglobin catabolism.* PLoS Genet, 2014. **10**(1): p. e1004085.
66. Ginsburg, H., et al., *Inhibition of glutathione-dependent degradation of heme by chloroquine and amodiaquine as a possible basis for their antimalarial mode of action.* Biochem Pharmacol, 1998. **56**(10): p. 1305-13.
67. Patzewitz, E.M., et al., *Glutathione transport: a new role for PfCRT in chloroquine resistance.* Antioxid Redox Signal, 2013. **19**(7): p. 683-95.

Chapter 2 MEMBRANE PROTEIN STRUCTURE

2.1 Membrane protein: Introduction

Membrane proteins, including transporters, pumps, enzymes, receptors and channels, play important roles in many fundamental biological processes. They are essential in maintaining the structural integrity of the cell membrane, relaying signals between the extracellular and intracellular environment, and transporting small molecules and ions across the cell membrane facilitating the maintenance of cellular homeostasis. Membrane proteins constitute approximately 22% of the human proteome, and approximately 60% of current drug targets are membrane proteins [68].

Despite their relevance as therapeutic targets for various human diseases, our knowledge of membrane protein structures is still scarce. In fact, only approximately 900 unique membrane protein structures have been determined up to date (**Fig. 2.1;** *https://blanco.biomol.uci.edu/mpstruc/; data retrieved on June 3, 2019*) from the total predicted 31,778 genes encoding for membrane proteins [69]. Thus, less than 3% of the unique structures of membrane proteins are currently available in the Protein Data Bank (PDB, https://www.rcsb.org) and much remains to be discovered.

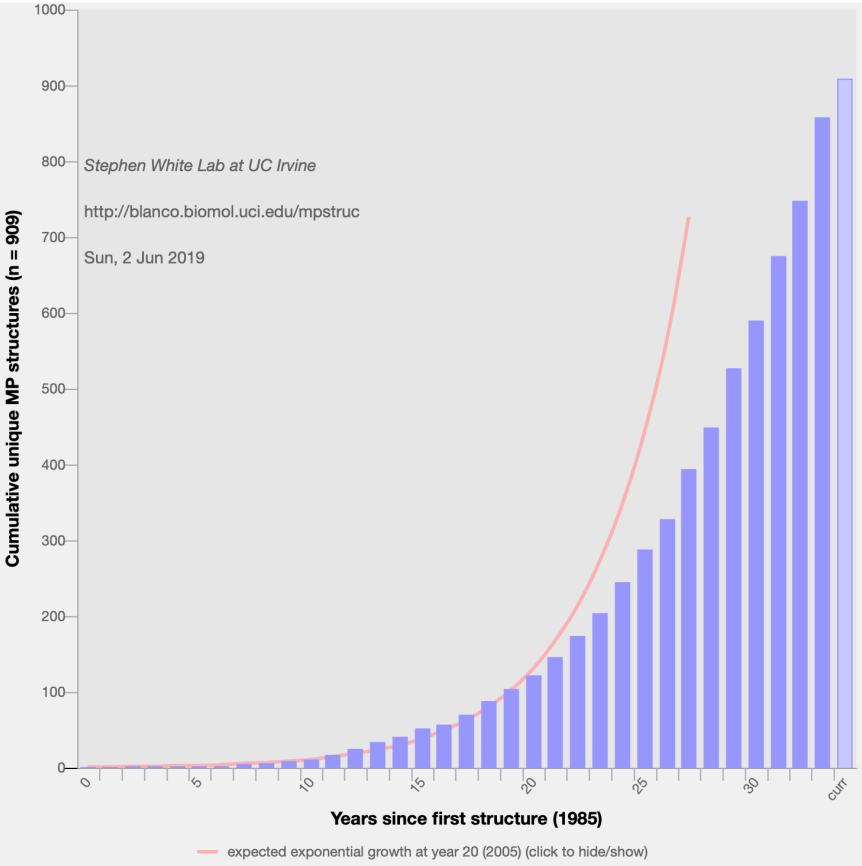

Figure 2.1 Membrane protein structural determination over time. The graph was adapted from Stephen White's Membrane Proteins of Known Structures Database https://blanco.biomol.uci.edu/mpstruc/; data retrieved on June 3, 2019.

The first three-dimensional projection structure of bacteriorhodopsin from *Halobacterium halobium* was determined at 7Å resolution using electron crystallography on two-dimensional crystals in 1975 by Richard Henderson and Nigel Unwin [70]. The first atomic-resolution structure of a membrane protein, the photosynthetic reaction center purified from *Rhodopseudomonas viridis*, was solved to 3Å resolution using x-ray crystallography in 1985 [71]. Since then, the advancements in the three major techniques for structural studies – x-ray crystallography, electron microscopy (EM) and nuclear magnetic resonance (NMR) – have been accelerating the progress of structural biology of membrane proteins (**Fig 2.1**). Over the years the most predominant technique for structural studies of membrane proteins has been x-ray

crystallography, and the majority of membrane protein structures deposited in the PDB are determined by using x-ray crystallography [72]. Recent technological advancements in the field of single-particle cryogenic electron microscopy (cryo-EM) has further facilitated new pathway for structural determination of selective classes of proteins. However, cryo-EM is still not suitable for solving small molecules (i.e. < 100 kDa) to high resolution.

Despite of the exponential growth in the number of structures solved, sample preparation still remains a major bottleneck in membrane protein structural studies. Membrane proteins generally have low expression levels in cells and/or heterologous systems. Moreover, eukaryotic membrane proteins often require eukaryotic host cells such as yeast, insect cells and mammalian cells [73]. The low abundance of membrane proteins makes it extremely difficult for structural analysis. Furthermore, the hydrophobic nature of membrane proteins within lipid bilayers often further complicates structure determination. Structural and functional studies of membrane protein require the protein to be extracted from the lipid bilayer and further solubilized and purified in the presence of surfactants like detergents. However, many detergents and their micelles are harsh for protein stability, as proteins can be misfolded once extracted from their native lipid environments leading to denaturation or aggregation. In x-ray crystallography, detergents and their micelles can hamper the ability of protein to be crystalized as they mask the transmembrane (TM) region and minimize the surface area for protein-protein crystal contacts. Also, detergents can be problematic in cryo-EM analysis as free empty detergent micelles tend to diminish the contrast of protein in cryo-EM images [74, 75]. Therefore, the choice of the appropriate detergent appears to be a challenge throughout all the steps towards membrane protein structure determination.

2.2 Structural Determination Technique: Single-Particle Cryo-Electron Microscopy (Cryo-EM)

In the past, the electron microscopy approach for structural determination of protein was limited by low resolution. Cryo-EM enables us to provide three-dimensional structural information of biological macromolecules by averaging EM images of non-crystalline specimens embedded in a thin layer of vitreous ice in random orientations [76]. A beam of electrons, as the source of illumination, transmits through a sample and projects an image [77]. The series of two-dimensional images from sample particles in the same orientation are averaged computationally and are further used to provide a three-dimensional electron density map [78]. Recent improvements in camera and data processing software packages together have led to the "resolution revolution" in cryo-EM [79]. Such improvements have allowed to determine structures of integral membrane proteins that had previously been intractable with x-ray crystallography including for example Transient receptor potential channel (TRPV1) [80], Stimulated by Retinoic Acid 6 (STRA6) [81] and Ryanodine receptors (RyRs) [82]. In the following sections, I will discuss the basic workflow of single-particle cryo-EM.

2.2.1 Sample preparation

One advantage of cryo-EM analysis over x-ray crystallography is that cryo-EM does not require a large quantity of homogeneous sample, which is a critical, yet, challenging parameter for crystallization and the need of crystals. Once a purified sample is obtained, negative stain EM is usually the first step to examine and screen the quality of target protein sample. It can also be used to reconstruct a low-resolution three-dimensional structure [83]. For negative stain, the sample is applied onto a carbon coated grid and stained with heavy metal salts like uranyl

formate or uranyl acetate, which readily interact with the electron beam to enhance phase contrast. The issue with negative stain is that the resolution is limited by the size of the heavy metal grains approximately to 15 Å.

2.2.2. Sample Vitrification

To obtain high resolution reconstructions, the sample is required to undergo a vitrification step for cryo-EM analysis. Vitrification is a crucial step, as it helps maintaining the specimen intact in the native orientation from the radiation damage in the electron microscope [84]. The protein sample is applied onto a holey carbon or gold grid, excess liquid is blotted away, and the sample is immediately plunged into liquid ethane cooled by liquid nitrogen, to approximately -160 °C, to create a thin layer of vitrified ice [85, 86]. Ice thickness is critical, as a consistent thin layer of ice on the grid helps establish high contrast between the protein particles and the ice background and also avoid possible defocus problems caused by the different heights of particles in the ice layer [76]. Currently, the commercially available automated plunge-freezer instruments, such as Leica EM GP, Vitrobot™, Cryoplunge™, are designed to produce a thin and reproducible vitrified ice layer, and variables like humidity, temperature and blotting time can be changed and optimized as needed for each sample [87].

2.2.3 Imaging

Vitrified samples in different cryogenic conditions are required to screen on a low-end microscope which provides information on sample particle distribution and ice thickness. The grid with the optimal cryogenic condition then can be imaged on a high-end microscope equipped with 200 kV or 300 kV acceleration voltage and a field emission gun (FEG) electron

source producing an electron beam with more penetrance and coherence [88]. Recent introduction of the direct electron detector device (DDD) camera [89] and beam-induced motion correction [90] helped improve EM image quality. Compared to previous technologies, the DDD camera provides enhanced detective quantum efficiency (DQE), a measure of signal and noise performance in an image with a function of spatial frequencies, to improve the signal-to-noise between sample particles and background. Also, the camera has the capability to record high frame rate movies instead of a single micrograph while correcting beam-induced movement and image blurring to enhance the sharpness of the particle images [89]. Such developments and improvements in camera have made it possible to produce a good quality of images and ultimately obtain a high-resolution density map.

2.2.4 Reconstruction

Determining a high-resolution 3D reconstruction requires 2D projection images. Particle picking from each micrograph can often be difficult as the image has low contrast and noise. The particle picking can be achieved either manually, automated, or semi-automated with templates. Particles in the same conformation are aligned, clustered and averaged together to enhance the signal to noise ratio in generating 2D projection images of particles [77]. A 3D reconstruction of the sample can be achieved by using the projection slice theorem, which combines the 2D Fourier transform of the 2D projection of electron densities from all angles followed by an inverse Fourier transform in 3D. When the particle images of a 3D reference in all projection directions are converged during the refinement, the final reconstruction is made through back projection of the 2D particles [91, 92](**Fig. 2.2**). Recent developments in data processing

algorithms and software packages such as RELION [93] and cryoSPARC [94] have provided convenient ways to proceed in the 3D reconstruction of protein sample from the cryo-EM data.

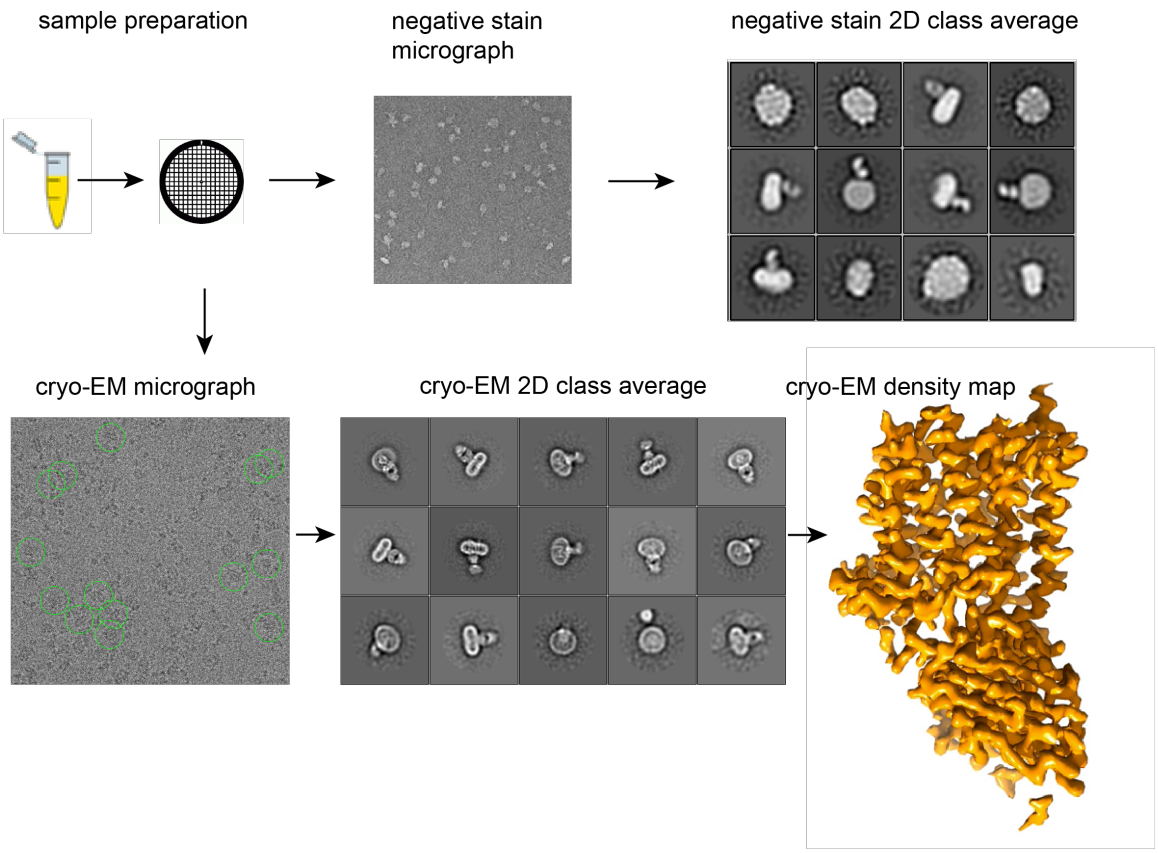

Figure 2.2 Structure determination workflow by single particle cryo-EM. Initial low resolution 2D classes can be obtained by negative stain EM. The purified protein sample can be frozen on grids for cryo-EM analysis. Micrographs are collected as a subframe movie, which is further aligned and averaged. Particles are picked from each image, aligned and clustered in the same spatial orientation and used to reconstruct a 3D structure.

References

68. Overington, J.P., B. Al-Lazikani, and A.L. Hopkins, *How many drug targets are there?* Nat Rev Drug Discov, 2006. **5**(12): p. 993-6.
69. Lander, E.S., et al., *Initial sequencing and analysis of the human genome.* Nature, 2001. **409**(6822): p. 860-921.
70. Henderson, R. and P.N. Unwin, *Three-dimensional model of purple membrane obtained by electron microscopy.* Nature, 1975. **257**(5521): p. 28-32.

71. Deisenhofer, J., et al., *Structure of the protein subunits in the photosynthetic reaction centre of Rhodopseudomonas viridis at 3A resolution.* Nature, 1985. **318**(6047): p. 618-24.
72. Hardy, D., et al., *Overcoming bottlenecks in the membrane protein structural biology pipeline.* Biochem Soc Trans, 2016. **44**(3): p. 838-44.
73. Bernaudat, F., et al., *Heterologous expression of membrane proteins: choosing the appropriate host.* PLoS One, 2011. **6**(12): p. e29191.
74. Schmidt-Krey, I. and J.L. Rubinstein, *Electron cryomicroscopy of membrane proteins: specimen preparation for two-dimensional crystals and single particles.* Micron, 2011. **42**(2): p. 107-16.
75. Gewering, T., et al., *Know your detergents: A case study on detergent background in negative stain electron microscopy.* J Struct Biol, 2018. **203**(3): p. 242-246.
76. Cheng, Y., et al., *A primer to single-particle cryo-electron microscopy.* Cell, 2015. **161**(3): p. 438-449.
77. De Rosier, D.J. and A. Klug, *Reconstruction of three dimensional structures from electron micrographs.* Nature, 1968. **217**(5124): p. 130-4.
78. Frank, J., et al., *Reconstruction of glutamine synthetase using computer averaging.* Ultramicroscopy, 1978. **3**(3): p. 283-90.
79. Kuhlbrandt, W., *Biochemistry. The resolution revolution.* Science, 2014. **343**(6178): p. 1443-4.
80. Liao, M., et al., *Structure of the TRPV1 ion channel determined by electron cryo-microscopy.* Nature, 2013. **504**(7478): p. 107-12.
81. Chen, Y., et al., *Structure of the STRA6 receptor for retinol uptake.* Science, 2016. **353**(6302).
82. Zalk, R., et al., *Structure of a mammalian ryanodine receptor.* Nature, 2015. **517**(7532): p. 44-9.
83. Booth, D.S., A. Avila-Sakar, and Y. Cheng, *Visualizing proteins and macromolecular complexes by negative stain EM: from grid preparation to image acquisition.* J Vis Exp, 2011(58).
84. Taylor, K.A. and R.M. Glaeser, *Electron diffraction of frozen, hydrated protein crystals.* Science, 1974. **186**(4168): p. 1036-7.
85. McDowall, A.W., et al., *Electron microscopy of frozen hydrated sections of vitreous ice and vitrified biological samples.* J Microsc, 1983. **131**(Pt 1): p. 1-9.
86. Lepault, J., F.P. Booy, and J. Dubochet, *Electron microscopy of frozen biological suspensions.* J Microsc, 1983. **129**(Pt 1): p. 89-102.
87. Dobro, M.J., et al., *Plunge freezing for electron cryomicroscopy.* Methods Enzymol, 2010. **481**: p. 63-82.
88. Cheng, Y., *Single-Particle Cryo-EM at Crystallographic Resolution.* Cell, 2015. **161**(3): p. 450-457.
89. McMullan, G., A.R. Faruqi, and R. Henderson, *Direct Electron Detectors.* Methods Enzymol, 2016. **579**: p. 1-17.
90. Li, X., et al., *Electron counting and beam-induced motion correction enable near-atomic-resolution single-particle cryo-EM.* Nat Methods, 2013. **10**(6): p. 584-90.
91. Penczek, P.A., *Fundamentals of three-dimensional reconstruction from projections.* Methods Enzymol, 2010. **482**: p. 1-33.

92. Carroni, M. and H.R. Saibil, *Cryo electron microscopy to determine the structure of macromolecular complexes.* Methods, 2016. **95**: p. 78-85.
93. Scheres, S.H., *RELION: implementation of a Bayesian approach to cryo-EM structure determination.* J Struct Biol, 2012. **180**(3): p. 519-30.
94. Punjani, A., et al., *cryoSPARC: algorithms for rapid unsupervised cryo-EM structure determination.* Nat Methods, 2017. **14**(3): p. 290-296.

Chapter 3 STRUCTURAL ELUCIDATION OF PfCRT 7G8

3.1 Introduction

As described in **Section 1.5**, PfCRT is a 49-kDa transporter spanning the membrane of the pathogenic intra-erythrocytic asexual blood stage (ABS) parasite's digestive vacuole and is responsible for resistance to both previously and currently used first-line antimalarials. Despite its importance both physiologically and clinically, further insight into PfCRT function and structure, and the molecular basis of PfCRT-mediated drug resistance, have been hampered by the lack of an atomic model. Structural information of PfCRT will help elucidate respective drug binding and drug resistance mechanisms and provide basis for the development of future therapies.

In this chapter, I will describe steps and approaches developed to overcome the challenges mentioned in Chapter 2 in determining a structure of PfCRT. I believe that the work detailed in the following sections represents a significant advance in understanding the molecular mechanisms underlying Pf resistance to antimalarial drugs in clinical use. Furthermore, determining the structure of a sub-50kDa membrane protein by cryo-EM is a noteworthy achievement.

Prior to presenting the manuscript which describes the first structure of PfCRT, I will briefly discuss the experimental procedures involving the optimization of PfCRT expression, stability, and purity.

3.2 Expression Screen of Chloroquine Resistance Transporter (CRT) Variants

The expression of PfCRT has been a long-standing problem in both structural and functional studies [95]. To overcome this crucial barrier, we used a structural genomics approach in which we screened for optimal expression of PfCRT variants with different drug resistance profiles, isoforms from different *Plasmodia*, or codon optimized for different organisms and expression systems (**Fig. 3.1 and Table 3.1**) [96]. We generated C-terminal GFP fusion constructs with a decahistidine affinity tag and screened them first for expression by western blot, and then for stability in detergent (dodecyl-maltoside; DDM) by fluorescence coupled size-exclusion chromatography (FSEC) (**Fig. 3.2**) [97]. These experiments allowed us to identify the PfCRT 7G8 CQ-resistant isoform as a candidate for structural investigation.

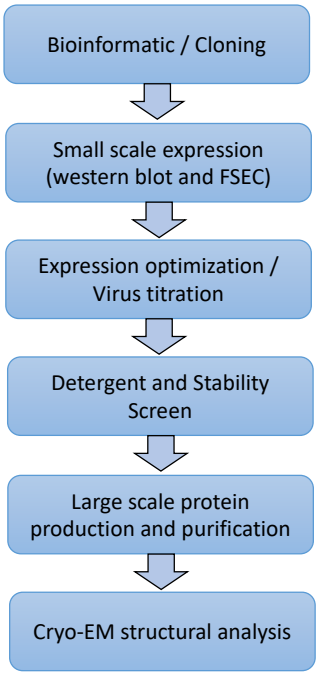

Figure 3.1 Schematic representation of COMPPÅ pipeline. Structural genomics method was adapted from the Center on Membrane Protein Production and Analysis (COMPPÅ) pipeline. The expression of target protein and its variants are screened in high throughput manner to identify the most promising target for further structural and functional studies. FSEC, fluorescence coupled size-exclusion chromatography.

Table 3.1 CRT variants cloned and tested for expression.

Construct / Organism	Uniprot ID	Expression
Plasmodium falciparum HB3 (137071)	Q9N623 (CRT_PLAFA_HB3)_Chloroquine resistance transporter	Yes
Plasmodium falciparum Dd2 (57267)	D5L5S2 (D5L5S2_PLAFA_Dd2)_Chloroquine resistance transporter	Yes
Plasmodium falciparum HB3 (137071)	Q9N623 (CRT_PLAFA_HB3)_CRT [codon optimized for X.laevis]	No
Plasmodium falciparum Dd2 (57267)	D5L5S2 (D5L5S2_PLAFA_Dd2)_CRT [codon optimized for X.laevis]	No
Plasmodium knowlesi H (5851)	Q9GSD7 (CRT_PLAKN_H)_Chloroquine resistance transporter	N/A
Toxoplasma gondii ME49 (508771)	B9Q9P9 (B9Q9P9_TOXGO_ME49)_Chloroquine resistance transporter	N/A
Plasmodium berghei ANKA (5823)	Q9GSD8 (CRT_PLABE_ANKA)_Chloroquine resistance transporter	N/A
Theileria parva Muguga (333668)	Q4N5R6 (Q4N5R6_THEPA_Muguga)_Chloroquine resistance transporter	N/A
Theileria annulata ANKA (353154)	Q4UDS9 (CRT_THEAN_ANKA)_Chloroquine resistance transporter	No
Cryptosporidium parvum Iowa II (353152)	Q7YZ23 (Q7YZ23_CRYPV_IowaII)_Chloroquine resistance transporter	No
Plasmodium vivax Sal-1 (126793)	Q9GSD3 (CRT_PLAVI_Sal-1)_Chloroquine resistance transporter	Yes
Plasmodium falciparum 7G8 (57266)	AF233064_putative chloroquine resistance transporter [Plasmodium falciparum 7G8]	Yes
Plasmodium vivax Sal-1 (126793)	Q9GSD3 (CRT_PLAVI_Sal-1)_CRT [codon optimized for S.frigiperda]	Yes

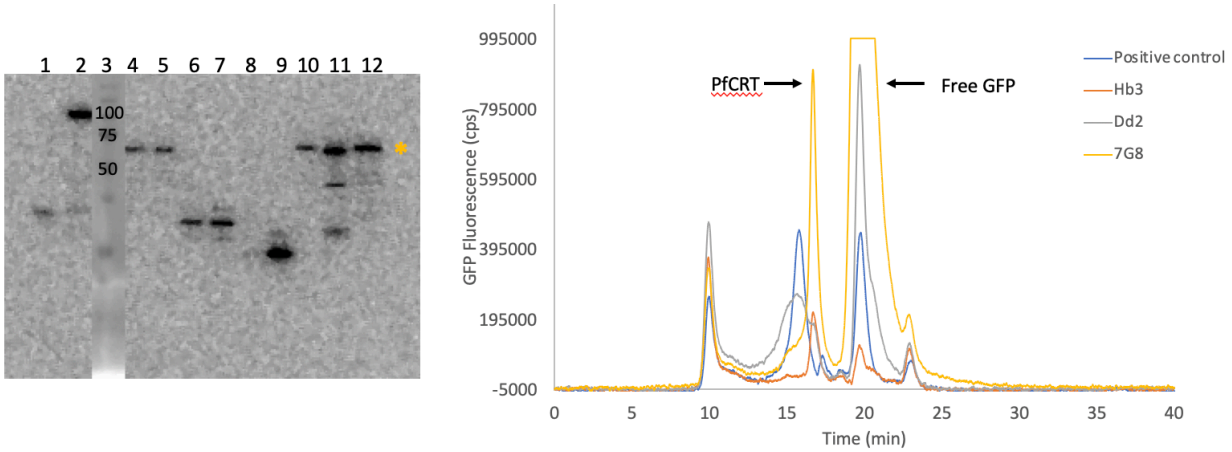

Figure 3.2 Expression and detergent stability screens of CRT variants. (left) anti-GFP western blot, where the molecular weight for CRT GFP fusion is marked by a yellow asterisk. Lanes are: 1 empty vector, 2 positive control (*D. rerio* STRA6), 3 MW markers, 4 PfCRT HB3, 5 PfCRT Dd2, 6 PfCRT HB3 codon optimized for *X. laevis*, 7 PfCRT Dd2 codon optimized for *X. laevis*, 8. *Theileria annulata* ANKA CRT, 9 *Cryptosporidium parvum* Iowa II CRT, 10 *P. vivax* Sal-1 CRT, 11 PfCRT 7G8, 12 *P. vivax* Sal-1 CRT codon optimized for Sf9 cells. (right) FSEC DDM elution profiles for the positive control (*D. rerio* STRA6), HB3, Dd2 and 7G8 PfCRT.

The expression of PfCRT 7G8 was tested in various systems including baculovirus infection of insect cells, transient transfection of mammalian cells with polyethylenimine (PEI) [98], and baculovirus transduction of mammalian cells (BacMam system). Based on the protein yield, the BacMam system was used for further optimization. The BacMam system employs a modified insect baculovirus, encoding the target gene of interest, to transduce HEK293 cells lacking N-acetylglucosaminyltransferase I (GnTi$^-$) where the constitutively active CMV promoter drives expression [99, 100]. Also, the addition of a histone deacetylase inhibitor like sodium butyrate in the BacMam system was used to enhance protein expression [99].

To test and optimize the expression level of PfCRT 7G8 isoform with the BacMam system, I transduced 100 mL HEK293 GnTi- cells at 2.0 million cells per mL with a fixed amount of virus (1:10 v/v between virus to culture) varying three conditions: temperature after the addition of 10 mM sodium butyrate (30 °C and 37 °C), time point on the addition of 10 mM

sodium butyrate post transduction (8 hours versus 24 hours), and time point on harvest (2 days versus 3 days). Cell pellets of each condition were solubilized in DDM, nickel purified, and loaded on an analytical Superdex 200 Increase 5/150 GL column (GE Healthcare) for high performance liquid chromatography (HPLC). The condition at 37 °C, sodium butyrate 8 hours after transduction, and harvest after 2 days produced the highest yield of protein (**Fig. 3.3**). Subsequently, I was able to obtain 0.4-0.6 mg of PfCRT 7G8 per 800mL of transduced cells. The enhanced expression of PfCRT was instrumental in allowing us to screen further purification conditions.

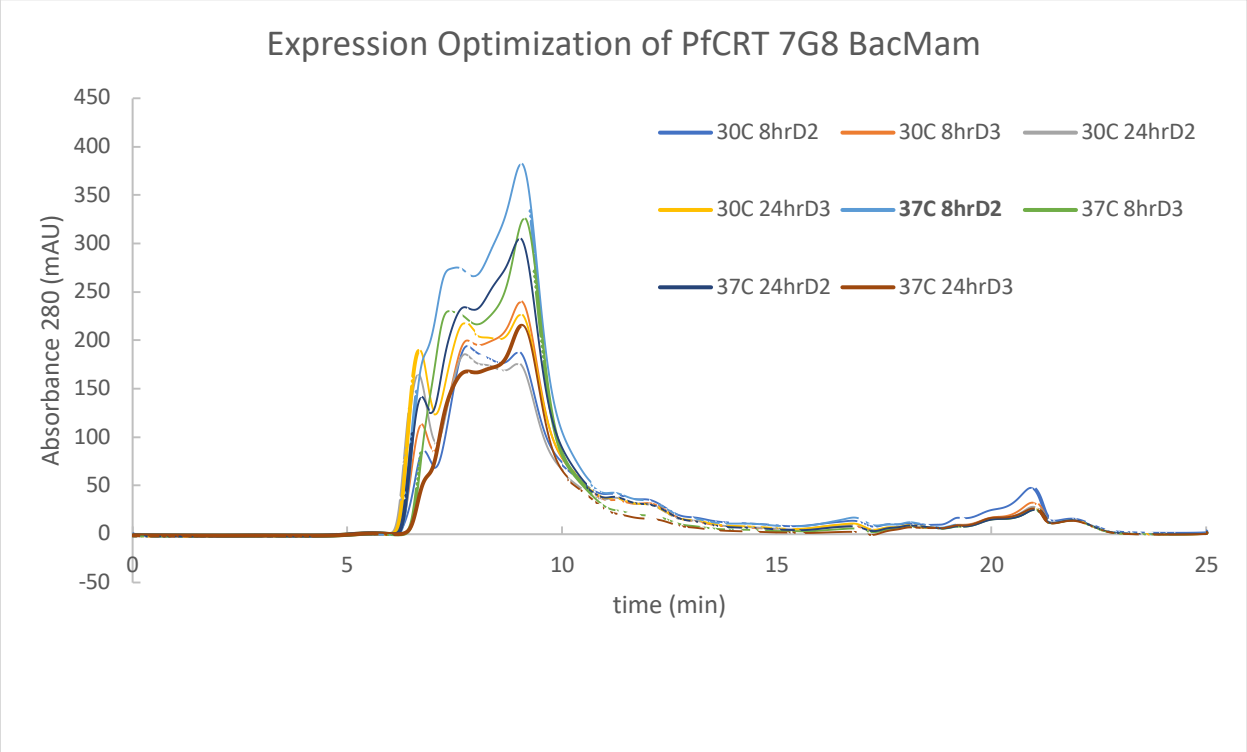

Figure 3.3 PfCRT 7G8 expression optimization. Small-scale cultures of cells were transduced with fixed amount of baculovirus and 10 mM sodium concentration. The time of sodium butyrate addition was tested at 8 h or 24 h post transduction at two temperature points (30 °C or 37 °C) upon the addition of sodium butyrate. The harvest time after the addition of sodium butyrate was tested between 2 days or 3 days. The nickel purified sample of each condition was loaded and evaluated by an analytical gel filtration column Superdex 200 Increase 5/150 with high performance liquid chromatography (HPLC). The best expression condition is bolded in the legend.

3.3 Detergent and Stability Screen of PfCRT 7G8

The initial expression and stability screen shown in Section **3.2** was performed using the nonionic detergent, dodecyl-maltoside (DDM), which is a mild detergent that is commonly used to extract and solubilize membrane proteins. To find more stable purification conditions for PfCRT 7G8, other detergents were examined in the absence or presence of cholestryl hemisuccinate (CHS). CHS has been shown to improve the stability of G protein-coupled receptors and has been commonly used in stabilizing membrane proteins during purification [101]. The nickel purified samples were loaded on to an analytical Superdex 200 Increase 5/150 GL column (GE Healthcare) for gel filtration on HPLC. The screen results demonstrate a substantial improvement in stability of PfCRT 7G8 in DDM with the addition of CHS (**Fig. 3.4**). Therefore, DDM/CHS (10:1 w/w) was used for the remaining of the experiment. This result was consistent with a recently published paper on the purification of truncated PfCRT HB3 CQ-sensitive isoform [102].

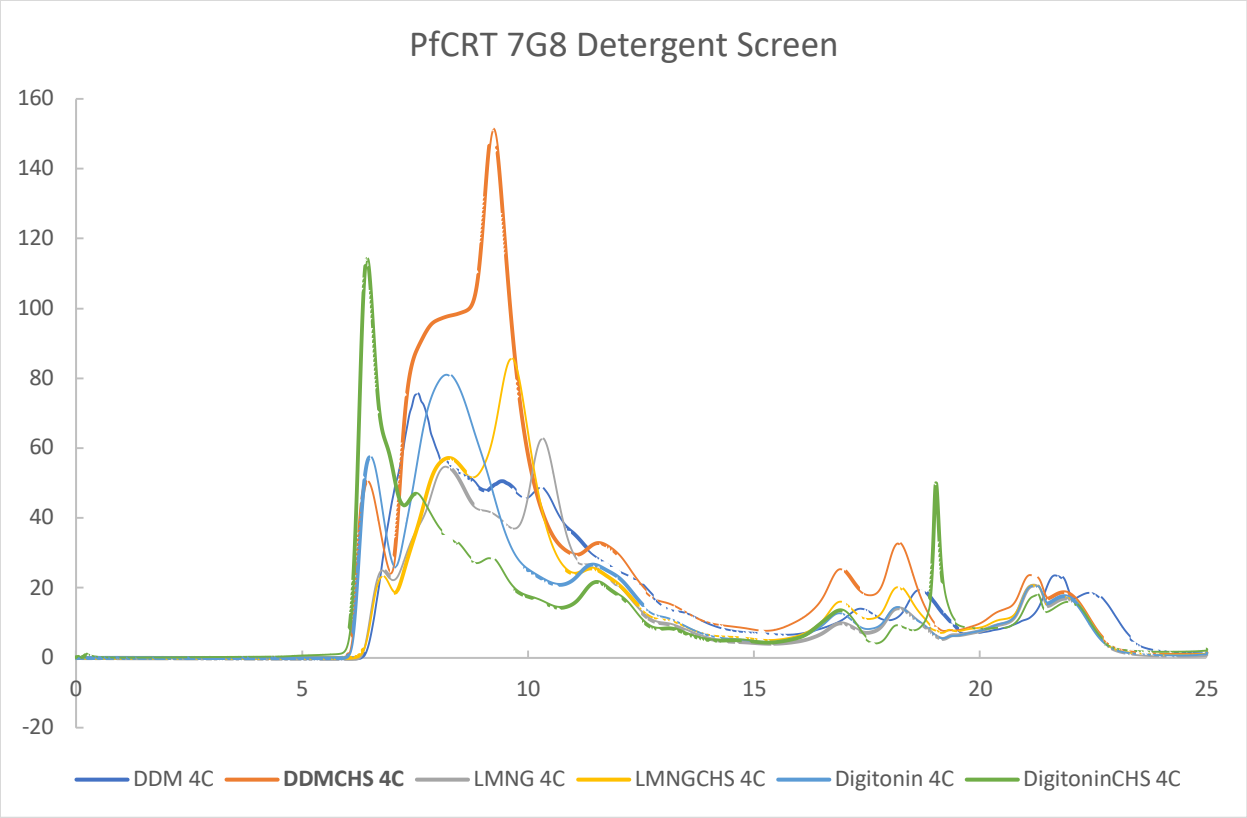

Figure 3.4 Detergent Screen for PfCRT 7G8. Nickel purified samples in various detergents were evaluated by an analytical gel filtration column (Superdex 200 Increase 5/150 GL column) on high performance liquid chromatography (HPLC). Cholestryl hemisuccinate (CHS); DDM n-Dodecyl-β-D-Maltopyranoside; LMNG Lauryl Maltose Neopentyl Glycol and Digitonin. The optimal condition is bolded in the legend.

3.4 Reconstitution of PfCRT 7G8 into Nanodiscs

Once the expression and stability of the PfCRT 7G8 in DDM/CHS had been optimized, initial attempts to crystallize the PfCRT 7G8 were performed. However, when we attempted to concentrate the purified sample beyond 2mg/mL, the protein was unstable in detergent solution and precipitated, which made setting up trays for crystallization challenging. Additionally, the level of purity, based on SDS-PAGE gel analysis, after metal affinity chromatography followed by size exclusion chromatography in buffer containing detergent, was not optimal for crystallization. To resolve these issues, I reconstituted detergent purified PfCRT 7G8 into

nanodiscs. Nanodiscs consist of two copies of amphipathic membrane scaffolding proteins (MSP) encircling a target protein embedded in a bilayer of phospholipids [103]. The nanodiscs mimic a native lipid bilayer environment, in which the protein is more stable, soluble and provides homogenous particles of defined size and composition. A second metal affinity chromatography step was introduced after the reconstitution into nanodiscs in order to remove excess free empty nanodisc and further improve sample purity (**Fig. 3.5**). In result, the reconstitution of PfCRT 7G8 into nanodiscs enhanced both purity and stability (data shown in the manuscript **Extended Data Fig. 2**)

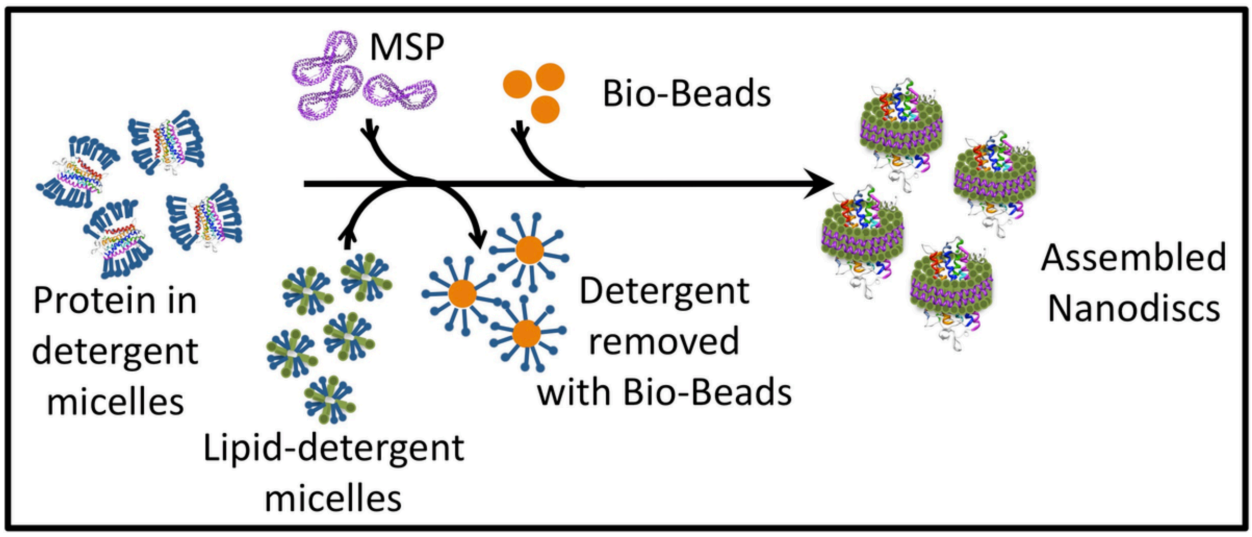

Figure 3.5 Schematic representation of nanodisc assembly. Nanodiscs assembly requires a target membrane protein to be extracted from native lipid bilayers in the presence of detergent, to which membrane scaffold proteins (MSP) and phospholipids are added into purified protein in solution containing detergent. Detergent is removed upon the addition of bio-beads while protein is incorporated into nanodisc bilayers. Figure adapted from https://www.labome.com/method/Nanodiscs-Membrane-Protein-Research-in-Near-Native-Conditions.html.

3.5 Structural Elucidation of PfCRT 7G8

As an alternative to x-ray crystallography, we used cryo-EM to determine the structure of PfCRT 7G8. The primary challenge in solving the PfCRT structure using cryo-EM was that the

size of the protein (49kDa) is well below the average size of macromolecules amenable for cryo-EM analysis despite recent advances in the field. Also, based on protein structure predictions the majority of protein was anticipated to be embedded in the lipid bilayer [43], and a lack of soluble features would make it difficult to align particles in cryo-EM analysis. To overcome these challenges, we collaborated with the Kossiakoff laboratory at the University of Chicago to raise and select 50-kDa antigen-binding fragments (Fab) which bind specifically to PfCRT to increase the size of the protein particle and to provide soluble features to help particle alignment in cryo-EM analysis. We reconstituted PfCRT 7G8 into biotinylated nanodiscs and sent the sample off to the Kossiakoff laboratory. The Kossiakoff laboratory has developed a technique where they screen a phage display library to select a Fab that binds to the target protein with high affinity [104]. Subsequently, 4 Fab candidates were obtained for complex formation. Based on the binding affinity, which was determined using ELISA (data shown in the manuscript **Extended Data Fig. 2)**, I chose the 7G8-CTC Fab as it has the highest affinity. I further confirmed that PfCRT 7G8 and the CTC Fab form a stable complex using size exclusion chromatograph and negative stain EM (data shown in the manuscript **Extended Data Fig. 2 and 3)**.

I will now present the manuscript "Structure of the *Plasmodium falciparum* Pleiotropic Drug Resistance Transporter PfCRT", that is currently under review in Nature. This manuscript demonstrates for the first time the structure of PfCRT and provides greater insight into where antimalarial drugs (CQ and PPQ) might bind. Also, we show the location of clinical mutations causing drug resistance in our structural model, and further reveal that PfCRT transports drug in the presence of both a membrane potential and a pH gradient. Finally, we propose that arginine is a potential substrate for CQ-resistant isoforms of PfCRT under physiological conditions.

References

43. Martin, R.E. and K. Kirk, *The malaria parasite's chloroquine resistance transporter is a member of the drug/metabolite transporter superfamily.* Mol Biol Evol, 2004. **21**(10): p. 1938-49.
95. Reeves, D.C., et al., *Chloroquine-resistant isoforms of the Plasmodium falciparum chloroquine resistance transporter acidify lysosomal pH in HEK293 cells more than chloroquine-sensitive isoforms.* Mol Biochem Parasitol, 2006. **150**(2): p. 288-99.
96. Mancia, F. and J. Love, *High-throughput expression and purification of membrane proteins.* J Struct Biol, 2010. **172**(1): p. 85-93.
97. Kawate, T. and E. Gouaux, *Fluorescence-detection size-exclusion chromatography for precrystallization screening of integral membrane proteins.* Structure, 2006. **14**(4): p. 673-81.
98. Longo, P.A., et al., *Transient mammalian cell transfection with polyethylenimine (PEI).* Methods Enzymol, 2013. **529**: p. 227-40.
99. Goehring, A., et al., *Screening and large-scale expression of membrane proteins in mammalian cells for structural studies.* Nat Protoc, 2014. **9**(11): p. 2574-85.
100. Dukkipati, A., et al., *BacMam system for high-level expression of recombinant soluble and membrane glycoproteins for structural studies.* Protein Expr Purif, 2008. **62**(2): p. 160-70.
101. Grisshammer, R., *Purification of recombinant G-protein-coupled receptors.* Methods Enzymol, 2009. **463**: p. 631-45.
102. Wright, D.J., M. O'Reilly, and D. Tisi, *Engineering and purification of a thermostable, high-yield, variant of PfCRT, the Plasmodium falciparum chloroquine resistance transporter.* Protein Expr Purif, 2018. **141**: p. 7-18.
103. Bayburt, T.H. and S.G. Sligar, *Membrane protein assembly into Nanodiscs.* FEBS Lett, 2010. **584**(9): p. 1721-7.
104. Dominik, P.K. and A.A. Kossiakoff, *Phage display selections for affinity reagents to membrane proteins in nanodiscs.* Methods Enzymol, 2015. **557**: p. 219-45.

Structure of the *Plasmodium falciparum* Pleiotropic Drug Resistance Transporter PfCRT

Jonathan Kim[1,10], Yong Zi Tan[1,2,10], Satchal K. Erramilli[3], Kathryn J. Wicht[4], Audrey L. Warren[5], Sabrina I. Giacometti[1], Satish K. Dhingra[4], John Okombo[4], Kamil Nosol[3], Paul D. Roepe[6], Clinton S. Potter[2,7], Bridget Carragher[2,7], Anthony A. Kossiakoff[3], Matthias Quick[5,8*], David A. Fidock[4,9*], Filippo Mancia[1*]

Affiliations:

[1]Department of Physiology and Cellular Biophysics, Columbia University Irving Medical Center, New York, NY 10032, USA.

[2]National Resource for Automated Molecular Microscopy, Simons Electron Microscopy Center, New York Structural Biology Center, New York, NY 10027, USA.

[3]Department of Biochemistry and Molecular Biology, University of Chicago, Chicago, IL 60637, USA.

[4]Department of Microbiology and Immunology, Columbia University Irving Medical Center, New York, NY 10032, USA.

[5]Division of Molecular Therapeutics, New York State Psychiatric Institute, New York, NY 10032, USA.

[6]Department of Chemistry and Department of Biochemistry and Cellular and Molecular Biology, Georgetown University, Washington DC, 20057, USA.

[7]Department of Biochemistry and Molecular Biophysics, Columbia University Irving Medical Center, New York, NY 10032, USA.

[8]Center for Molecular Recognition, Department of Psychiatry, Columbia University Irving Medical Center, New York, NY 10032, USA.

[9]Division of Infectious Diseases, Department of Medicine, Columbia University Irving Medical Center, New York, NY 10032, USA.

[10]These authors contributed equally: Jonathan Kim, Yong Zi Tan.

*Correspondence to be addressed to: mq2102@cumc.columbia.edu (M.Q.); df2260@columbia.edu (D.A.F.); fm123@cumc.columbia.edu (F.M.).

Keywords: Malaria, single-particle cryo-electron microscopy, antibody phage display, fragment antigen-binding, nanodisc, transport, resistance, chloroquine, piperaquine

Summary: The emergence and spread of drug-resistant *Plasmodium falciparum* has been a major setback in efforts to control and eliminate malaria. For decades, treatment relied on chloroquine (CQ), a safe and affordable 4-aminoquinoline that was highly effective against pathogenic intra-erythrocytic asexual blood-stage (ABS) parasites until resistance arose and spread, with devastating consequences in Africa[1]. Resistance to the chemically related current first-line combination drug piperaquine (PPQ) has also recently emerged, thwarting its treatment efficacy in Southeast Asia. Resistance to both CQ and PPQ has been associated with distinct sets of point mutations in the 49 kDa *P. falciparum* chloroquine resistance transporter PfCRT[2], a member of the drug/metabolite transporter (DMT) superfamily[3], which resides within the digestive vacuole (DV) membrane of the parasite. Here we present the structure of the PfCRT CQ-resistant, PPQ-sensitive 7G8 isoform to 3.2 Å resolution, determined using fragment antigen-binding technology and single-particle cryo-electron microscopy. Mutations contributing to resistance to CQ and PPQ map to a central cavity, implicating this as the major site of drug interaction. Binding and transport studies reveal that the 7G8 isoform binds both drugs, and mediates transport of CQ and of the positively charged amino acid arginine in a membrane potential- and pH-dependent manner. These data provide the first atomic-level insights into the molecular mechanism of this key mediator of antimalarial treatment failures.

Recent reductions in the global malaria burden have stalled in the past 2-3 years, with the situation in Southeast Asia exacerbated by emerging resistance to artemisinin-based combination therapies including the bis-4-aminoquinoline partner drug PPQ[4-6]. A major determinant of drug resistance in *Plasmodium falciparum* malaria parasites is the 49 kDa putative transporter PfCRT. Amino acid substitutions in this protein group as haplotypes that originated independently decades ago in several regions subjected to intense drug pressure with the former gold-standard antimalarial, CQ. These include the 5-amino acid 7G8 variant that dominates in South America and the Western Pacific, and the 8-amino acid Dd2 variant that is prevalent in Southeast Asia and that is thought to have seeded the introduction of mutant PfCRT and CQ resistance into Africa (**Extended Data Fig. 1**). Extensive use of PPQ in Cambodia is suspected to have recently driven the rapid emergence of novel PfCRT mutations, arising in the Dd2 isoform[7]. For CQ, resistance has been attributed to mutant PfCRT-mediated efflux of drug out of the DV (**Fig. 1a**). It remains unclear whether this mechanism would apply to PPQ[8-12]. CQ and PPQ are thought to act by accumulating in the ABS parasite's acidic DV as protonated species that bind toxic Fe^{3+} heme (ferri-protoporphyrin IX; FPIX) and inhibit heme incorporation into chemically inert hemozoin crystals[13, 14]. FPIX is released following parasite-mediated proteolysis of host hemoglobin (Hb) that is endocytosed into the DV.

To explore the structural basis of PfCRT-mediated drug resistance, we used single-particle cryo-electron microscopy (cryo-EM) to determine the structure of the 49 kDa 7G8 PfCRT. To overcome current cryo-EM size limitations[15], we screened a synthetic phage display library[16] to select for recombinant PfCRT-specific antigen-binding fragments (Fabs, ~50 kDa) to form a stable PfCRT-Fab complex (**Extended Data Fig. 2 and 3**). The cryo-EM reconstruction of the nanodisc-incorporated 7G8 PfCRT-Fab complex was determined to a nominal resolution of 3.3 Å, with the PfCRT portion resolved to 3.2 Å (**Extended Data Table 1 and Extended Data Fig. 4**). Using this map, a *de novo* model of PfCRT was built comprising residues 47-113 and 123-405 of the 424-amino acid protein (**Fig. 1b, c and Extended Data Fig. 4, 5**). PfCRT is monomeric and consists of 10 transmembrane (TM) helices with both termini located on the cytosolic side (**Fig. 1b**). Two juxtamembrane helices (JM1 and JM2), parallel to the DV membrane on opposite sides, are located at the N-terminus and between TM helices 7 and 8, respectively (**Fig. 1b**). The 10 TMs are arranged as five helical pairs that form two-helix hairpins with an inverted topology, whereby the N-termini of helices 1-5 pair on the same side of the DV membrane as the C-termini of helices 6-10 (**Fig. 1b, c and Extended Data Fig. 6**). The structure of PfCRT is similar to Vrg4 (PDB ID: 5OGE/5OGK;[17]), YddG (PDB ID: 5I20;[18]) and TPT (PDB ID: 5Y78/5Y79;[19]), which are also DMTs (**Extended Data Fig. 7A**).

TM helices 1–4 and 6–9 form a central cavity of ~ 3,300 $Å^3$ that is wider on the DV side of the protein and closes approximately halfway into the membrane, suggesting that the structure is in an open-to-DV/inward-open state conformation (**Fig. 2a**). The corresponding cavity in Vrg4, TPT and YddG constitutes the known ligand-binding site (**Extended Data Fig. 7b**), predicting that this cavity is also the ligand-binding site for PfCRT. The net charge in the PfCRT cavity is negative, determined mainly by the aspartate residues D137, D326 and D329 (**Fig. 2a**). In contrast, both Vrg4 and TPT have a positively charged cavity, whereas that of YddG is neutral (**Extended Data Fig. 7b**). These electrostatic profiles suggest that putative substrates for PfCRT are likely positively charged, in contrast to those of the other three DMTs cited. Consistent with

this proposal, the positively charged residue arginine R111 in the variable loop region of our selected Fab occupies the predicted binding site in the cavity of PfCRT (**Fig. 2b**). Interactions between the Fab R111 and PfCRT D326 and D329 presumably help stabilize the PfCRT-Fab complex (**Fig. 2b**).

Alignment of the PfCRT sequence with *Plasmodia* and other Apicomplexan orthologs reveals extensive sequence conservation within the helices that line the cavity, as well as the adjacent TM5 / TM10 inverted helices that are separate from the cavity (**Fig. 2c and Extended Data Fig. 8**). None of the PfCRT mutations associated with CQ or PPQ resistance mapped to residues that were fully conserved across our set of Apicomplexan CRT orthologs (**Extended Data Fig. 8**), suggesting structural and/or functional constraints. We also identified density in a separate cleft region, delineated by JM1, TM1, TM9 and TM10, near the cytosolic side of the DV membrane. We tentatively assigned this density to cholesterol hemisuccinate, present during the purification (**Extended Data Fig. 9**). This hydrophobic cleft is absent in the other DMT superfamily members cited above, which also lack JM1.

Extensive conservation was also observed in JM2 and the ensuing long loop connecting TM helices 7 and 8. This loop, extending into the DV, consists of four highly conserved cysteines that likely form two disulfide bridges (**Fig. 2c, d and Extended Data Fig. 8**), suggesting that this particular region might be involved in redox sensing through formation of reversible disulfide bonds[20]. A role for PfCRT in redox sensing is plausible given the release in the acidic DV (pH 5.2-5.5) of Hb-derived Fe^{2+}-protoporphyrin IX, whose oxidation to the Fe^{3+} state produces reactive oxygen species[21].

The structure of PfCRT provides key insights into how mutations can confer resistance to CQ and PPQ (**Fig. 3a**). All CQ-R isoforms, irrespective of geographic origin, share a common and requisite K76T mutation, substituting a positive lysine that is believed to repel CQ^{2+} for an uncharged threonine[9, 22]. Our structure places residue 76 directly in the lining of the central cavity (**Fig. 3b**). The CQ-R 7G8 isoform has four additional mutations (C72S, A220S, N326D, I356L; compared with the canonical wild-type CQS 3D7 isoform), which also line the cavity (**Fig. 3b**), supporting this region as the primary site of CQ interactions. Indeed, this cavity, with a ~25Å maximum diameter, is in principle able to accommodate CQ or PPQ (~14 and ~21Å maximum lengths, respectively). The C350R mutation, which reverses CQ resistance when added to 7G8[23], also resides in this cavity where presumably the introduction of the positive Arg residue minimizes interactions with CQ^{2+}. Similarly, the CQ-R Dd2 isoform has six (M74I, N75E, K76T, A220S, N326S, I356T) of its eight mutations located within the cavity, with two additional mutations (Q271E and R371I) located at its entrance (**Fig 3b and Extended Data Fig. 1b**).

Our structural data support a primary role for PfCRT in PPQ resistance, with the associated amino acid substitutions lining the cavity (including C350R that arose on the 7G8 isoform; as well as H97Y, F145I, and G353V that emerged on the Dd2 isoform; **Fig. 3b**). The high-grade resistance mutation F145I resides close to the cavity entrance, and both H97Y and G353V are in line with the plane of CQ-R mutations. M343L, which confers low-grade PPQ resistance in the Dd2 isoform, lies above the cavity, close to the cytosol. Almost all mutations that promote PPQ

resistance in Dd2 parasites result in at least some loss of CQ resistance, suggesting differences in CQ and PPQ binding and transport (**Fig. 3b and Extended Data Fig. 1a**;[7]).

Using scintillation proximity-based assays[24] on structurally-validated purified protein reconstituted in nanodiscs, we found that PfCRT 7G8 binds both CQ and PPQ (**Fig. 4a**). Isotopic dilution assays yielded mean half-maximal binding constants of ~300 nM for CQ, similar to earlier studies with Dd2 PfCRT[25, 26], and ~190 nM for PPQ (**Fig. 4b**). Each drug competitively inhibited the binding of the other with virtually identical mean half-maximal inhibition constants (IC_{50} values) of ~170 nM (**Fig. 4c**).

Binding of these two drugs was partially inhibited by verapamil (**Fig. 4d**), a known CQ resistance reversal agent that has been reported to inhibit CQ transport by resistant parasites[27]. Near-complete inhibition was observed with amodiaquine, a related 4-aminoquinoline first-line partner drug against which PfCRT 7G8 mediates cross resistance[28], implying similar drug occupancies in the PfCRT cavity. Control assays found no inhibition for [^{3}H]-CQ or [^{3}H]-PPQ binding with the structurally unrelated antimalarial drugs lumefantrine and atovaquone that have separate modes of action. No [^{3}H]-CQ or [^{3}H]-PPQ binding was observed with the unrelated transporter LeuT[29].

We also examined drug uptake using protein reconstituted in proteoliposomes, which allowed us to investigate energetic requirements for transport. Our data showed that active [^{3}H]-CQ uptake required an inwardly directed pH gradient (pH 5.5-7.5, corresponding to the gradient observed in the DV of the parasites[30]), and a membrane potential $\triangle\Psi$ (**Extended Data Fig. 10a).** Here, $\triangle\Psi$ was created by an outward-directed K^+ diffusion gradient from the proteoliposomes in the presence of the K^+-specific ionophore valinomycin. Using these conditions, we observed [^{3}H]-CQ uptake, peaking within one minute (**Fig. 4e**). These results support proton motive force-dependent CQ efflux as the mechanism underlying mutant PfCRT 7G8-mediated CQ resistance, and are consistent with earlier reports[10-12, 25, 27, 31]. Under our experimental conditions, no detectable uptake was observed with [^{3}H]-PPQ, as expected for this PPQ-S isoform (**Fig. 4e**).

Based on the observed interaction between the Fab R111 and the cavity of PfCRT (**Fig. 2b**), earlier evidence that mutant PfCRT isoforms can result in excess accumulation of Hb-derived peptides in the DV[32, 33], the cationic nature of putative PfCRT substrates, and prior transport studies[34], we also tested the inhibition of Arg on [^{3}H]-CQ binding. Indeed, this positively charged amino acid inhibited [^{3}H]-CQ binding, whereas control experiments using Leu revealed no interaction of this amino acid with PfCRT 7G8 (**Fig. 4d**). We also assayed for Arg as a potential transported substrate for PfCRT. Like CQ, [^{3}H]-Arg uptake in proteoliposomes required a pH gradient and a $\triangle\Psi$ (**Extended Data Fig. 10b**), and its accumulation peaked within one minute (**Fig 4e**). Scintillation proximity-based binding revealed that [^{3}H]-Arg binds to PfCRT 7G8 (**Extended Data Fig. 10c**), with a half-maximal binding constant of ~400 μM (**Extended Data Fig. 10d**). Binding of [^{3}H]-Arg was effectively competed by both CQ and PPQ, as well as by amodiaquine and non-radiolabeled Arg or Lys. In contrast, the aliphatic amino acid Leu failed to inhibit [^{3}H]-Arg binding (**Extended Data Fig. 10e**). Binding of [^{3}H]-Arg, [^{3}H]-CQ and [^{3}H]-PPQ was competed by the Fab in a concentration-dependent manner (**Fig. 4f**),

indicating overlapping binding of Arg, CQ, PPQ and the Fab to the PfCRT cavity. In our proteoliposome uptake assays, we also observed partial to strong inhibition of [^{3}H]-CQ and [^{3}H]-Arg uptake by verapamil and 4-aminoquinolines, at levels similar to those observed in the binding assays (**Fig. 4g and Extended Data Fig. 10e**). These data further implicate a crucial role for the central cavity in dictating PfCRT 7G8-mediated binding and transport.

In summary, our 3.2 Å resolution cryo-EM structure reveals that mutations previously identified to be involved in antimalarial drug resistance surround a central cavity, implicating this as the likely site of parasite protein interaction leading to resistance to these drugs. Moreover, we show that PfCRT mediates binding and transport of the 4-aminoquinoline CQ and positively charged amino acids in the presence of both membrane potential and pH gradients as driving forces. Our binding data and mutational analysis also support emerging PfCRT mutations as drivers of high-grade PPQ resistance. These results create new tools and perspectives to further elucidate PfCRT function and its relation to drug binding and transport, and to assess whether inhibition of PfCRT itself can be leveraged as a strategy to overcome its ability to mutate and mediate parasite resistance to first-line antimalarial drugs.

Figure 1

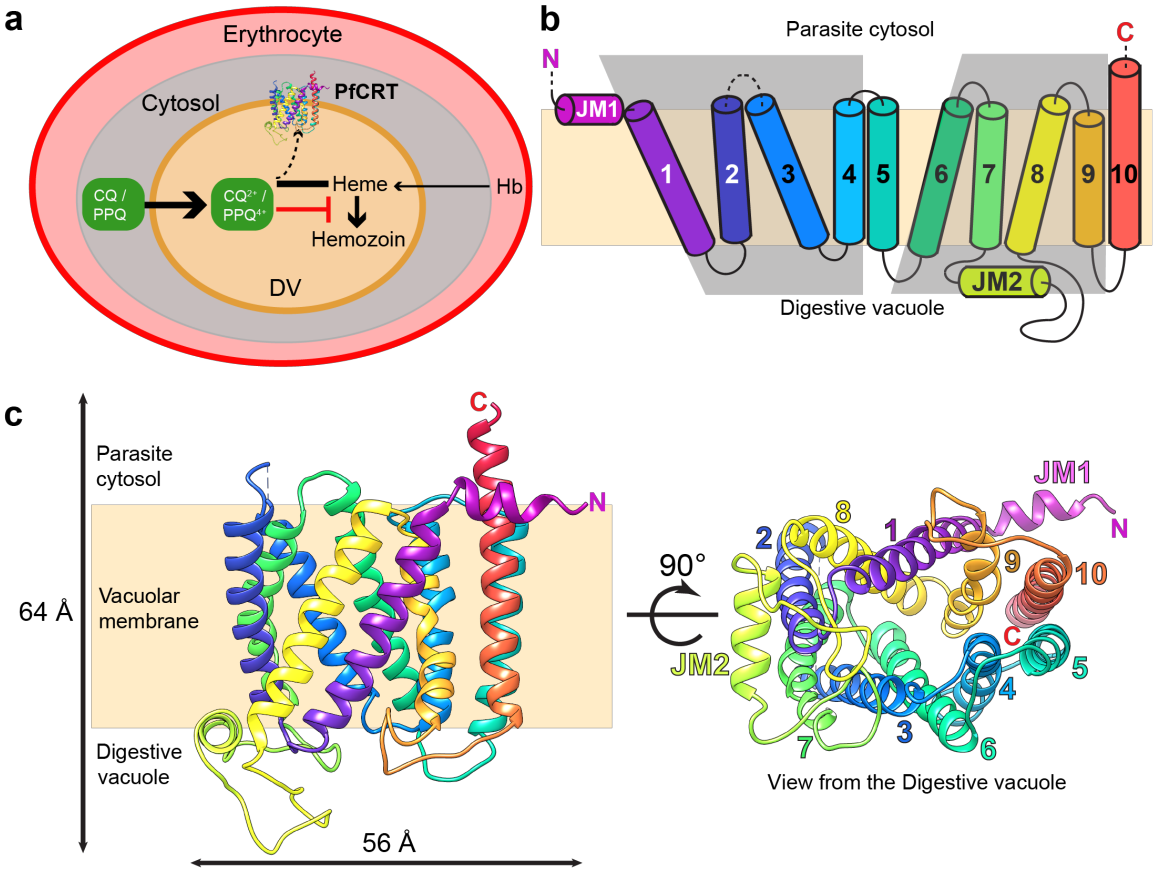

Figure 1 | Single-particle cryo-EM structure of PfCRT 7G8. a, PfCRT (PlasmoDB ID PF3D7_0709000) is localized within the membrane of the *P. falciparum* intra-erythrocytic parasite's digestive vacuole (DV), wherein imported host hemoglobin (Hb) is catabolized and toxic free heme is released. The related 4-aminoquinoline antimalarial drugs chloroquine (CQ) and piperaquine (PPQ) are believed to bind heme and prevent its incorporation into inert hemozoin[9, 14]. PfCRT is thought to efflux CQ out of the DV into the cytosol away from its heme target. **b,** Topology of PfCRT with disordered regions shown as dotted lines. Transmembrane helices are numbered 1 to 10, while the juxtamembrane helices (JM) are labeled JM1 and JM2. **c,** 3.2 Å cryo-EM structure of PfCRT 7G8, with the 10 transmembrane helices colored in rainbow. The N- and C- termini are labeled. The right panel shows a 90° rotation with helices numbered, as viewed from the DV side.

Figure 2

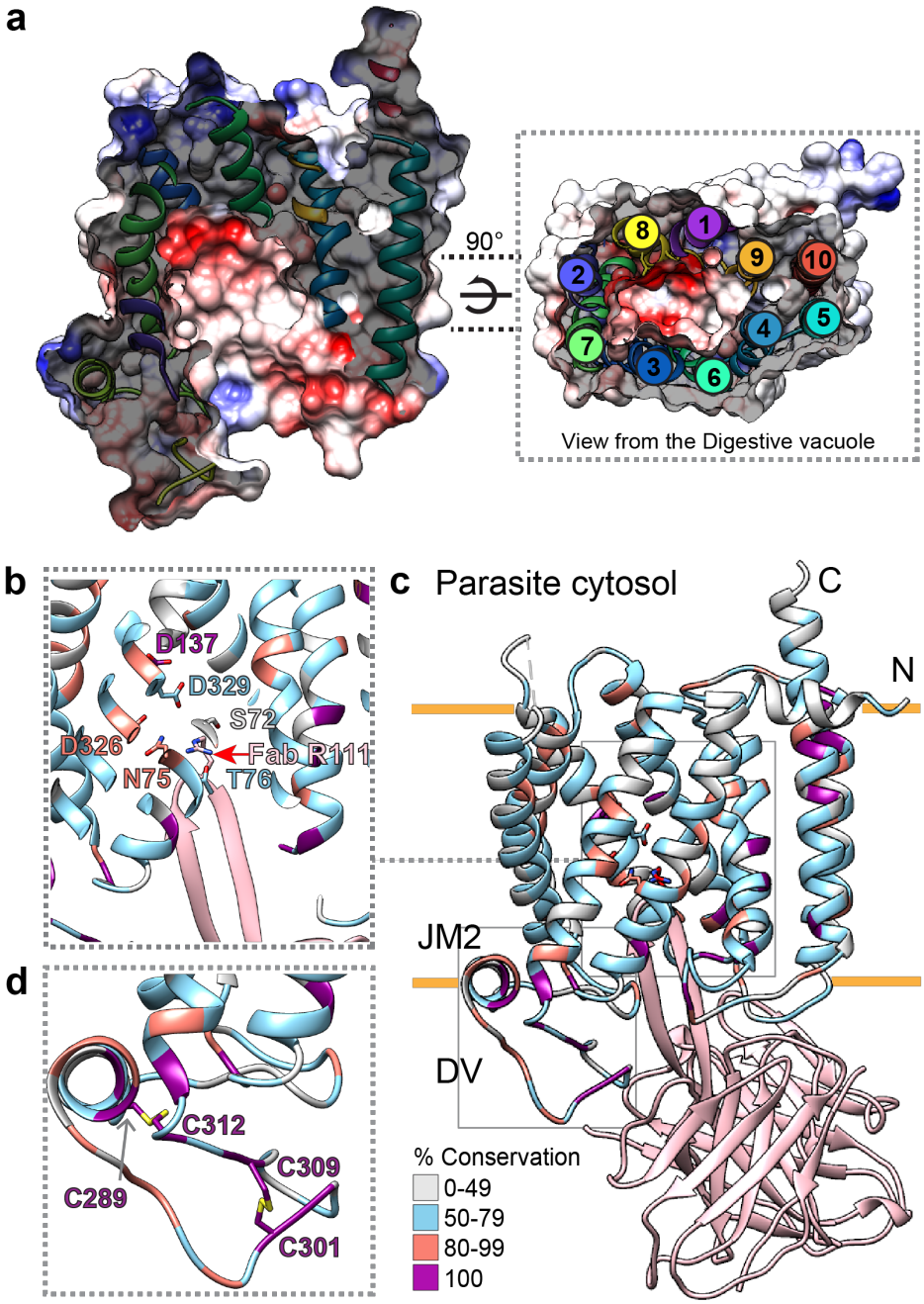
a
90°
1
2
3
4
5
6
7
8
9
10
View from the Digestive vacuole
b
D137
D329
S72
D326
Fab R111
N75
T76
c
Parasite cytosol
C
N
JM2
DV
% Conservation
0-49
50-79
80-99
100
d
C312
C309
C289
C301

Figure 2 | Structural features of PfCRT. a, Surface representation of the electrostatic potential of the central cavity with red and blue being negatively and positively charged, respectively. On the right, a central slice through the structure (dotted lines) as an insert shows the arrangement of transmembrane helices, which are labeled from N- to C-terminus. **b,** Interaction between the CTC Fab and PfCRT 7G8. PfCRT is rendered in cartoon and colored based on conservation. Residues in PfCRT 7G8 that are proximal to R111 in the Fab variable region (pink and red arrowed) are colored on the basis of their conservation in our selected panel of Apicomplexan parasites (Extended Data Fig. 9 and 10). **c,** PfCRT and Fab are rendered in cartoon and colored in conservation and pink, respectively. **d,** Cysteine residues that likely form disulfide bonds at the region between TM7 and TM8 are shown in yellow and rendered as sticks.

Figure 3

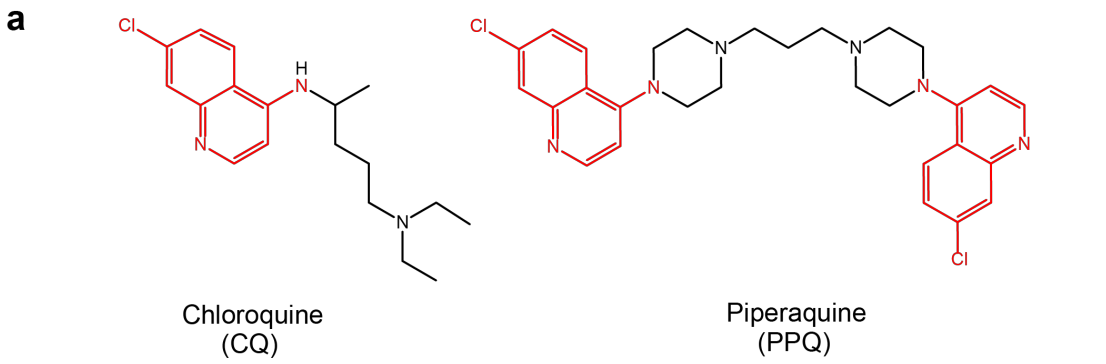

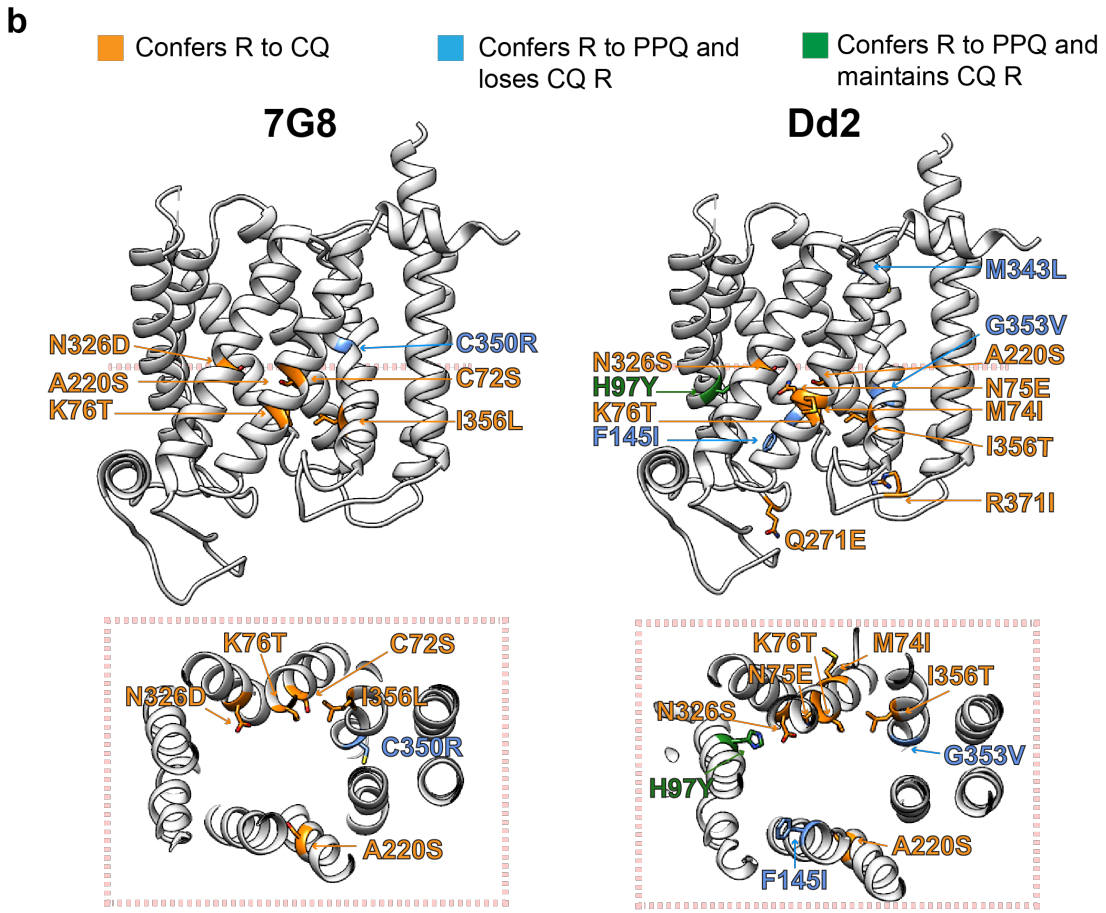

Figure 3 | Mapping of mutations onto the PfCRT structure. a, Chemical structures of CQ and PPQ. **b,** Residues known to contribute to resistance to CQ and PPQ have their side chains rendered as sticks and are colored based on their resistance profiles. The remaining structure is rendered in cartoon and colored in grey. Highlighted residues are topologically represented in **Extended Data Fig. 1**. Mutations in the 7G8 and Dd2 regional haplotypes of PfCRT (**Extended Data Fig. 1 and Extended Data Table 2**) are colored, using the atomic model for the solved 7G8 structure.

Figure 4

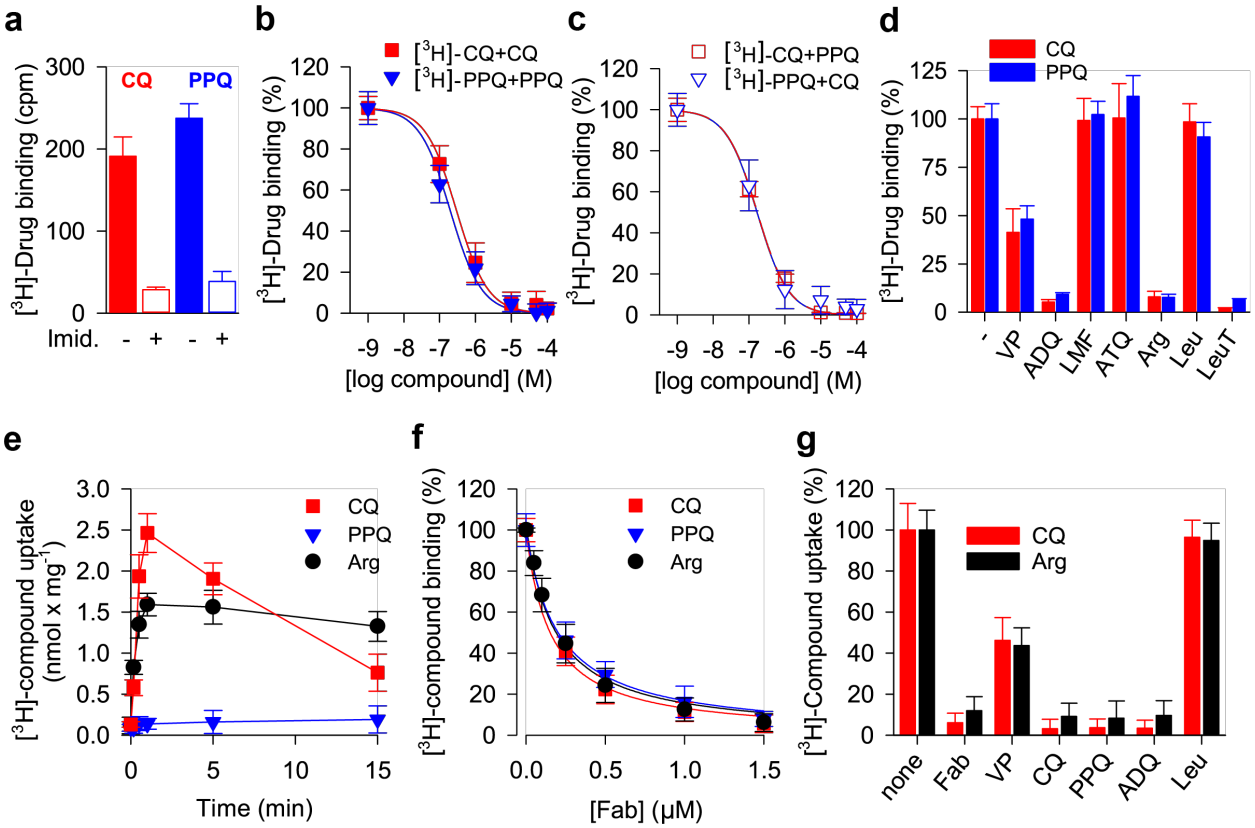

Figure 4 | Functional characterization of PfCRT 7G8. a, Binding of 370 nM [^{3}H]-CQ (red) or 75 nM [^{3}H]-PPQ (blue) to PfCRT 7G8 ± imidazole (Imid.; data are means±SEM; N,n=3,3). **b,** Isotopic dilution of [^{3}H]-CQ (■) or [^{3}H]-PPQ (▼) revealed Log*EC*$_{50}$ of -6.53 ± 0.04 M and -6.70 ± 0.05 M (corresponding to means of 296.5 nM CQ and 189.6 nM PPQ), respectively. **c,** Competition of [^{3}H]-CQ (□) or [^{3}H]-PPQ (▽) binding with non-radiolabeled PPQ or CQ, respectively, revealed Log*IC*$_{50}$ values of -6.77 ± 0.03 M and -6.78 ± 0.06 M (corresponding to means of 170.9 nM and 167.3 nM), respectively. **d,** Specific binding of [^{3}H]-CQ or [^{3}H]-PPQ performed in the absence (-) or presence of 10 µM verapamil (VP), 1 µM amodiaquine (ADQ), 10 µM lumefantrine (LMF) or atovaquone (ATQ), or 1 mM Arg or Leu. Nanodiscs containing LeuT[29] served as control. **e,** Time course of 93 nM [^{3}H]-CQ, 75 nM [^{3}H]-PPQ, or 125 nM [^{3}H]-Arg, uptake measured with 7G8 PfCRT-containing proteoliposomes (PLs). Data are mean±SEM; N,n=2,3. **f,** Fab binding to the PfCRT 7G8 isoform reduces binding of 250 nM [^{3}H]-Arg, 370 nM [^{3}H]-CQ, or 75 nM [^{3}H]-PPQ in a concentration-dependent manner, yielding *IC*$_{50}$ values of 0.18 ± 0.02 µM, 0.15 ± 0.02 µM, and 0.20 ± 0.02 µM, respectively. **g,** One-minute uptake of 370 nM [^{3}H]-CQ or 250 nM [^{3}H]-Arg was determined in the presence or absence of 1 µM Fab, 10 µM VP, CQ, PPQ, ADQ, or 1 mM Leu. Data are shown as mean±SEM (N,n=2,3) and values are normalized to the signal in the absence of non-radiolabeled compound. Data in panel a, c, d, and f are shown as mean±SEM (N,n=3,3) and are normalized to the specific signal (total cpm minus cpm in the presence of imidazole) in the absence of the respective non-radiolabeled compound.

References

1. Miller, L.H., Ackerman, H.C., Su, X.Z. & Wellems, T.E. Malaria biology and disease pathogenesis: insights for new treatments. *Nat Med* **19**, 156-167 (2013).
2. Fidock, D.A. et al. Mutations in the *P. falciparum* digestive vacuole transmembrane protein PfCRT and evidence for their role in chloroquine resistance. *Mol Cell* **6**, 861-871 (2000).
3. Martin, R.E. & Kirk, K. The malaria parasite's chloroquine resistance transporter is a member of the drug/metabolite transporter superfamily. *Mol Biol Evol* **21**, 1938-1949 (2004).
4. Organization, W.H. (Geneva: World Health Organization; 2018).
5. Fairhurst, R.M. et al. Artemisinin-resistant malaria: research challenges, opportunities, and public health implications. *Am J Trop Med Hyg* **87**, 231-241 (2012).
6. Blasco, B., Leroy, D. & Fidock, D.A. Antimalarial drug resistance: linking *Plasmodium falciparum* parasite biology to the clinic. *Nat Med* **23**, 917-928 (2017).
7. Ross, L.S. et al. Emerging Southeast Asian PfCRT mutations confer Plasmodium falciparum resistance to the first-line antimalarial piperaquine. *Nat Commun* **9**, 3314 (2018).
8. Naude, B., Brzostowski, J.A., Kimmel, A.R. & Wellems, T.E. *Dictyostelium discoideum* expresses a malaria chloroquine resistance mechanism upon transfection with mutant, but not wild-type, *Plasmodium falciparum* transporter PfCRT. *J Biol Chem* **280**, 25596-25603 (2005).
9. Lakshmanan, V. et al. A critical role for PfCRT K76T in *Plasmodium falciparum* verapamil-reversible chloroquine resistance. *EMBO J* **24**, 2294-2305 (2005).
10. Sanchez, C.P. et al. Differences in trans-stimulated chloroquine efflux kinetics are linked to PfCRT in *Plasmodium falciparum*. *Mol Microbiol* **64**, 407-420 (2007).
11. Paguio, M.F., Cabrera, M. & Roepe, P.D. Chloroquine transport in Plasmodium falciparum. 2. Analysis of PfCRT-mediated drug transport using proteoliposomes and a fluorescent chloroquine probe. *Biochemistry* **48**, 9482-9491 (2009).
12. Martin, R.E. et al. Chloroquine transport via the malaria parasite's chloroquine resistance transporter. *Science* **325**, 1680-1682 (2009).
13. Olafson, K.N., Ketchum, M.A., Rimer, J.D. & Vekilov, P.G. Mechanisms of hematin crystallization and inhibition by the antimalarial drug chloroquine. *Proc Natl Acad Sci USA* **112**, 4946-4951 (2015).
14. Dhingra, S.K. et al. A variant PfCRT isoform can contribute to *Plasmodium falciparum* resistance to the first-line partner drug piperaquine. *MBio* **8**, 303-317 (2017).
15. Renaud, J.P. et al. Cryo-EM in drug discovery: achievements, limitations and prospects. *Nat Rev Drug Discov* **17**, 471-492 (2018).
16. Dominik, P.K. et al. Conformational chaperones for structural studies of membrane proteins using antibody phage display with nanodiscs. *Structure* **24**, 300-309 (2016).
17. Parker, J.L. & Newstead, S. Structural basis of nucleotide sugar transport across the Golgi membrane. *Nature* **551**, 521-524 (2017).
18. Tsuchiya, H. et al. Structural basis for amino acid export by DMT superfamily transporter YddG. *Nature* **534**, 417-420 (2016).
19. Lee, Y. et al. Structure of the triose-phosphate/phosphate translocator reveals the basis of substrate specificity. *Nat Plants* **3**, 825-832 (2017).
20. Cremers, C.M. & Jakob, U. Oxidant sensing by reversible disulfide bond formation. *J Biol Chem* **288**, 26489-26496 (2013).
21. Gorka, A.P., de Dios, A. & Roepe, P.D. Quinoline drug-heme interactions and implications for antimalarial cytostatic versus cytocidal activities. *J Med Chem* **56**, 5231-5246 (2013).
22. Callaghan, P.S., Hassett, M.R. & Roepe, P.D. Functional comparison of 45 naturally occurring isoforms of the *Plasmodium falciparum* chloroquine resistance transporter (PfCRT). *Biochemistry* **54**, 5083-5094 (2015).
23. Pelleau, S. et al. Adaptive evolution of malaria parasites in French Guiana: Reversal of chloroquine resistance by acquisition of a mutation in *pfcrt*. *Proc Natl Acad Sci USA* **112**, 11672-11677 (2015).
24. Quick, M. & Javitch, J.A. Monitoring the function of membrane transport proteins in detergent-solubilized form. *Proc Natl Acad Sci USA* **104**, 3603-3608 (2007).
25. Zhang, H., Paguio, M. & Roepe, P.D. The antimalarial drug resistance protein Plasmodium falciparum chloroquine resistance transporter binds chloroquine. *Biochemistry* **43**, 8290-8296 (2004).

26. Lekostaj, J.K., Natarajan, J.K., Paguio, M.F., Wolf, C. & Roepe, P.D. Photoaffinity labeling of the *Plasmodium falciparum* chloroquine resistance transporter with a novel perfluorophenylazido chloroquine. *Biochemistry* **47**, 10394-10406 (2008).
27. Bellanca, S. et al. Multiple drugs compete for transport via the Plasmodium falciparum chloroquine resistance transporter at distinct but interdependent sites. *J Biol Chem* **289**, 36336-36351 (2014).
28. Sa, J.M. et al. Geographic patterns of Plasmodium falciparum drug resistance distinguished by differential responses to amodiaquine and chloroquine. *Proc Natl Acad Sci USA* **106**, 18883-18889 (2009).
29. Shi, L., Quick, M., Zhao, Y., Weinstein, H. & Javitch, J.A. The mechanism of a neurotransmitter:sodium symporter--inward release of Na+ and substrate is triggered by substrate in a second binding site. *Mol Cell* **30**, 667-677 (2008).
30. Kuhn, Y., Rohrbach, P. & Lanzer, M. Quantitative pH measurements in Plasmodium falciparum-infected erythrocytes using pHluorin. *Cell Microbiol* **9**, 1004-1013 (2007).
31. Bray, P.G. et al. Defining the role of PfCRT in *Plasmodium falciparum* chloroquine resistance. *Mol Microbiol* **56**, 323-333 (2005).
32. Lewis, I.A. et al. Metabolic QTL analysis links chloroquine resistance in *Plasmodium falciparum* to impaired hemoglobin catabolism. *PLoS Genet* **10**, e1004085 (2014).
33. Lee, A.H. et al. Evidence for Regulation of Hemoglobin Metabolism and Intracellular Ionic Flux by the Plasmodium falciparum Chloroquine Resistance Transporter. *Sci Rep* **8**, 13578 (2018).
34. Juge, N. et al. *Plasmodium falciparum* chloroquine resistance transporter is a H+-coupled polyspecific nutrient and drug exporter. *Proc Natl Acad Sci USA* **112**, 3356-3361 (2015).

Acknowledgments We thank Bill Rice, Ed Eng, Laura Kim, Kelsey Jordan, Misha Kopylov, Venkat Dandey, Hui Wei, Sargis Dallakyan, Carl Negro, Stanislaw Gabryszewski, Somnath Mukherjee, Bryce Riegel, Oliver Clarke and Yunting Chen for their helpful contributions. This work was supported by NIH grants (R01 GM111980 and R21 AI119672 to F.M.; R37 AI50234 and R01 AI124678 to D.A.F.; R01 GM119396 to M.Q.; R01 AI506312 and AI111962 to P.D.R.; T32 HL120826 to J.K.; P41 GM103310 to C.S.P. and B.C.; the Agency for Science, Technology and Research Singapore (to Y.Z.T.); the Simons Foundation (SF349247 to C.S.P. and B.C.); and NYSTAR (to C.S.P. and B.C.). Some of the work was performed at the Center for Membrane Protein Production and Analysis (COMPPÅ; P41 GM116799 to Wayne Hendrickson) and at the National Resource for Automated Molecular Microscopy at the Simons Electron Microscopy Center (P41 GM103310), both located at the New York Structural Biology Center.

Author contributions J.K. and D.A.F. performed bioinformatics analyses. J.K. performed protein expression and purification, with help from S.I.G. S.K.E., K.N., and A.A.K. identified the Fabs. Y.Z.T. and J.K. produced and analyzed the cryo-EM data, and built the model, with help from B.C. and C.S.P. M.Q. and A.L.W. performed the functional assays. K.J.W., S.K.D., J.O., P.D.R. and D.A.F. conducted mutational analyses. M.Q., D.A.F. and F.M. designed experiments and wrote the paper with J.K., Y.Z.T., K.J.W., and P.D.R.

Competing interests The authors declare no competing interest.

Correspondence and requests for materials should be addressed to M.Q., D.A.F., or F.M.

Data availability: All raw movie frames, micrographs, the particle stack and relevant metadata files will be deposited into EMPIAR. The electron density map will be deposited into EMDB. The model will be deposited into PDB. All data are available in the manuscript or the supplementary materials.

Methods

Small-scale expression screen of CRT variants. Initial expression studies were performed with twelve CRT variants, including the *Plasmodium falciparum pfcrt* sequences 7G8 (AF233064), HB3 (Q9N623), HB3 that was codon optimized for *Xenopus laevis*, Dd2 (D5L5S2), Dd2 codon optimized for *Xenopus laevis*, *Plasmodium berghei* CRT (PbCRT, Q9GSD8), *Plasmodium knowlesi* CRT (PkCRT, Q9GSD7), *Plasmodium vivax* CRT (PvCRT, Q9GSD3), PvCRT codon optimized for *Spodoptera frugiperda*, *Theileria parva* CRT (TpCRT, Q4N5R6), *Theileria annulata* CRT (TaCRT, Q4UDS9), and *Cryptosporidium parvum* CRT (CpCRT, Q7YZ23). To express these in mammalian cells, the sequences were cloned into pFM1.2[35] as a GFP fusion with a decahistidine affinity tag at either the 5' or 3' end of the gene. One μg of each construct was diluted into 100 μl opti-MEM (ThermoFisher Scientific) and mixed with 100 μl opti-MEM containing 4 μg of polyethylenimine (PEI) Max MW 40,000 (Polysciences). This mixture was added to 1.0×10^6 HEK293T cells (Invitrogen) cells in a total volume of 2 mL, in a 6-well plate (Corning). The cell transfection mixture was incubated at 37°C for 72 hr in 5% CO_2. Transfected cells were then harvested, centrifuged at 800×*g* for 10 minutes at 4°C, and washed once on ice in 1×PBS. Each pellet was resuspended and solubilized in 20 mM HEPES pH 7.5, 200 mM NaCl, 20 mM $MgSO_4$, 0.5 mM phenylmethylsulfonyl fluoride (PMSF), cOmplete™, EDTA-free Protease Inhibitor Cocktail (Roche), 10 μg/mL DNaseI (Roche) and 8 μg/mL RNase (Sigma-Aldrich) supplemented with 1% n-dodecyl-β-D-maltopyranoside (DDM) and 0.1% cholesteryl hemisuccinate (CHS) at 4°C for 2 hr. Insoluble material was removed by ultracentrifugation in a single angle rotor at 4°C for 45 min. The supernatant of each sample was subjected to western blot analysis using a rabbit anti-GFP antibody (diluted 1:5,000; Invitrogen) and a secondary goat anti-rabbit IgG conjugated to horseradish peroxidase (diluted 1:7,000; Invitrogen). Labeling was detected using a western blot Luminol reagent (Santa Cruz).

Expression and stability were further evaluated by fluorescence-coupled size exclusion chromatography (FSEC)[36]. In these assays, each GFP-tagged construct was transfected into HEK293 Freestyle cells (Invitrogen) in the presence of PEI. Transfected cells were incubated at 37°C for 72 hr with 8% CO_2 and 70% humidity. Cell supernatants for the FSEC analysis were prepared as described above. DDM-solubilized supernatants were loaded onto a TSKgel G4000SWxl column (Tosoh Bioscience LLC) attached to a Prominence UFLC (Shimadzu) coupled to a RF-10AXL fluorescence detector (Shimadzu). These studies identified the PfCRT 7G8 construct as having the best yield and mono-dispersity.

PfCRT 7G8 protein expression, purification and nanodisc reconstitution. The *pfcrt* 7G8 full-length open reading frame was cloned into the pEG BacMam vector[37] using the Gibson Assembly method[38]. *pfcrt* was fused at its 3' end with a Tobacco Etch Virus (TEV) protease cleave site (ENLYFQSYV) and a decahistidine affinity tag followed by a streptavidin affinity tag (WSHPQFEK). The resulting plasmid was transformed into DH10Bac *E. coli* competent cells to generate the bacmid using bac-to-bac (Invitrogen) protocol. Recombinant P1 baculovirus was transfected into Sf9 cells (Expression System) in the presence of PEI and cultured in ESF 921 Protein-free insect cell culture medium (Expression Systems). For protein expression, 100 mL P4 virus was used to infect 1L cultures of HEK293S GnTi$^-$ cells (Invitrogen) at 3×10^6 cells/mL in Freestyle 293 media (GIBCO) supplemented with 2% FBS (GIBCO). After infection, the cells were incubated at 37°C for 8 to 10 hr in the presence of 8% CO_2 and 70%

humidity. We then added 10 mM sodium butyrate (Sigma-Aldrich) to enhance BacMam protein expression. Cells were incubated at 37°C for another 48 hr prior to their harvest. Cell pellets were homogenized in low salt buffer 10 mM HEPES pH 7.5, 10 mM KCl, 10 mM $MgCl_2$, 0.5 mM PMSF, cOmplete™, EDTA-free Protease Inhibitor Cocktail, 10 μg/mL DNaseI and 8 μg/mL RNase in a glass homogenizer. Membrane fractions were isolated by ultracentrifugation at 40,000×*g* in Type 45 Ti Rotor (Beckman Coulter). Membrane fractions were further homogenized and washed twice with high salt buffer containing 10 mM HEPES pH 7.5, 10 mM KCl, 10 mM $MgCl_2$, 1 M NaCl, 0.5 mM PMSF, cOmplete™, EDTA-free Protease Inhibitor Cocktail, 10 μg/mL DNaseI and 8 μg/mL RNase in a glass homogenizer followed by ultracentrifugation. The washed membrane fractions were resuspended again by homogenizing in buffer containing 20 mM HEPES pH 7.5, 200 mM NaCl and 0.5 mM PMSF, and cOmplete™, EDTA-free Protease Inhibitor Cocktail, and then stored at -80°C until use.

The thawed membrane fraction was solubilized by adding DDM with CHS in a 10:1 (w/w) ratio to a final concentration of 1% (w/v) detergent and incubating at 4°C for 2 hours with gentle agitation. Insoluble material was removed by ultracentrifugation at 40,000×g in a type 45 Ti rotor (Beckman Coulter) at 4°C for 30 min. The supernatant was filtered (Millipore) into a Falcon tube containing pre-equilibrated Ni^{2+}-NTA resin (Qiagen) in the presence of 20 mM imidazole and incubated 4°C overnight with gentle rotation. The resin was washed with 10 column volumes of buffer containing 20mM HEPES pH 7.5, 200 mM NaCl, 60mM imidazole, 0.1% DDM and 0.01% CHS and eluted with buffer consist of 20 mM HEPES pH 7.5, 200 mM NaCl, 200 mM imidazole, 0.05% DDM and 0.005% CHS. The eluted protein was incorporated into lipid nanodiscs with a molar ratio 1:600:10 of protein:1-palmitoyl-2-oleoyl-sn-glycero-3-phospho-(1'-rac-glycerol) (POPG): membrane scaffold protein 1D1 (MSP1D1) and incubated at 4°C for 2.5 hr with gentle agitation. Reconstitution was initiated by removing detergent with the addition of Bio-beads (Bio-Rad) at 4°C overnight with constant rotation. Bio-beads were removed and the nanodisc reconstitution mixture was bound again to Ni^{2+}-NTA resin for at 4°C for 2 hr to remove free nanodiscs. The resin was washed with 10 column volumes of wash buffer (20 mM HEPES pH 7.5, 200 mM NaCl and 20 mM Imidazole) followed by 4 column volumes of elution buffer (20 mM HEPES pH 7.5, 200 mM NaCl and 200 mM Imidazole). The eluted protein was further purified by loading on a Superdex 200 Increase 10/300 GL size-exclusion column (GE Healthcare Life Sciences) in gel filtration buffer (20 mM HEPES pH 7.0 and 150 mM NaCl).

Identification of PfCRT-specific Fab fragments using phage display. For the purposes of Fab screening, PfCRT 7G8 was reconstituted into nanodiscs using biotinylated MSP1D1. Prior to nanodisc assembly, MSP1D1 was chemically biotinylated as previously described[16, 39, 40]. Efficient biotinylation was confirmed using a pull-down assay with streptavidin-coated paramagnetic particles (Promega). Biopanning was performed using Fab Library E[41, 42] in Selection Buffer (25 mM HEPES pH 7.4, 150 mM NaCl, and 1% Bovine Serum Albumin). In the first round, biopanning was performed manually using 200 nM of PfCRT 7G8-MSP1D1 nanodiscs immobilized onto magnetic beads. Following three washes with Selection Buffer, the resuspended beads enriched for PfCRT-specific Fab fragments were used to infect log-phase *E. coli* XL-1 Blue cells. Phages were amplified overnight in 2xYT media supplemented with ampicillin (100 μg/mL) and M13-KO7 helper phage (10^9 pfu/mL). To increase the stringency of selection, four additional rounds of sorting were performed with decreasing target concentration,

from 150 nM to 75 nM to 40 nM to 20 nM. For each round, the amplified phage pool from each preceding round was used as the input. For rounds 2-5, biopanning was performed semi-automatically using a Kingfisher magnetic beads handler (Thermo Fisher Scientific). To reduce the presence of non-specific binders, the phage pool for rounds 2-5 was pre-cleared with 100 µL of streptavidin particles. Moreover, for all rounds empty, non-biotinylated 1D1 nanodiscs were used as soluble competitors in excess at a constant concentration of 1.5 µM. Finally, in rounds 2-5, bound phage particles were removed by elution from magnetic beads following a 15 min incubation step with 1% Fos-choline-12 prepared in Selection Buffer.

Single-point phage ELISA. The initial validation for selection was performed by single-point phage ELISA using individual clones from rounds 4 and 5. All ELISA experiments were performed in 96-well plates (Nunc) coated with 2 µg/mL Neutravidin and blocked with Selection Buffer. Colonies of *E. coli* XL-1 blue harboring phagemids were used to inoculated 400 µL 2xYT media supplemented with 100 µg/mL ampicillin and 10^9 pfu/mL M13-KO7 helper phage. Phages were amplified overnight in 96-well deep-well blocks at 37°C with shaking at 280 rpm. Amplified phages were diluted 10-fold into Selection Buffer and assayed against either PfCRT-loaded or empty biotinylated nanodiscs. Target proteins were immobilized at room temperature for 30 min followed by incubation with phage dilutions for 30 min. Bound phage particles were detected with TMB substrate (Thermo Fisher Scientific) following a 30 min incubation with HRP-conjugated anti-M13 monoclonal antibody (GE Healthcare). The reaction was quenched with 1.0 M HCl and the absorbance at 450 nm was measured. Wells containing empty nanodiscs were used to determine non-specific binding.

Fab expression and purification. Specific binders from phage ELISA were selected based on their signal/background ratio[16] and were sequenced at the University of Chicago Comprehensive Cancer Center DNA Sequencing facility. Unique clones were then sub-cloned in pRH2.2 using the In-Fusion Cloning kit (TaKaRa Bio). Sequence-verified Fab expression vectors were then transformed into *E. coli* BL21-Gold competent cells (Agilent) and used to inoculate overnight cultures. Inocula were used the following morning to seed 1L 2xYT broth supplemented with 100 µg/mL ampicillin, which were subsequently grown to an OD_{600} of 0.8 and then induced for 4 hours. Cells were harvested by centrifugation and stored at -80°C until use. Cell pellets were resuspended in buffer (20 mM HEPES pH 7.4, 150 mM NaCl and 0.5 mM $MgCl_2$) supplemented with 1 mM PMSF and 1 µg/mL DNase I (Gold Biosciences). These preparations were sonicated (Branson Sonifier) until complete lysis was achieved. Lysates were then incubated at 60°C for 30 min to eliminate potential Fab proteolyzed fragments, subsequently cooled on ice, and cleared by centrifugation. Supernatants were filtered and then loaded onto a 5-mL HiTrap MabSelect SuRe column (GE Healthcare) equilibrated with Wash Buffer (20 mM HEPES pH 7.4 and 500 mM NaCl). The column was washed 10 times with Wash Buffer and Fabs were eluted with 0.1 M acetic acid. Fractions containing Fab fragments were loaded onto a 1 mL Resource S column (GE Healthcare) equilibrated with buffer A (50 mM sodium acetate, pH 5.0). Following washing with 10 column volumes of buffer A, Fab fragments were eluted by a linear 0-50% gradient with buffer B (buffer A with 2 M NaCl). Fractions containing Fab fragments were evaluated for purity by SDS-PAGE and subsequently pooled and dialyzed overnight in 20 mM HEPES pH 7.4 and 150 mM NaCl.

Multi-point protein ELISA. To estimate apparent binding affinity, we performed multi-point ELISA with purified Fab fragments[16]. Purified Fab fragments were diluted serially 3-fold starting from 3 μM maximum concentration. ELISA plates were coated and blocked as described above for the phage ELISA studies. 50 nM of biotinylated PfCRT 7G8-MSP1D1 nanodiscs were immobilized on the plates by 30 min incubation, followed by washing. Fab dilutions were added to wells containing immobilized PfCRT and allowed to bind for 30 min. Bound Fab was detected with TMB substrate following a 30 min incubation with HRP-conjugated mouse anti-human IgG $F(ab')_2$ monoclonal antibody (Jackson). Reactions were quenched with 1.0 M HCl and the absorbance at 450 nm was measured. A_{450} values were plotted against the $\log_{10}$ of the Fab concentration. EC_{50} values were then calculated in Prism (GraphPad Software) using a variable slope model and assuming a sigmoidal dose response.

PfCRT 7G8 in nanodisc complexed with Fab CTC. Size-exclusion chromatography fractions of purified PfCRT in nanodisc were incubated with the CTC Fab on ice for 2 hr in a 1:3 molar ratio of protein to Fab. The PfCRT-Fab complex was then concentrated and filtered, and then loaded on a Superdex 200 Increase 10/300 GL size-exclusion column in gel filtration buffer (20mM HEPES pH 7.0 and 150mM NaCl).

Negative stain electron microscopy. In order to determine the quality of the sample and success of the Fab binding, purified protein was diluted to 0.01 mg/ml (for PfCRT without Fab) or 0.005 mg/ml (for PfCRT with Fab) and applied onto copper grids (Ted Pella). These grids were overlaid by a thin (~1.5 nm) layer of continuous carbon that had been plasma-cleaned (Gatan Solarus) for 30s using a mixture of H_2 and O_2. Thereafter, filter paper (Whatman 4) was used to remove the protein solution. 3 μl of 2% uranyl formate was then added and immediately removed by absorbing with filter paper – this repeated seven times. The grid was imaged on either a Tecnai T12 microscope (FEI) (for PfCRT without Fab) or a Tecnai TF20 microscope (FEI) (for PfCRT with Fab). Both microscopes were equipped with a Tietz F416 CCD camera (Tietz) at 1.23 Å or 1.10 Å per pixel respectively, using the Leginon software package[43]. 166 and 87 images were collected respectively and were processed using the Appion software package[44] to obtain 2D classes with Relion 2.1[45, 46]. The micrographs showed good particle dispersion (**Extended Data Fig. 3**). 2D class averages showed that the Fab addition resulted in a clear fiducial for particle alignment.

Single-particle cryo-EM vitrification and data collection. Purified PfCRT-Fab complex was concentrated to 1.56 mg/ml using a 30-kDa concentrator (Amicon). 2.5 μL of sample was added to a plasma-cleaned (Gatan Solarus) 1.2/1.3 μm holey gold grid (Quantifoil UltrAuFoil) and blotted using filter paper on one side for 2s using the Leica GP plunger system before plunging immediately into liquid ethane for vitrification. The plunger was operating at 6°C with >80% humidity to minimize evaporation and sample degradation.

Data acquisition. Images were recorded on a Titan Krios electron microscope (FEI) equipped with a C_s corrector and K2 summit direct detector (Gatan) operating at 0.5175 Å per pixel (calibrated using an AAV2 dataset) in counting mode using the Leginon software package[43]. Energy filter slit width of 15 eV was used during the collection and was aligned automatically every hour using Leginon. Data collection was performed using a dose of ~91.56 $e^-/Å^2$ across 80 frames (75 msec per frame) at a dose rate of ~4.0 e^-/pix/sec, using a set defocus range of -1.2 μm

to -1.8 μm. A 100 μm objective aperture was used. In total, 3,377 micrographs were recorded over a single 2.5-day collection using an image beam shift data collection strategy[47]. Ice thickness was monitored after every 4th exposure using the Leginon zero-loss peak (ZLP) algorithm[48] and was determined to be 23.1 ± 9.1 nm (SD)

Data processing. Movie frames were aligned using MotionCor2[49] with 3 by 3 patches, a grouping of 3, and a B-factor of 100, using the Appion software package[44]. Micrograph CTF estimations were performed using both CTFFind4[50] and GCTF[51], and the best estimates based on confidence were selected using the Appion software package. Micrographs that had estimated resolution at 0.5 confidence level of worse than 10 Å were removed, resulting in 3,297 micrographs. DoG picker[52] was used to pick 682,520 particles (extracted binned by 2), which were transferred into Relion 2.1[45, 46] for 2D classification. 2D class averages that showed clear structural details of PfCRT were used as templates for template-based picking using Gautomatch (https://www.mrc-lmb.cam.ac.uk/kzhang/Gautomatch; Kai Zhang, unpublished). To not miss any particles, we chose a lenient threshold that resulted in 1,095,304 initial picks. These were pared down to 183,241 particles after Relion 2D classification. Two rounds of CryoSPARC 2 [53] *ab initio* (using 2 models) were then performed to further refine the particle stack to 35,682 particles, which yielded an 8.27 Å resolution upon 3D homogeneous refinement. Particles were then re-centred and re-extracted using Relion and per-particle CTF estimation using GCTF was then performed. The particle stack was brought back into CryoSPARC for one round of *ab initio* refinement (using 2 models). The best set of particles and model was then used for non-uniform refinement. This resulted in a 3.7 Å map from 17,034 particles.

The mag_distortion_correct software[54] was then used on the micrographs to correct for magnification anisotropy of 1.3%, which was determined previously using gold-replica grating using the mag_distortion_estimate software[54]. The resulting particles were then subjected to three rounds of CryoSPARC non-uniform refinement, re-centering and re-extracting in Relion, with removal of overlapped particles centered no more than 20 pixels from each other, and CTF refinement using *cis*TEM[55]. This resulted in 3.6 Å from 17,030 particles.

In an effort to optimize the alignment of frames, movie frames were re-aligned using MotionCor2 with 2 by 2 patches, a grouping of 3, correction for in-frame motion, and a B-factor of 150 for global frame alignment and 50 for local frame alignment. Visual inspection of the resulting micrographs showed that certain micrographs fared better using the new frame alignment parameters (these were less blurry), while some fared worse than with the 3 by 3 patches described above. To determine the best frame alignment parameter on a per-particle basis, particles were extracted from micrographs using both conditions. These particles were then subjected to a CryoSPARC 2 non-uniform refinement and one round of *cis*TEM refinement. Thereafter, for each particle, we chose the alignment parameter that produced the highest score. This resulted in 7,191 particles coming from micrographs aligned with 2 by 2 patches, and 9,714 particles coming from micrographs aligned with 3 by 3 patches. Particle polishing algorithms that require neighboring particles to aid in alignment were tested but gave consistently worse results, likely because of the low average number of particles per micrograph (~5.3) caused by the high magnification used and sizeable number of free Fab contaminants.

Thereafter, signal subtraction using Relion was performed. Subtraction of just the nanodisc did not improve the overall resolution. However, subtraction of both the nanodisc and constant

domain of the Fab improved the resolution of the reconstruction, after CryoSPARC non-uniform refinement, to 3.3 Å overall, and 3.2 Å for PfCRT alone.

This final map was sharpened using phenix.auto_sharpen[56], which automatically selected b_iso sharpening to high_resolution cutoff as the algorithm to use. Overall b_sharpen applied was 28.3 $Å^2$, final b_iso obtained was 47.3 $Å^2$ and the high-resolution cut-off was 3.2 Å.

All conversions between Relion, CryoSPARC, and *cis*TEM were performed using Daniel Asarnow's pyem script (unpublished, https://github.com/asarnow/pyem).

Model building and refinement. To build the PfCRT model, we first used the Chimera[57] program to approximately segment out the PfCRT part of the map from the nanodisc and Fab density. *De novo* model building for the PfCRT cryo-EM map its primary sequence was initiated using Rosetta[58]. After two rounds of Rosetta model building, the partial model was brought into Coot[59] program for manual model building. For model building of the Fab, the Fab portion of the deposited yeast nucleoprotein complex (PDB-ID:4XMM[60]) was used as a starting template as it had the same scaffold backbone. An extra electron density between PfCRT helices 1, 9 and 10 was not modelled by protein density and was likely of lipid origin. Out of the lipids potentially present in the nanodisc, CHS produced the best density fit and was therefore incorporated into the model.

Thereafter, model adjustment and refinement were performed iteratively in Coot and Phenix, with the statistics being examined using Molprobity[61] until no further improvements were observed. The final map and model were then validated using 1) EMRinger[62] to compare map to model, 2) ResMap[63] to calculate map local resolution, and 3) a program suite with 3D Fourier shell correlations (FSC; [64]). To calculate the FSC values, we used a cut-off criterion of 0.143[65]. The 3D FSC program suite[64] was used to calculate the degree of directional resolution anisotropy. Map-to-model FSCs were also calculated by first converting the model to a map using Chimera molmap function at Nyquist resolution (2.07 Å). A mask was made from this map using Relion (after low-pass filtering to 8 Å, extending by 1 pixel and applying a cosine-edge of 3 pixels), and was then applied to the density map. Map-to-model FSC was calculated using EMAN[66].

Model analysis. A cavity search using the Solvent Extractor from Voss Volume Voxelator server[67] was performed using an outer probe radius of 10 Å and inner probe radius of 3 Å. We then used a Dali server[68] to search for other PDB structures with a similar fold. This search produced top results for Vrg4 (PDB ID: 5OGE/5OGK;[17]), YddG (PDB ID: 5I20;[18]) and TPT (PDB ID: 5Y78/5Y79;[19]), with Z scores from 26.7 to 16.0. Thereafter, there was a large drop in Z score for the next best hit at 8.5 (the chloride pumping rhodopsin, PDB ID: 5B2N) that visually did not superimpose well with PfCRT (Root mean square deviation of superimposition was 8.1 Å).

Amino acid sequence alignments. For conservation analysis in Apicomplexan parasites, we obtained nine orthologs of CRT from OrthoMCL-DB[69]. Their amino acid sequences were then aligned using MUSCLE[70].

For the pairwise alignments shown in **Extended Data Fig. 6**, the PfCRT 7G8 sequence was trimmed of residues 1-50 (N-terminus and JM1), 181-202 (TM5), 262-303 (JM2) and 368-424 (TM10 and C-terminus) and put through the AlignMe[71-73] server.

For the sequences used for **Extended Data Fig. S8**, the sequences used are Pf3D7_0709000, PVX_087980, PKNH_0107600, PY05061, PBANKA_1219500, PCHAS_1220200, Chro.60564, cgd6_4890, and TA12005. Multiple sequence alignments were displayed using ESPript[74].

Scintillation proximity assay (SPA)-based binding. All radiolabeled compounds were purchased from American Radiolabeled Chemicals. Unless other concentrations are indicated, binding of 125 nM [^{3}H]-Arg (40 Ci/mmol), 370 nM [^{3}H]-CQ (5.45 Ci/mmol), or 75 nM [^{3}H]-PPQ (15 Ci/mmol) (unless was performed with the SPA, as described previously[24]. 100 ng of PfCRT 7G8 reconstituted into nanodiscs were assayed in buffer composed of 50 mM Tris/Mes, pH 7.5, 5 % glycerol, 0.1 mM TCEP, 0.1 % PEI in the presence of 125 µg of YSi-His Tag SPA beads (Perkin Elmer), and in the presence or absence of indicated reagents or Fab. 800 mM imidazole, which competes with the His tag (fused to PfCRT) for binding to the copper-coated YSi SPA beads, was used to determine the non-proximity background signal. Concentrations of radiolabeled compounds were chosen in pilot experiments to obtain a signal-to-noise ratio ≥ 5, and specific binding was determined by subtracting the cpm in the presence of imidazole from the cpm measured in its absence. Control binding experiments of [^{3}H]-CQ employed nanodiscs containing 100 ng of the unrelated *Aquifex aeolicus* bacterial amino acid transporter LeuT. Non-linear regression analysis of the data was performed with GraphPad Prism 7. Kinetic constants represent the means ± SEM of the fit.

Transport measurements. Purified PfCRT 7G8 was reconstituted in preformed liposomes made of *E. coli* total lipids:CHS 94:6 (w/w) at a protein-to-lipid ratio of 1:150 (w/w). The lumen of the proteoliposomes was composed of 100 mM KP_i, pH 7.5 and 2 mM β-mercaptoethanol. Uptake of [^{3}H]-Arg (40 Ci/mmol), [^{3}H]-CQ (5.45 Ci/mmol), or [^{3}H]-PPQ (15 Ci/mmol) was performed by diluting PfCRT-containing proteoliposomes (40 ng PfCRT per assay) in 50 µL of 100 mM Tris/Mes, pH 5.5. When indicated, 1 µM valinomycin (Val) was added to the reaction to generate a K^+ diffusion potential-driven membrane potential. The reactions were stopped after the indicated time periods by the addition of ice-cold 100 mM KP_i, pH 6.0/100 mM LiCl and filtered through 0.45 µm nitrocellulose filters (Millipore). Filters were dried and incubated in scintillation cocktail, and the radioactivity captured on the filters was counted in a Hidex SL300 scintillation counter. Specific radioactivity of all compounds was confirmed by counting known amounts of each radiolabel by determination of the decays-per-minutes (dpm) to transform the dpm of the samples into pmol. Unspecific binding of all compounds with the nitrocellulose filters was determined by measuring mock uptakes in the absence of liposomes or proteoliposomes, and these values (determined for each experiment) were used to calculate the uptake activity in liposomes or proteoliposomes. For data shown in Extended Data Fig. 13, the specific uptake was determined by subtracting the time-dependent accumulation of the tested compounds in control liposomes (lacking PfCRT) from that measured in PfCRT-containing proteoliposomes.

Extended Data Fig. 1

a

Haplotype	Region	Mutations	PfCRT haplotype														Drug phenotype	
			72	74	75	76	97	145	220	271	326	343	350	353	356	371	CQ	PPQ
3D7 (wild-type)	Africa	0	C	M	N	K	H	F	A	Q	N	M	C	G	I	R	S	S
7G8	S. America, W. Pacific	5	S	--	--	T	--	--	S	--	D	--	--	--	L	--	R	S
7G8+C350R	French Guiana (S. America)	6	S	--	--	T	--	--	S	--	D	--	R	--	L	--	S	R (low)
Dd2	SE Asia	8	--	I	E	T	--	--	S	E	S	--	--	--	T	I	R	S
Dd2+H97Y	Cambodia	9	--	I	E	T	Y	--	S	E	S	--	--	--	T	I	R	R
Dd2+F145I	Cambodia	9	--	I	E	T	--	I	S	E	S	--	--	--	T	I	S[a]	R
Dd2+M343L	Cambodia	9	--	I	E	T	--	--	S	E	S	L	--	--	T	I	S[a]	R (low)
Dd2+G353V	Cambodia	9	--	I	E	T	--	--	S	E	S	--	--	V	T	I	S[a]	R

Mutations in the reference Dd2 allele are shown in light grey. Other mutations are in dark grey. S, sensitive; R, resistant; [a]Sensitized to CQ compared to parental line but not fully sensitive.

b

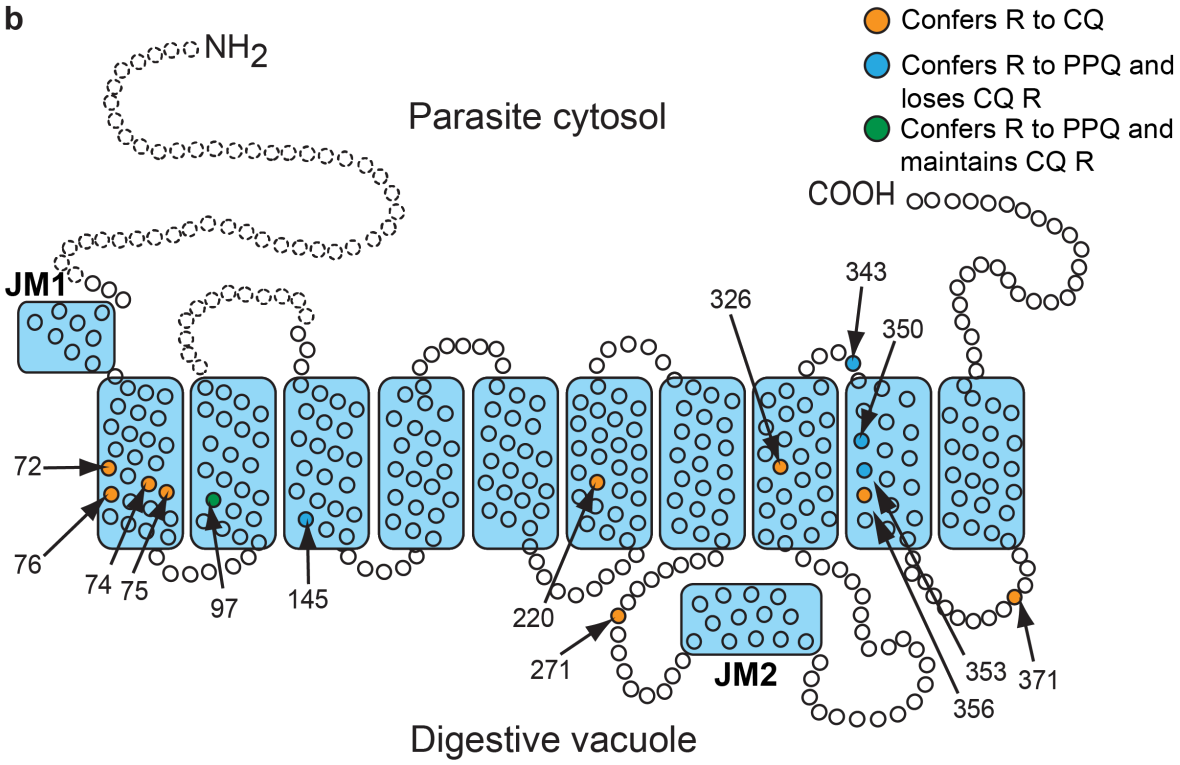

Extended Data Figure 1 | Major PfCRT haplotypes and location of residues involved in chloroquine (CQ) or piperaquine (PPQ) drug resistance phenotypes. a, Listing of the PfCRT canonical CQ-sensitive 3D7 haplotype, the 7G8 (South America and Western Pacific) and Dd2 (Southeast Asia) variant haplotypes, and mutations that have emerged in *P. falciparum* parasites in malaria-endemic areas that contribute to PPQ resistance. **b,** Localization of PfCRT mutations associated with CQ or PPQ resistance, based on the solved PfCRT structure. Most mutations localize within or near the boundary of one of the 10 transmembrane helices. JM, juxtamembrane. **Extended Data Table 2** shows an expanded list of mutations observed in the field or obtained in drug-pressured cultured parasites.

Extended Data Fig. 2

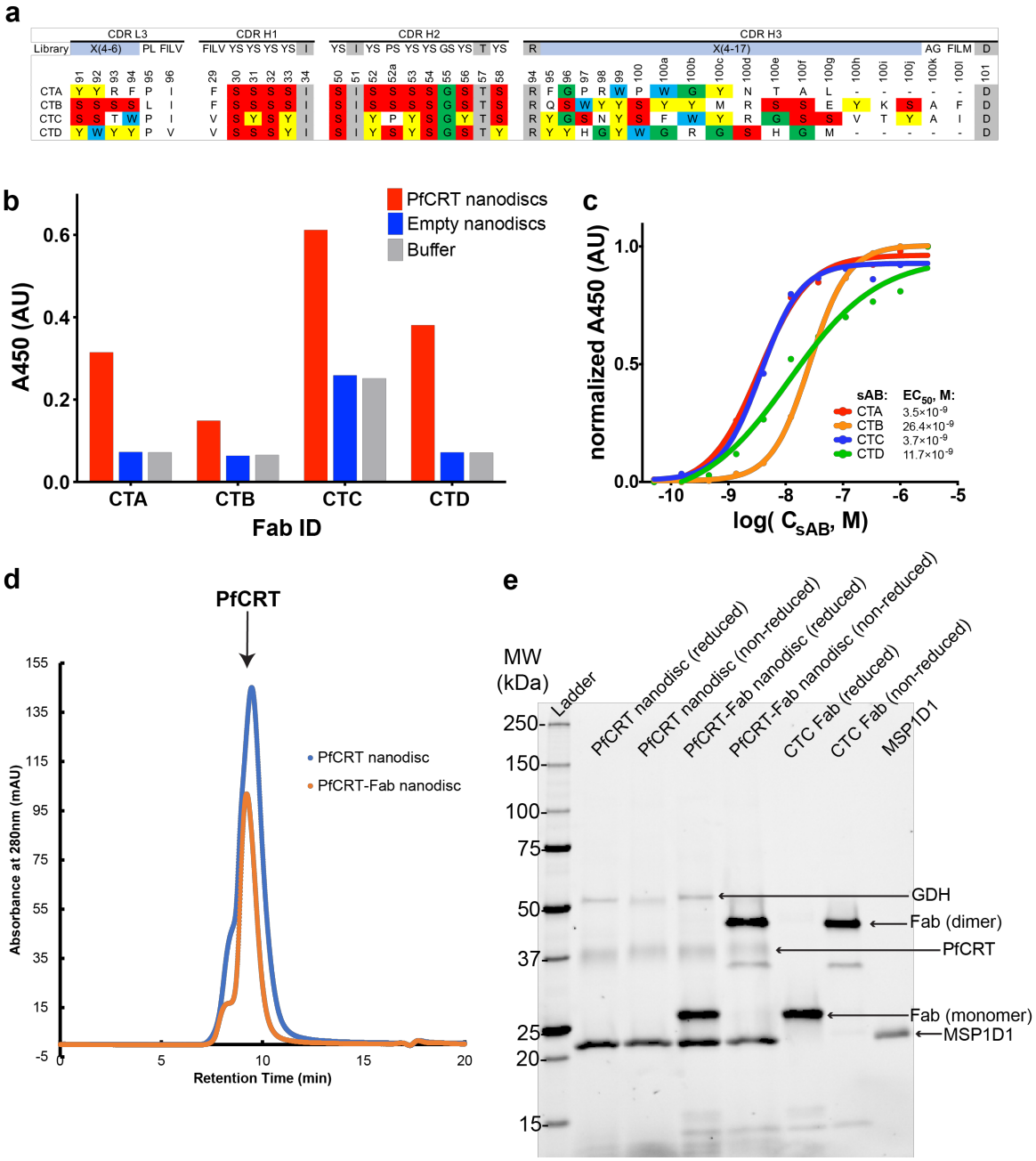

Extended Data Figure 2 | Identification of PfCRT-specific antigen-binding fragments (Fab) and preparation of purified PfCRT±Fab protein in nanodiscs. a, Complementarity-determining region (CDR) sequences of unique antigen-binding fragments (Fabs) panned for binding to recombinant PfCRT incorporated into MSP1D1 nanodiscs. Fabs were selected following multiple rounds of enrichment from the phage display library E[41, 42, 75]. Enriched SYGW residues are highlighted by color code (red, yellow, green and blue, respectively) and are numbered according to the Kabat system[76]. **b,** Single-point ELISA quantifying the binding of phage-displayed Fab to PfCRT-incorporated nanodiscs, empty nanodiscs, or buffer (empty wells), as measured at 450 nm absorbance. **c,** *EC50* evaluation for purified Fab binding to PfCRT

incorporated into biotinylated nanodiscs, showing high affinity binding for the CTC Fab (3.7 nM). **d,** High-performance liquid chromatography profile of PfCRT ± bound CTC Fab. **e,** SDS-PAGE gel of pooled and concentrated size-exclusion chromatography fractions from PfCRT±CTC Fab. The contaminant glutamate dehydrogenase, GDH (present as a left shoulder in **d**), was excluded from single-particle analyses. MSP1D1 is a membrane scaffold protein used to assemble the nanodiscs. The identity of PfCRT and GDH was confirmed using mass spectrometry.

Extended Data Fig. 3

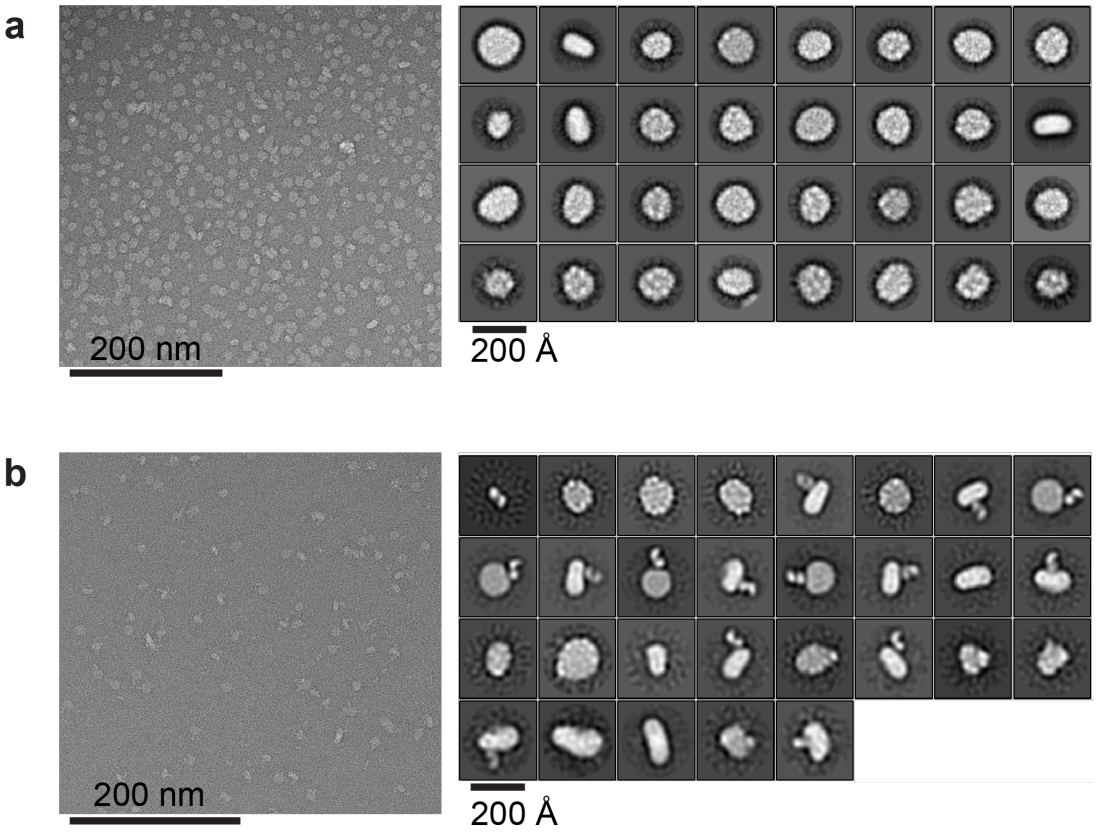

Extended Data Figure 3 | Negative-stain electron microscopy of PfCRT with and without Fab. a, Representative micrograph and 2D class averages from Relion[45] 2D classification of nanodisc-incorporated PfCRT without Fab. **b,** Representative micrograph and 2D class averages from Relion 2D classification of nanodisc-incorporated PfCRT with bound CTC Fab.

Extended Data Fig. 4

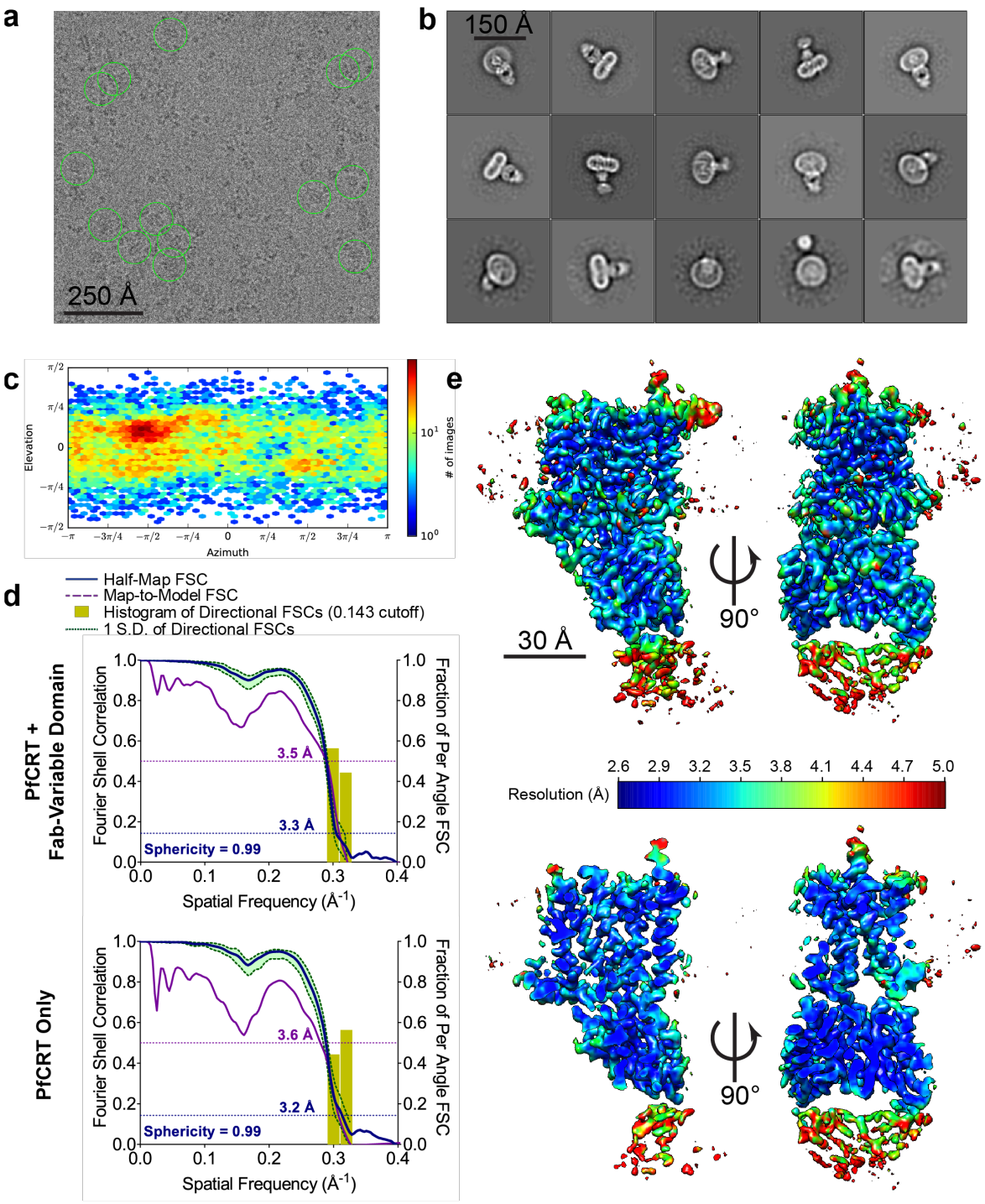

Extended Data Figure 4 | Cryo-EM analysis of the PfCRT-Fab complex. a, Representative micrograph (0.5175 Å per pixel, 1.65 μm defocus). Picked particles contributing to the final reconstruction are circled in green. **b,** Representative 2D class averages from Relion 2D classification. **c,** Euler angle distribution plot of the final 3D reconstruction from CryoSPARC 2[53]. **d,** Fourier shell correlation (FSC) curves for PfCRT complexed with the Fab variable domain as well as for PfCRT alone. Data show the half-map (blue) and map-to-model (purple)

resolutions (at 0.143 and 0.5 cut-offs respectively), with embedded histograms of directional resolutions sampled evenly over the 3D-FSC[64] (yellow). The corresponding sphericity values are indicated. **e,** Local resolution[77] display of unsharpened reconstructions of PfCRT complexed with the Fab variable domain, in orthogonal views, sliced through the density.

Extended Data Fig. 5

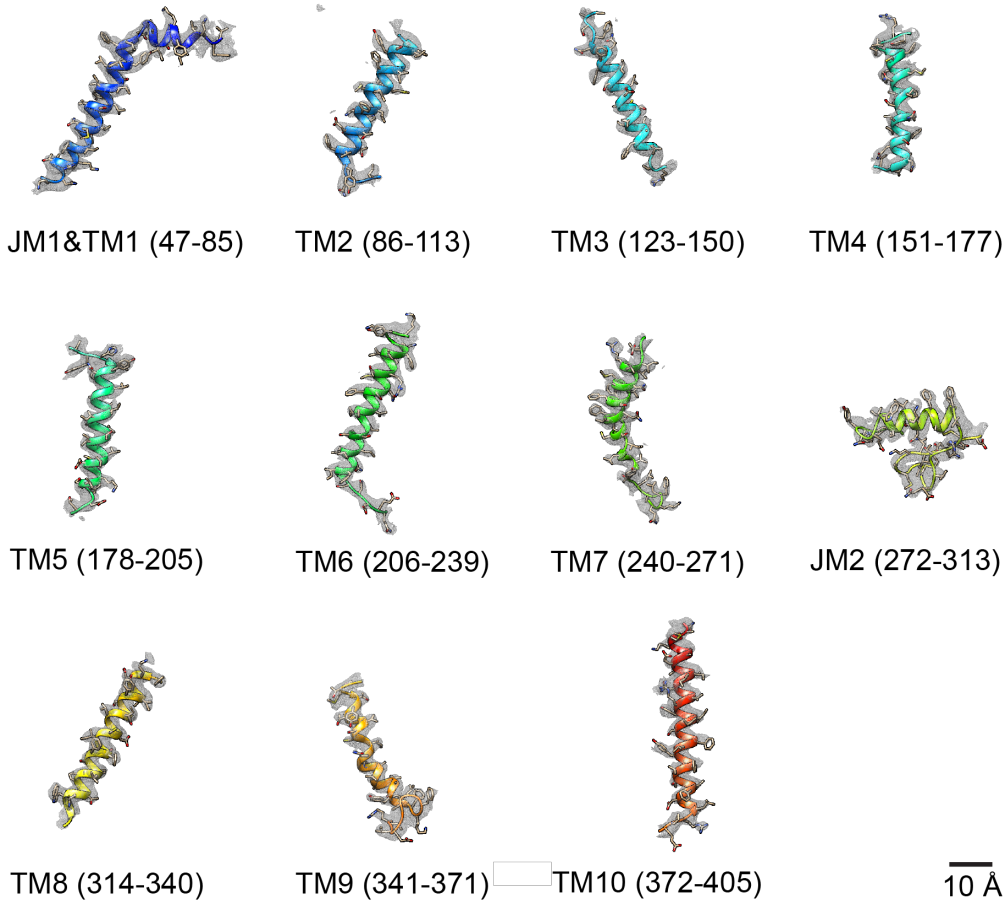

Extended Data Figure 5 | Fit of cryo-EM density with model. Cryo-EM densities (mesh) are superimposed with TM and JM helices of the PfCRT model. The model is rendered as a cartoon, colored in rainbow.

Extended Data Fig. 6

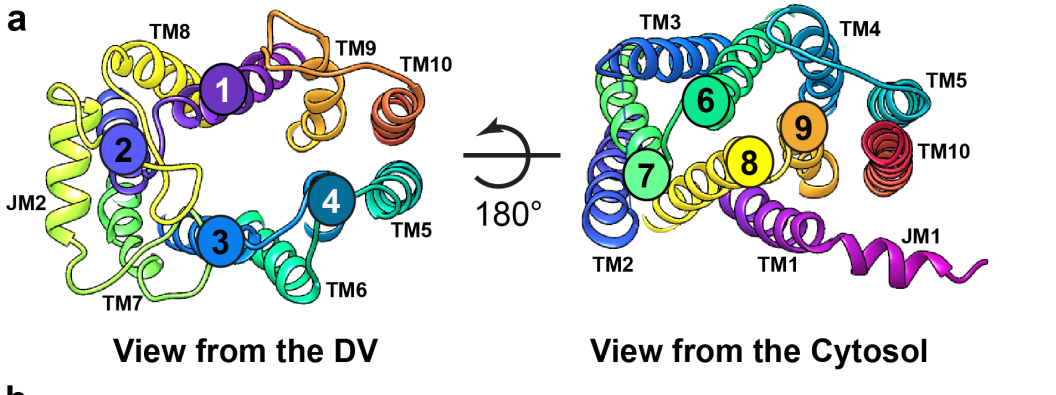

b

```
                TM1                                                 TM2
TM1-4___  ---LIFKEIKDNIFIYILSIIYLSVSVMNTIFAKRTINKIGNY-SFVTSETHNFICMIMFFIVYSL-FG
TM6-9___  FETQEENSIIFNLVL-ISSLI--PVCFSN-M-TRE-I-VFKKYKIDILRLNAMVSFFQLFTSCLILGMA
                TM6   *  *    * * *   *   *          TM7*         *     *

                      TM3                                 TM4
TM1-4___  NKKGNSKERHRSFNLQFFAISMLDACSVILAFIGLTRTTGNIQSFVLQLSIP-INMFFCFLILR-YRYH
TM6-9___  KLCDDCDGAWKTF-ALFSFFDICD--NLITSYI-IDKFSTMTYTIVSCIQGPALAIAYYFKFLAG----
                TM8*   *      *    *   *          TM9*     *       *  *
```

```
Sequence identity: 11.9%
Matched Positions: 72.5%
```

Extended Data Figure 6 | Symmetrical arrangement in inverted topology repeats of PfCRT. **a,** View of PfCRT from opposite directions of the DV and cytoplasm, with labeling of the four helices that are closest to the center (thus contributing to the cavity). **b,** AlignMe[71-73] sequence alignment between the two structural repeats within this pseudo-symmetric transporter reveals a high degree of sequence conservation, with each helix lining up with its corresponding helix from the pseudo-repeat. Residues 1-50 (N-terminus and JM1), 181-202 (TM5), 262-303 (JM2) and 368-424 (TM10 and C-terminus) were removed when doing the alignment. Helices are colored as per **Fig. 1**.

Extended Data Fig. 7

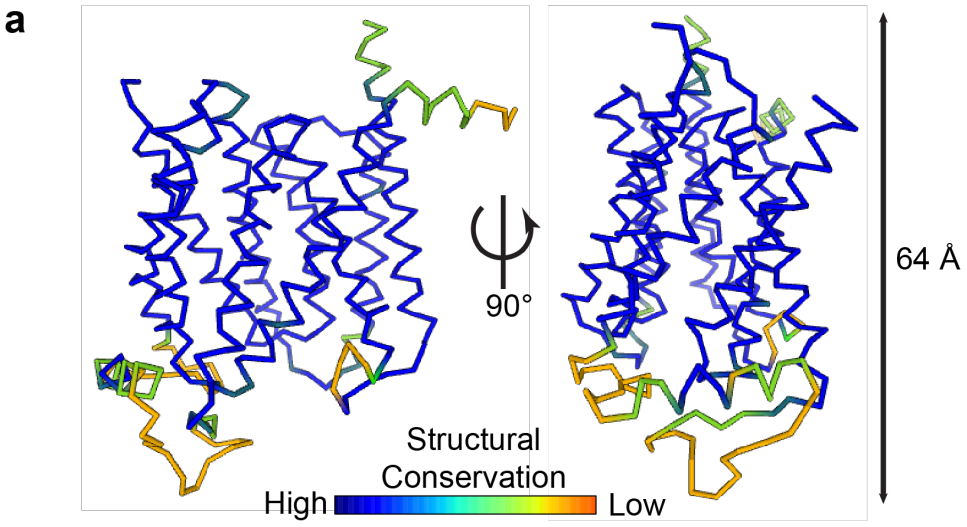

Extended Data Figure 7 | Structural comparison of PfCRT with other DMT superfamily members. a, Structural conservation of PfCRT compared with its DMT family members Vrg4 (PDB ID: 5OGE;[17]), YddG (PDB ID: 5I20;[18]) and TPT (PDB ID: 5Y78;[19]), generated using the Dali server[68]. **b,** Electrostatic representation of slices revealing the cavities of these four proteins in their solved structural states. Note the highly negatively charged (red) residues in the PfCRT cavity, contrasting with the positively charged (blue) or neutral residues in the other DMT transporters. Ligands for the non-PfCRT transporters are shown in a ball and stick representation.

Extended Data Fig. 8

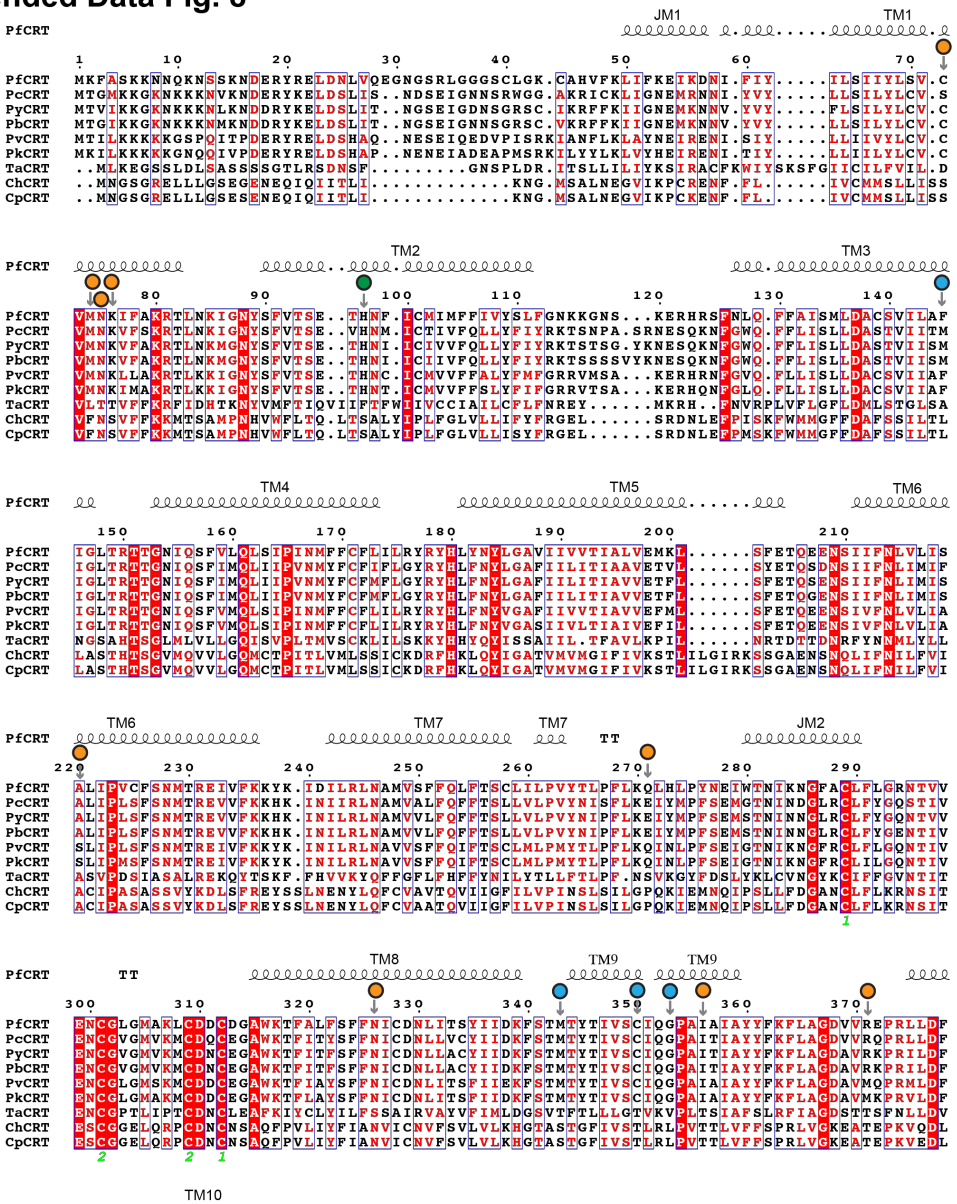

Extended Data Figure 8 | Sequence alignment and secondary structure of PfCRT. Sequences of different PfCRT isolates and other CRT homologs aligned using MUSCLE[70] and displayed using ESPript[74]. Sequences of nine orthologs of CRT in other *Plasmodium* or other Apicomplexan parasites were obtained from OrthoMCL-DB[69]. The sequences used are *Plasmodium falciparum* PfCRT strain 3D7 (the canonical wild-type sequence; UNIPROT Q9N623), *P. chabaudi* CRT strain chabaudi (PcCRT, Q7Z0V9), *P. yoelii* CRT strain 17XNL (PyCRT; Q7REK3) *P. berghei* CRT strain ANKA (PbCRT, Q9GSD8), *P. vivax* CRT strain Sal-1 (PvCRT, Q9GSD3), *P. knowlesi* CRT strain H (PkCRT; Q9GSD7); *Theileria annulata* CRT

strain Ankara (TaCRT, Q4UDS9); *Cryptosporidium hominis* CRT strain TU502 (ChCRT; RefSeq XP_666698); *Cryptosporidium parvum strain* Iowa II (CpCRT; XP_627815). The secondary structure of PfCRT is shown as a cartoon above the alignments, along with the positioning of the variant residues indicated in **Extended Data Fig. 1** (with same color scheme). The cysteine residues that likely form disulfide bonds are shown as green colored numbers below the alignment. Residues conserved (i.e. identical or similar) in at least 6 of 9 species are indicated in bold red text. Residues conserved in all species are in white text with red highlighting. None of the mutations associated with CQ or PPQ resistance mapped to residues that are fully conserved.

Extended Data Fig. 9

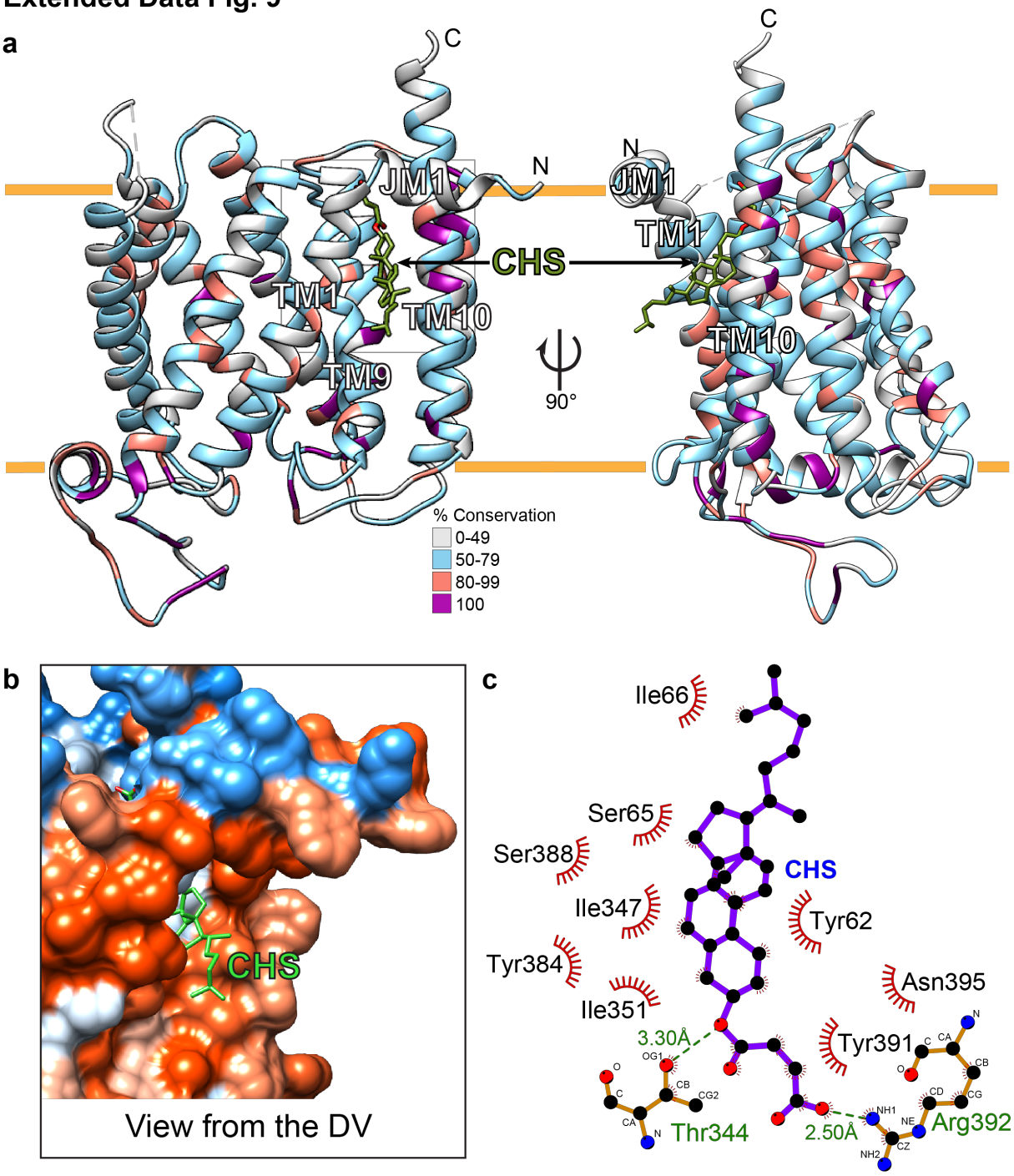

Extended Data Figure 9 | Binding cleft of cholesterol hemisuccinate (CHS) in PfCRT. a, A cleft formed by JM1, TM1, TM 9 and TM10 in the PfCRT demonstrates the binding of CHS (colored in olive green) in the PfCRT. PfCRT is colored based on conservation. **b,** PfCRT is rendered as surface colored by hydrophobicity, from orange (hydrophobic) to blue (hydrophilic). **c,** 2D diagram of CHS-PfCRT interaction generated using LigPlot[+78].

Extended Data Fig. 10

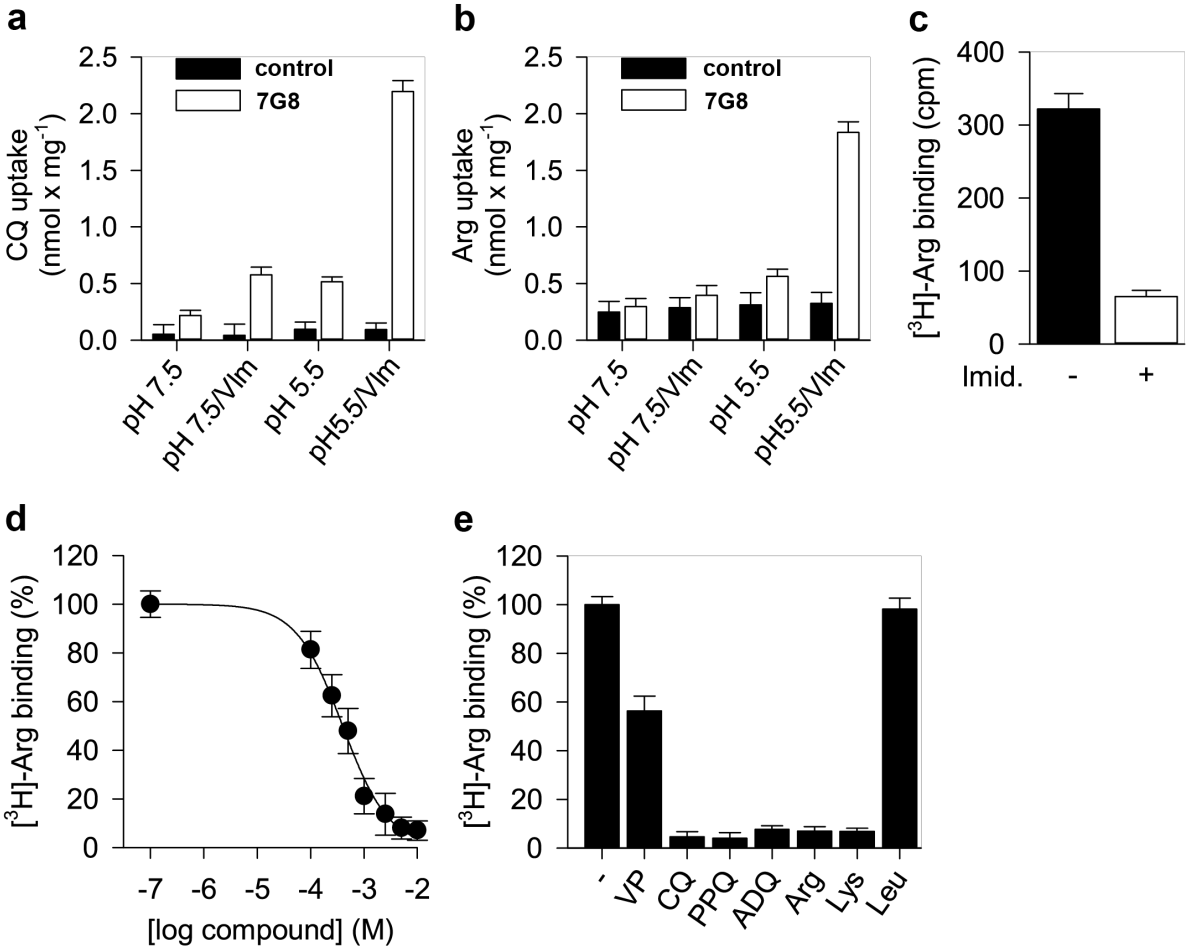

Extended Data Figure 10 | Binding and Transport Assays for PfCRT 7G8. a and **b**, one minute uptake for **(a)** 370 nM [^{3}H]-CQ or **(b)** 250 nM [^{3}H]-Arg were determined with PfCRT 7G8-containing proteoliposomes preloaded with 100 mM KP_i, pH 7.5 diluted in buffer composed of 50 mM Tris/MES, pH 5.5 or 7.5 ± the K^+ ionophore valinomycin (5 µM). The valinomycin (Vlm)-mediated K^+ efflux proceeding down its concentration gradient generated an inside-negative membrane potential. Empty liposomes lacking PfCRT 7G8 served as controls. Data are mean±SEM (N,n=2,3). **c,** Total binding of 125 nM [^{3}H]-Arg to 100 ng of nanodisc-incorporated PfCRT 7G8 was measured in the absence (-) or presence (+) of 800 mM imidazole (which competes with the His-tagged PfCRT 7G8 isoform for binding to the copper-coated YSi SPA beads). Data are mean±SEM (N,n=3,3). **d,** Isotopic dilution of 125 nM [^{3}H]-Arg with non-radiolabeled Arg revealed a LogEC_{50} value of -3.401 ± 0.03254 M (corresponding to 397.2 µM). We note that the primary source of Arg in parasitized red blood cells (RBCs) is from the proteolysis of Hb, which in its native state as a tetramer is present at 5 mM in RBCs[79]. **e,** Binding of 125 nM [^{3}H]-Arg in the presence or absence of 10 µM verapamil (VP), 1 µM CQ or PPQ, 0.1 µM amodiaquine (ADQ), or 1 mM Arg, Lys or Leu. Data in panels **d** and **e** are shown as mean±SEM (N,n=3,3) values and are normalized to the signal in the absence of the respective non-radiolabeled compound.

Supplementary References

16. Dominik, P.K. et al. Conformational chaperones for structural studies of membrane proteins using antibody phage display with nanodiscs. *Structure* **24**, 300-309 (2016).
17. Parker, J.L. & Newstead, S. Structural basis of nucleotide sugar transport across the Golgi membrane. *Nature* **551**, 521-524 (2017).
18. Tsuchiya, H. et al. Structural basis for amino acid export by DMT superfamily transporter YddG. *Nature* **534**, 417-420 (2016).
19. Lee, Y. et al. Structure of the triose-phosphate/phosphate translocator reveals the basis of substrate specificity. *Nat Plants* **3**, 825-832 (2017).
24. Quick, M. & Javitch, J.A. Monitoring the function of membrane transport proteins in detergent-solubilized form. *Proc Natl Acad Sci USA* **104**, 3603-3608 (2007).
35. Assur, Z., Hendrickson, W.A. & Mancia, F. Tools for coproducing multiple proteins in mammalian cells. *Methods Mol Biol* **801**, 173-187 (2012).
36. Kawate, T. & Gouaux, E. Fluorescence-detection size-exclusion chromatography for precrystallization screening of integral membrane proteins. *Structure* **14**, 673-681 (2006).
37. Goehring, A. et al. Screening and large-scale expression of membrane proteins in mammalian cells for structural studies. *Nature protocols* **9**, 2574 (2014).
38. Gibson, D.G. et al. Enzymatic assembly of DNA molecules up to several hundred kilobases. *Nature methods* **6**, 343 (2009).
39. Paduch, M. et al. Generating conformation-specific synthetic antibodies to trap proteins in selected functional states. *Methods* **60**, 3-14 (2013).
40. Dominik, P.K. & Kossiakoff, A.A. Phage display selections for affinity reagents to membrane proteins in nanodiscs. *Methods Enzymol* **557**, 219-245 (2015).
41. Fellouse, F.A., Wiesmann, C. & Sidhu, S.S. Synthetic antibodies from a four-amino-acid code: a dominant role for tyrosine in antigen recognition. *Proceedings of the National Academy of Sciences* **101**, 12467-12472 (2004).
42. Fellouse, F.A. et al. High-throughput generation of synthetic antibodies from highly functional minimalist phage-displayed libraries. *Journal of molecular biology* **373**, 924-940 (2007).
43. Suloway, C. et al. Automated molecular microscopy: the new Leginon system. *Journal of structural biology* **151**, 41-60 (2005).
44. Lander, G.C. et al. Appion: an integrated, database-driven pipeline to facilitate EM image processing. *J Struct Biol* **166**, 95-102 (2009).
45. Scheres, S.H. RELION: implementation of a Bayesian approach to cryo-EM structure determination. *J Struct Biol* **180**, 519-530 (2012).
46. Kimanius, D., Forsberg, B.O., Scheres, S.H. & Lindahl, E. Accelerated cryo-EM structure determination with parallelisation using GPUs in RELION-2. *Elife* **5**, e18722 (2016).
47. Cheng, A. et al. High resolution single particle cryo-electron microscopy using beam-image shift. *Journal of Structural Biology* (2018).
48. Rice, W.J. et al. Routine determination of ice thickness for cryo-EM grids. *Journal of Structural Biology* (2018).
49. Zheng, S.Q. et al. MotionCor2: anisotropic correction of beam-induced motion for improved cryo-electron microscopy. *Nat Methods* **14**, 331-332 (2017).
50. Rohou, A. & Grigorieff, N. CTFFIND4: Fast and accurate defocus estimation from electron micrographs. *J Struct Biol* **192**, 216-221 (2015).
51. Zhang, K. Gctf: Real-time CTF determination and correction. *J Struct Biol* **193**, 1-12 (2016).
52. Voss, N., Yoshioka, C., Radermacher, M., Potter, C. & Carragher, B. DoG Picker and TiltPicker: software tools to facilitate particle selection in single particle electron microscopy. *Journal of structural biology* **166**, 205-213 (2009).
53. Punjani, A., Rubinstein, J.L., Fleet, D.J. & Brubaker, M.A. cryoSPARC: algorithms for rapid unsupervised cryo-EM structure determination. *Nat Methods* **14**, 290-296 (2017).
54. Grant, T. & Grigorieff, N. Automatic estimation and correction of anisotropic magnification distortion in electron microscopes. *Journal of Structural Biology* **192**, 204-208 (2015).
55. Grant, T., Rohou, A. & Grigorieff, N. cisTEM, user-friendly software for single-particle image processing. *Elife* **7** (2018).

56. Adams, P.D. et al. PHENIX: a comprehensive Python-based system for macromolecular structure solution. *Acta Crystallographica Section D: Biological Crystallography* **66**, 213-221 (2010).
57. Pettersen, E.F. et al. UCSF Chimera—a visualization system for exploratory research and analysis. *Journal of computational chemistry* **25**, 1605-1612 (2004).
58. Wang, R.Y.-R. et al. Automated structure refinement of macromolecular assemblies from cryo-EM maps using Rosetta. *Elife* **5**, e17219 (2016).
59. Emsley, P. & Cowtan, K. Coot: model-building tools for molecular graphics. *Acta Crystallographica Section D: Biological Crystallography* **60**, 2126-2132 (2004).
60. Stuwe, T. et al. Architecture of the nuclear pore complex coat. *Science*, aaa4136 (2015).
61. Chen, V.B. et al. MolProbity: all-atom structure validation for macromolecular crystallography. *Acta Crystallographica Section D: Biological Crystallography* **66**, 12-21 (2010).
62. Barad, B.A. et al. EMRinger: side chain–directed model and map validation for 3D cryo-electron microscopy. *Nature methods* **12**, 943 (2015).
63. Kucukelbir, A., Sigworth, F.J. & Tagare, H.D. Quantifying the local resolution of cryo-EM density maps. *Nature methods* **11**, 63 (2013).
64. Tan, Y.Z. et al. Addressing preferred specimen orientation in single-particle cryo-EM through tilting. *Nature methods* **14**, 793 (2017).
65. Rosenthal, P.B. & Henderson, R. Optimal determination of particle orientation, absolute hand, and contrast loss in single-particle electron cryomicroscopy. *J Mol Biol* **333**, 721-745 (2003).
66. Ludtke, S.J., Baldwin, P.R. & Chiu, W. EMAN: semiautomated software for high-resolution single-particle reconstructions. *Journal of structural biology* **128**, 82-97 (1999).
67. Voss, N.R. & Gerstein, M. 3V: cavity, channel and cleft volume calculator and extractor. *Nucleic Acids Res* **38**, W555-562 (2010).
68. Holm, L. & Laakso, L.M. Dali server update. *Nucleic acids research* **44**, W351-W355 (2016).
69. Chen, F., Mackey, A.J., Stoeckert Jr, C.J. & Roos, D.S. OrthoMCL-DB: querying a comprehensive multi-species collection of ortholog groups. *Nucleic acids research* **34**, D363-D368 (2006).
70. Edgar, R.C. MUSCLE: multiple sequence alignment with high accuracy and high throughput. *Nucleic acids research* **32**, 1792-1797 (2004).
71. Stamm, M., Staritzbichler, R., Khafizov, K. & Forrest, L.R. AlignMe—a membrane protein sequence alignment web server. *Nucleic acids research* **42**, W246-W251 (2014).
72. Stamm, M., Staritzbichler, R., Khafizov, K. & Forrest, L.R. Alignment of helical membrane protein sequences using AlignMe. *PloS one* **8**, e57731 (2013).
73. Khafizov, K., Staritzbichler, R., Stamm, M. & Forrest, L.R. A study of the evolution of inverted-topology repeats from LeuT-fold transporters using AlignMe. *Biochemistry* **49**, 10702-10713 (2010).
74. Robert, X. & Gouet, P. Deciphering key features in protein structures with the new ENDscript server. *Nucleic acids research* **42**, W320-W324 (2014).
75. Miller, K.R. et al. T cell receptor-like recognition of tumor *in vivo* by synthetic antibody fragment. *PLoS One* **7**, e43746 (2012).
76. Wu, T.T. & Kabat, E.A. An analysis of the sequences of the variable regions of Bence Jones proteins and myeloma light chains and their implications for antibody complementarity. *J Exp Med* **132**, 211-250 (1970).
77. Hohn, M. et al. SPARX, a new environment for Cryo-EM image processing. *Journal of structural biology* **157**, 47-55 (2007).
78. Wallace, A.C., Laskowski, R.A. & Thornton, J.M. LIGPLOT: a program to generate schematic diagrams of protein-ligand interactions. *Protein Eng* **8**, 127-134 (1995).
79. Francis, S.E., Sullivan, D.J., Jr. & Goldberg, D.E. Hemoglobin metabolism in the malaria parasite *Plasmodium falciparum*. *Annu Rev Microbiol* **51**, 97-123 (1997).

Chapter 4 ON-GOING STUDIES AND FUTURE DIRECTIONS

4.1 Introduction

The structure of PfCRT 7G8 is a powerful tool that can be used to study the molecular determinants of anti-malarial drug binding and transport mechanisms. It also provides a structural basis for the investigation of clinical drug resistance and allows for greater understanding and foresight in the emerging global resistance landscape. We integrated structural, functional, and genetic approaches of three laboratories at Columbia University Irving Medical Center (Mancia lab, Fidock lab and Quick lab) to establish a transformative platform to study PfCRT at the molecular and atomic levels. These developments were made possible by the heterologous expression and purification of different PfCRT isoforms, Fab technology, and cryo-EM based structural studies. We now can biochemically characterize substrate binding and transport properties in purified or liposome reconstituted forms of PfCRT and test hypotheses about resistance conferring mutations and their drug susceptibility in genetically edited Pf cultures.

Here, I will discuss how we can leverage our recent structure to further study the molecular interactions of PfCRT and the mechanism of antimalarial drug resistance. I will describe both ongoing and long-term goals.

4.2 Investigating the physiological function of PfCRT

The structural and functional studies of PfCRT CQ-resistant 7G8 isoform reveal that an arginine is a putative substrate in CQ-resistant isoforms which is consistent with data in previous literature [56]. Based on our observation that arginine is a possible substrate, we performed a

scintillation-based proximity assay (SPA) on the purified PfCRT 7G8 reconstituted into nanodiscs probed with radiolabeled arginine in the absence or presence of other amino acids to see what other amino acids might display binding interaction. Binding of [^{3}H]-Arg was competitively inhibited in the presence of non-radiolabeled arginine, lysine and glutamate (**Figure 4.1**) suggesting that these three amino acids are likely to interact with PfCRT 7G8. Based on the observation in which arginine in the hypervariable region of the CTC Fab stabilizing the PfCRT 7G8-CTC Fab complex, we initially hypothesized that positively charged substrates may interact with PfCRT CQ-resistant isoforms. Data showing interaction of arginine and lysine with PfCRT are consistent with this proposition. However, glutamate interactions with the protein were unexpected.

Glutathione, a molecule made of three amino acids L-γ-glutamate, L-cysteinyl and glycine, is a cellular antioxidant that has been implicated in CQ resistance by which higher cellular levels of glutathione enhance CQ resistance [66]. There are two possible explanations on the association between glutathione and CQ response [105]. First, the glutathione could reduce the accumulation CQ, by which glutathione binds to heme and thus prevents from CQ binding to heme. Second, glutathione might encounter the oxidative damage resulted in heme degradation, from which *Plasmodium* parasites could possibly become more resistant to CQ [105]. However, there is no definitive understanding of the relationship between glutathione and CQ resistance. Strikingly, glutathione diminished the bindings of both Arg and CQ in its reduced form (GSH) and completely inhibited their bindings in its oxidized form (GSSG) (**Figure 4.1**). This finding raises a possibility that glutathione could be a natural substrate for PfCRT, and further implicates PfCRT has an important role in drug resistance. Our results are consistent with the previous hypothesis in that glutathione could be a natural substrate for PfCRT under

physiological condition [67] and may be a peptide transporter [55, 56]. To further explore the role of PfCRT with glutathione, we will measure the transport activity of glutathione in our proteoliposome experiment using radiolabeled GSH and GSSG.

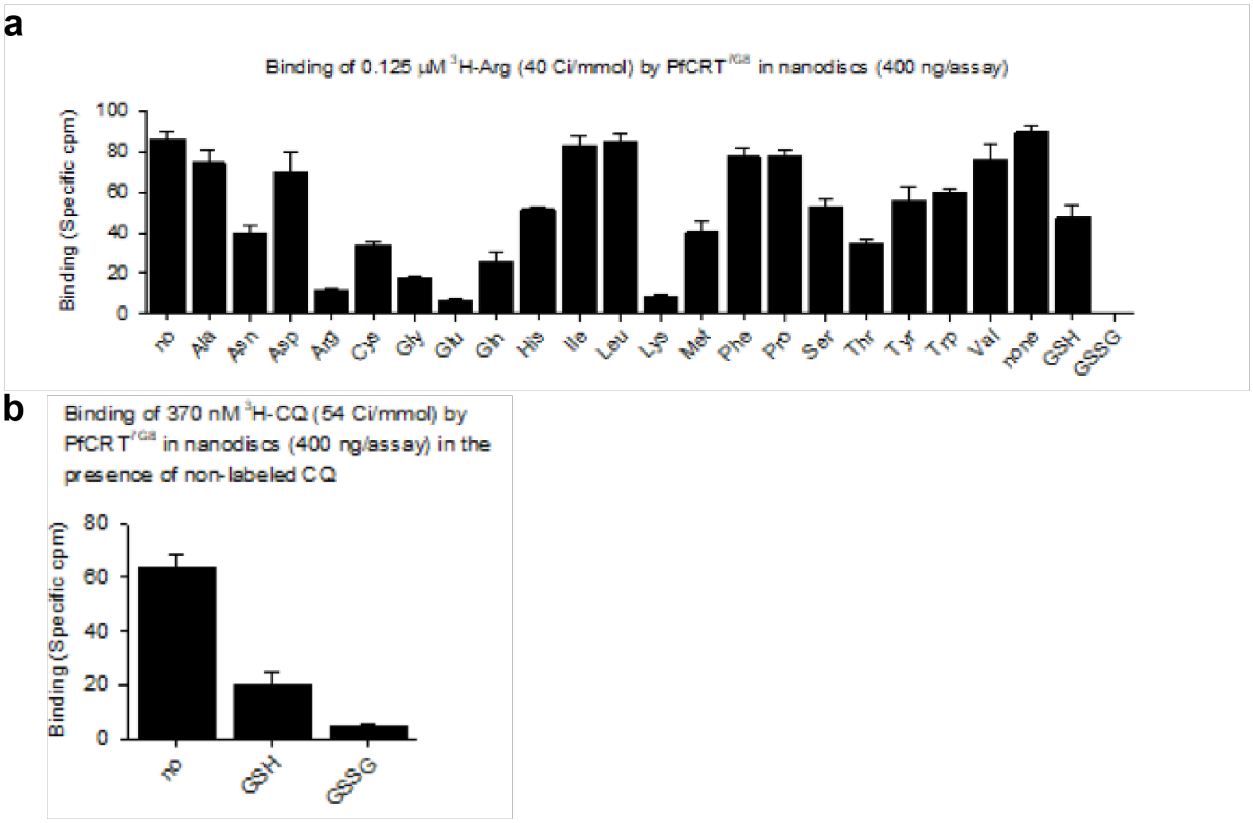

Figure 4.1 Substrates of PfCRT 7G8 isoform. (a) Binding of [^{3}H]-Arg was competitively inhibited in the presence of non-radiolabeled various amino acids as well as both reduced and oxidized glutathione. **(b)** Binding of [^{3}H]-CQ was competitively inhibitied in the presence of glutathione in both reduced and oxidized forms.

PfCRT may also be involved as a redox sensor because it has four highly conserved cysteine residues in a loop extending to the DV between TM 7 and 8 which are likely to form two disulfide bonds (C289-C312 and C301-C309). However, the effects of a potential redox system of PfCRT in parasites remains unknown. To test whether this conserved region of cysteine residues is involved in the reodox capabilities of PfCRT, I have made two single

mutants (C289A and C301A) using site-directed mutagenesis. Also, I plan to make double mutant (C289 301A) to disrupt both disulfide bonds and investigate whether the mutants affect the transport activity of CQ or PPQ in either reduced or oxidized environments.

4.3 Elucidating the mechanism of PfCRT-mediated drug resistance

The structure of PfCRT 7G8 provides insights to investigate novel mutations that could arise to confer resistance to antimalarial drugs and define their impact on PfCRT-mediated drug transport. As discussed in **Section 1.6**, recently emerged mutations (H97Y, F145I, M343L and G353V in the Dd2 isoform and C350R in the 7G8 isoform) that confer resistance to PPQ while sensitizing CQ [39, 63] are located around the central cavity in our PfCRT 7G8 structure. To gain a better understanding of the functional characterization of drug resistant variants, we have created the F145I and C350R mutants in the 7G8 background using site-directed mutagenesis, and also expressed and purified CQ-sensitive wildtype HB3 and CQ-resistant Dd2 isoform in the same conditions as that of 7G8 described in the Methods section of manuscript in Chapter III for the measurement of binding and transport (**Figure 4.2**). To assess the impact of new mutations in drug resistance and transport mechanisms, we measured the efflux of radiolabeled CQ, PPQ, and Arg on the purified and reconstituted PfCRT variants into proteoliposome (**Figure 4.3**). Consistent with *pfcrt* edited Pf cultured lines [39, 63], both F145I and C350R mutants in a heterologous expression system reversed CQ transport while mediating the efflux of PPQ. This data implicates altered transport as the core feature driving isoform-specific resistance.

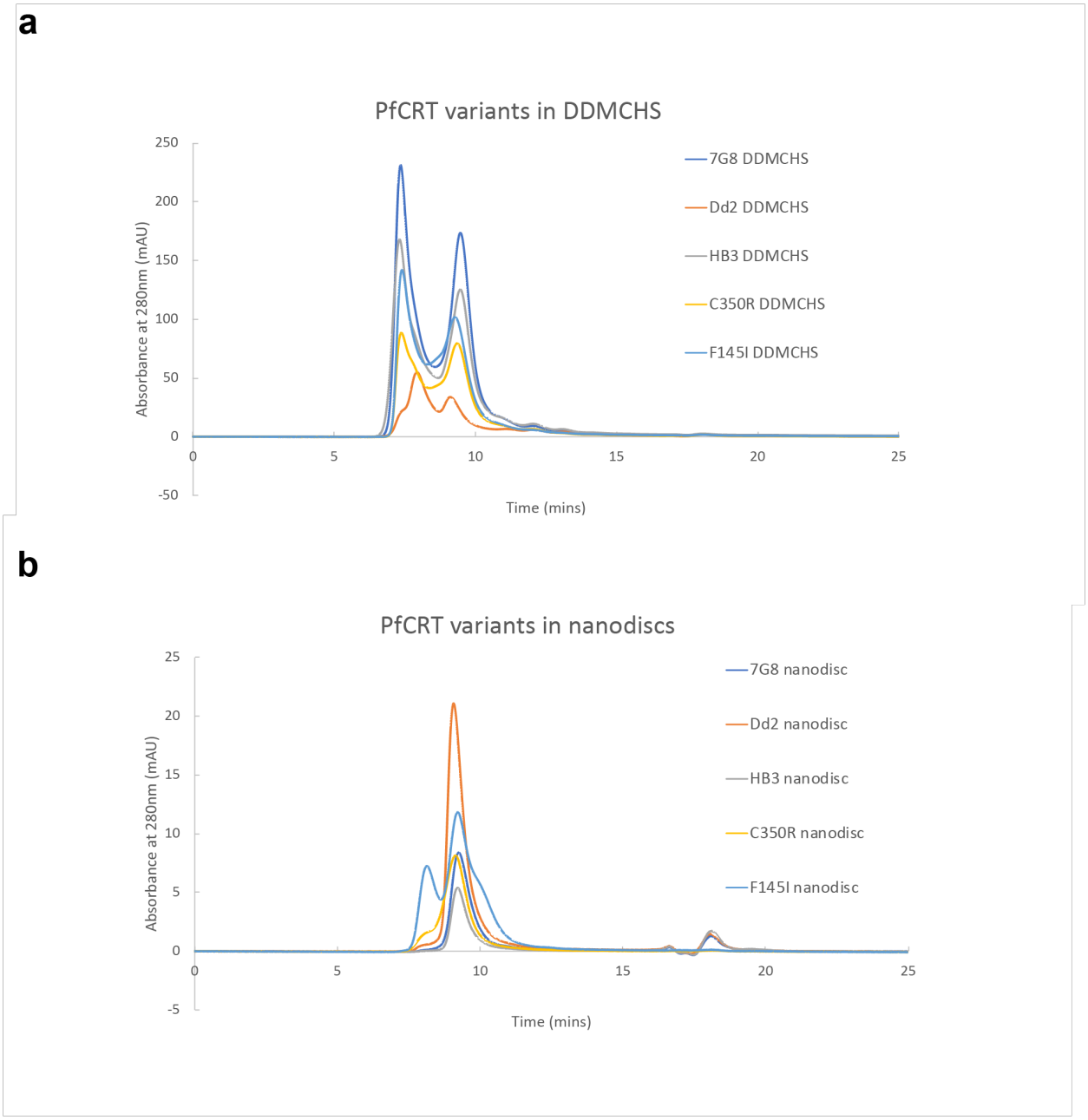

Figure 4.2 Purification of PfCRT variants. (a) Size-exclusion chromatography profiles of PfCRT 7G8, Dd2, HB3, 7G8 C350R, and 7G8 F145I nickel purified in DDMCHS and loaded onto Superdex 200 Increase 5/150 column. **(b)** Size-exclusion chromatography profiles of PfCRT variants reconstituted into nanodiscs.

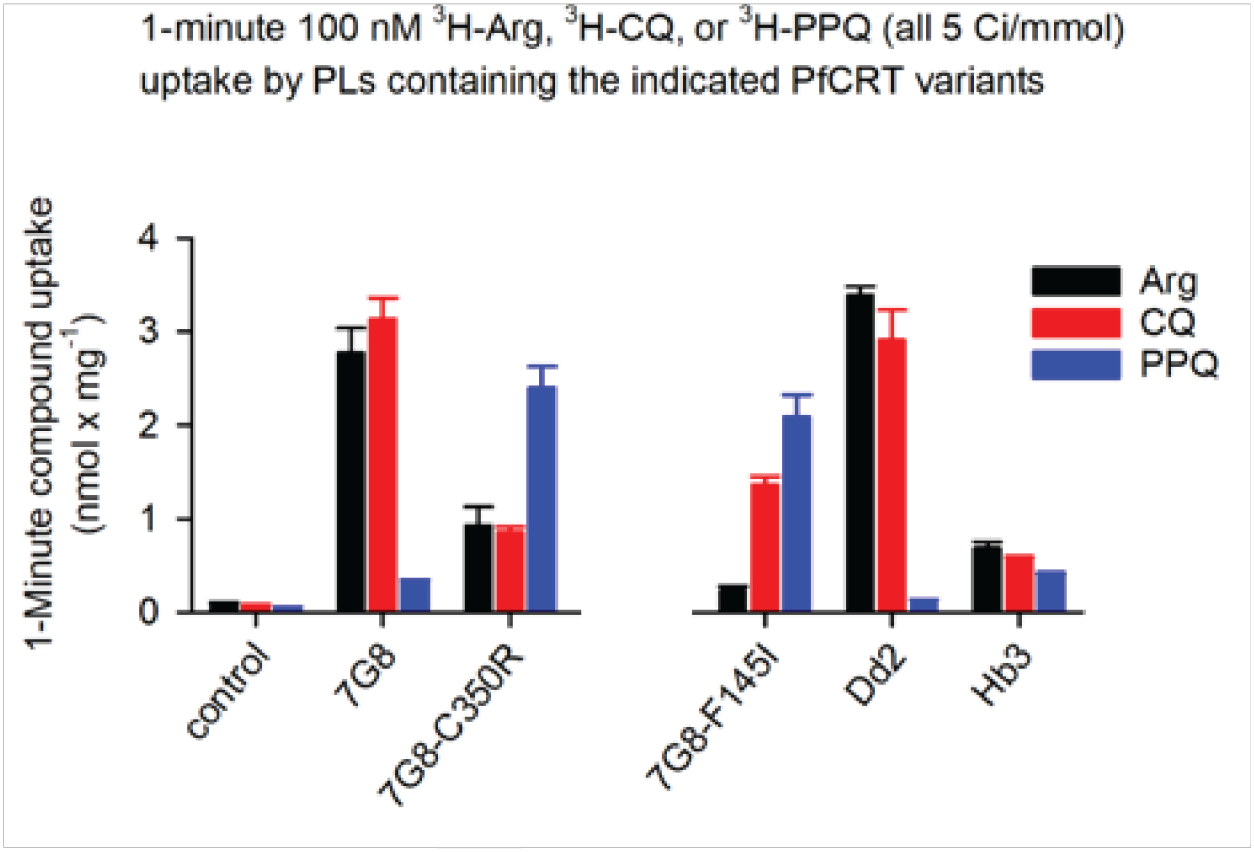

Figure 4.3 PfCRT variants uptake assay. One-minute uptake of 100 nM [^{3}H]-CQ, [^{3}H]-PPQ, or [^{3}H]-Arg was measured with PfCRT variants (7G8, Dd2, HB3, 7G8 C350R, and 7G8 F145I) reconstituted into proteoliposomes (PLs). Empty lipsome was served as a control.

4.4 Determining the structures of PfCRT 7G8 in complex with CQ and PPQ

Our PfCRT 7G8 structure displays a deep central cavity proposed as a putative ligand binding site, and we aim to obtain a structure of PfCRT 7G8 in complex with CQ and/or PPQ. However, the CTC Fab we used for our initial structural determination appears to compete with both CQ and PPQ. Therefore, we are currently reselecting new Fabs following the same Fab selection protocol in the presence of a saturation concentration of CQ or PPQ. So far, we have obtained 6 new Fabs (PTC #1, 2, 3, 4, 8, 11) using a phage display library from the Kossiakoff laboratory which seem to form complexes with PfCRT 7G8 while not interfering with CQ/PPQ

binding as shown by a shift during size-exclusion chromatography and from a SPA experiment respectively (**Figure 4.4**). The immediate next steps would be to screen the complex formation between PfCRT 7G8 and each Fab in cryogenic conditions with a FEI Tecnai F20 screening microscope in order for us to obtain a stable PfCRT-Fab complex and proceed in structural characterization of a drug bound state.

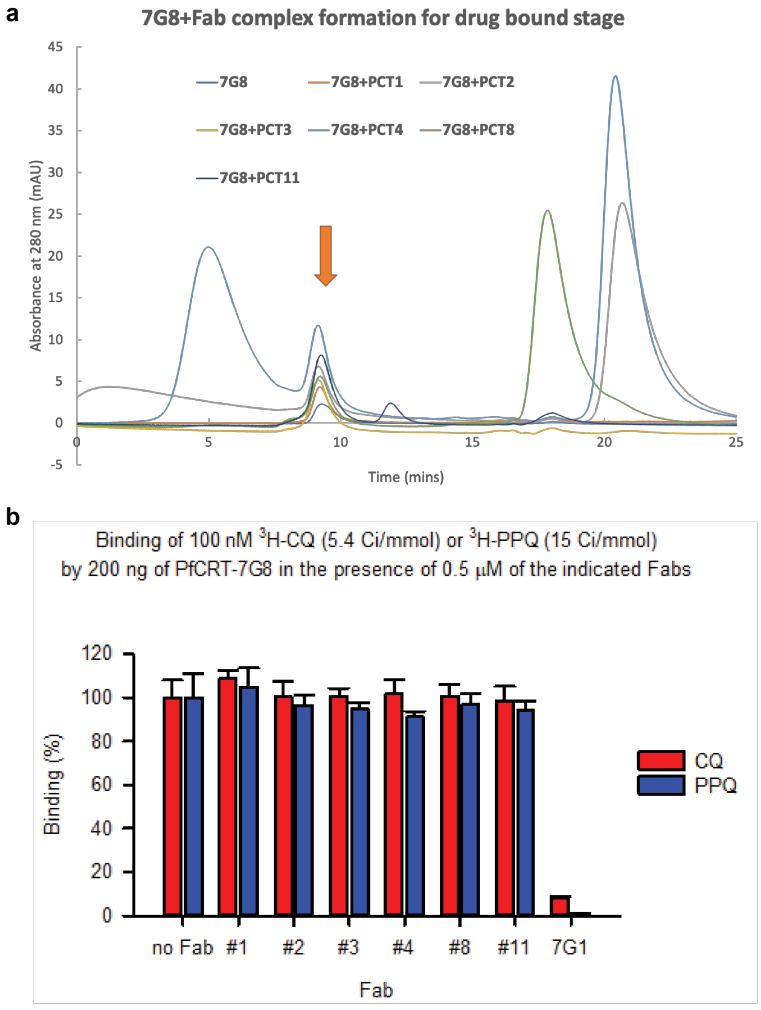

Figure 4.4 PfCRT 7G8 complex with PTC Fabs in the presence of drugs. (a) Size-exclusion chromatography profiles of PfCRT complexed with PTC Fabs selected from the screen of phage display library in the presence of saturated drug concentration. PfCRT in nanodisc sample was incubated with each Fab with 1:3 molar ratio and then loaded on to Superdex 200 Increase 5/150 column. Orange arrow indicates PfCRT±Fab. **(b)** Binding of 100nM [^{3}H]-CQ or [^{3}H]-PPQ was tested in competition with the presence of Fabs (PTC1, 2, 3, 4, 8, 11 and 7G1).

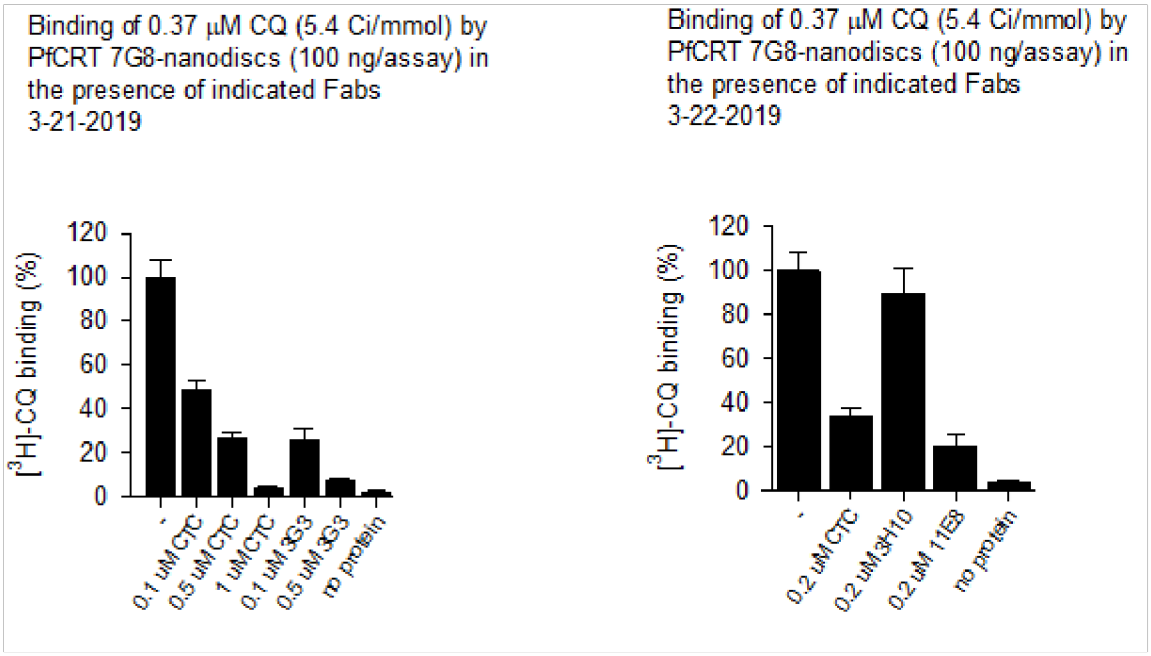

Figure 4.5 Competition binding assay between CQ and mouse monoclonal antibody Fabs. Competition of 370 nM [^{3}H]-CQ binding with Fabs generated from mice by Ilya Trakht. CTC Fab occupies the central cavity based on our initial structure of PfCRT 7G8 and was served as a control.

In parallel, we have been collaborating with Ilya Trakht in the Department of Medicine at Columbia University Irving Medical Center who generated mouse monoclonal antibody Fab fragments for PfCRT. We obtained four candidates (3G3, 3H10, 11E8 and 7G1) that form complexes with PfCRT 7G8, and biochemically tested whether each Fab competes with CQ binding (**Figure 4.5**). In results, we formed PfCRT 7G8-3H10 complex in the presence of CQ and collected images on the Titan Krios microscope at New York Structural Biology Center using the same parameters as the data collection that yielded our initial structural model. However, the dissociation between the protein and the Fab precluded us from obtaining a high enough number of particles to achieve a high-resolution density map. Still, the low-resolution density map allowed us to fit our initial model and we have learned that 3H10 Fab binds to the loop between TM 7 and 8 (**Figure 4.6**).

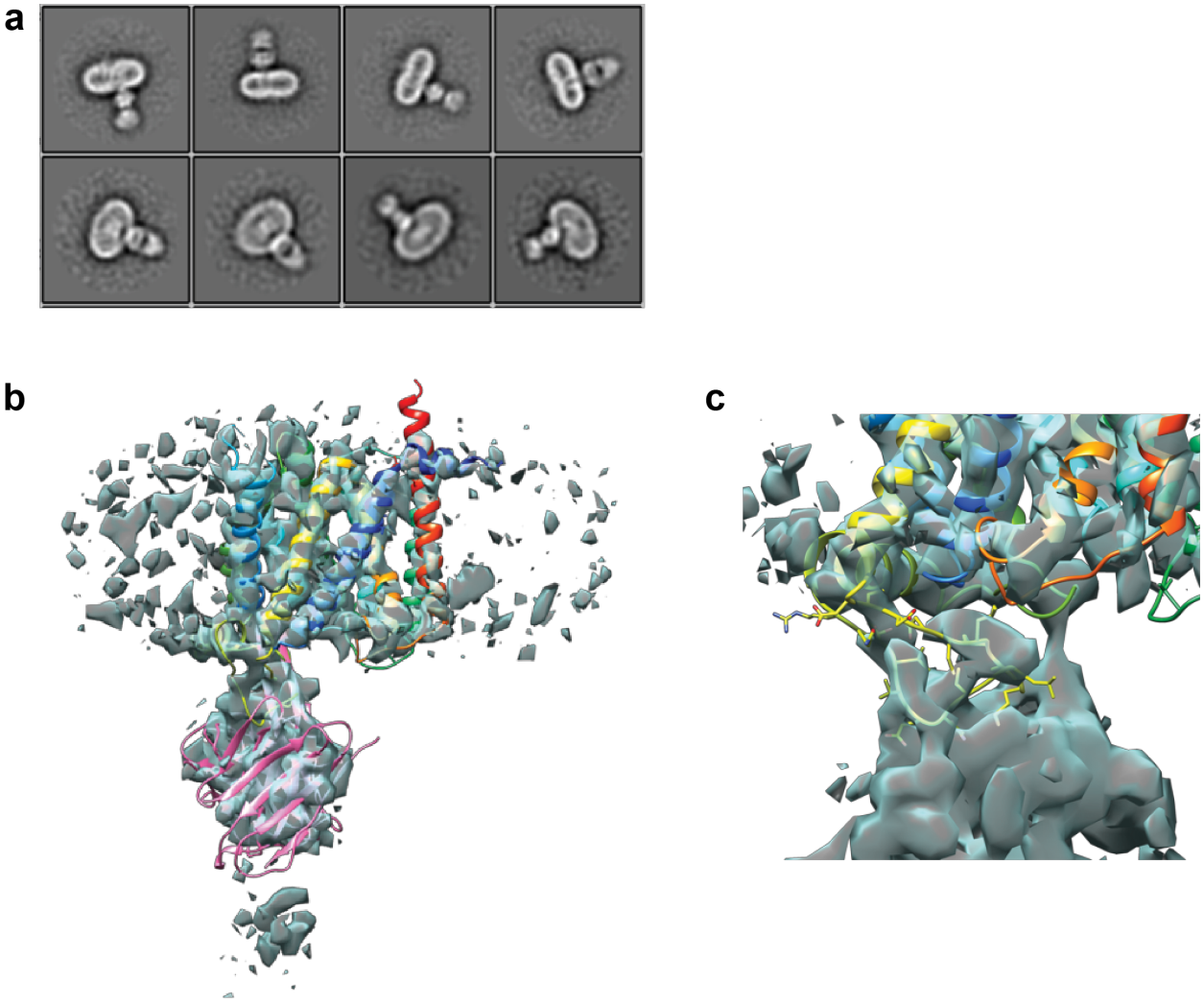

Figure 4.6 Cryo-EM analysis of the PfCRT+3H10 Fab complex. (a) Representative 2D class averages from Relion 2D classification. **(b)** Fit of the PfCRT+CTC Fab structural model into a low resolution cryo-EM density map of the PfCRT+3H10 Fab complex. The PfCRT 7G8 model is rendered as a cartoon and colored in rainbow. The CTC Fab is colored in pink. Low resolution density map of the PfCRT+3H10 complex shown in emerald green. **(c)** Close up view of electron density map indicating where 3H10 Fab interacts with the PfCRT 7G8.

As a third pathway to find the drug bound state, I am currently engineering a PfCRT fusion construct with apocytochrome b_{562}RIL (BRIL) domain [106] to extend the TM 10 based on our structural information, as the Kossiakoff lab at University of Chicago can provide us with anti-BRIL Fab to form a complex of PfCRT 7G8-BRIL with anti-BRIL Fab. BRIL has been used as a GPCR fusion protein to facilitate crystallization by extending hydrophilic surfaces which

promotes the formation of stable crystal contacts [106]. This could allow us to make the central cavity accessible for CQ or PPQ while the complex would be in the amenable size for cryo-EM analysis. A potential limitation of this approach is that extending the TM 10 helix with the BRIL domain could introduce structural flexibility hampering us from obtaining a high-resolution structure.

Defining the residues that interact with CQ and/or PPQ will enable us to predict novel mutations that could drive antimalarial resistance in geographically diverse PfCRT isoforms. As these mutations possibly evolve around the core or the entrance of the central cavity without affecting highly conserved residues across Apicomplexan CRT orthologs, we can perform molecular dynamic (MD) simulations and docking experiments to mutate these residues to investigate the changes in drug interaction. Based on MD simulations and docking scores, we can provide further experimental validation by examining both binding and transport of drugs on purified mutants. Based on the MD simulations and docking scores, we can then validate experimentally by examining both binding and transport of drugs on purified mutants.

4.5 Determining the structure of PfCRT 7G8 in other conformations

As with other DMT proteins, PfCRT consists of two inverted topology repeats, TM1-TM4 and TM6-TM9, suggesting that it is likely to have a similar alternating-access transport mechanism. To elucidate the mechanistic basis of PfCRT-mediated transport, we will attempt to capture and stabilize an outward-open conformation and other possible intermediate conformations. We will attempt to combine our Fab technology mentioned above with a random spherically constrained (RSC) single-particle cryo-EM approach, in which the PfCRT-Fab complex will be reconstituted into a uniformly sized liposome and frozen on a grid for EM

analysis. This method has been used to study the large conductance voltage- and calcium-activated potassium (BK) channels [107, 108].

Alternatively, we will also employ crosslinking and cysteine accessibility assays to determine the structure of the alternate conformation using the same Fab technology mentioned above. We propose to design various combinations of double cysteine mutants near the opening of PfCRT on the DV side. This approach has been used to investigate the mechanism of other transporters [109]. Both random spherically constrained single-particle cryo-EM and the crosslinking experiment could facilitate PfCRT transitioning from the inward to outward open state, allowing us to elucidate the mechanistic basis of how a substrate or drug is transported across the DV membrane.

4.6 Conclusions

PfCRT is an important molecule that mediates drug resistance in malaria. We present the structure of PfCRT with a putative binding site for antimalarial drugs, and provide evidence that drug resistance is associated with transport mechanism. Determining structures of PfCRT in complex with CQ and/or PPQ as well as in other conformations will be crucial to further elucidate the mechanism of CQ and/or PPQ resistance.

References

39. Ross, L.S., et al., *Emerging Southeast Asian PfCRT mutations confer Plasmodium falciparum resistance to the first-line antimalarial piperaquine.* Nat Commun, 2018. **9**(1): p. 3314.
55. Martin, R.E., et al., *Chloroquine transport via the malaria parasite's chloroquine resistance transporter.* Science, 2009. **325**(5948): p. 1680-2.
56. Juge, N., et al., *Plasmodium falciparum chloroquine resistance transporter is a H+-coupled polyspecific nutrient and drug exporter.* Proc Natl Acad Sci U S A, 2015. **112**(11): p. 3356-61.

63. Pelleau, S., et al., *Adaptive evolution of malaria parasites in French Guiana: Reversal of chloroquine resistance by acquisition of a mutation in pfcrt.* Proc Natl Acad Sci U S A, 2015. **112**(37): p. 11672-7.
66. Ginsburg, H., et al., *Inhibition of glutathione-dependent degradation of heme by chloroquine and amodiaquine as a possible basis for their antimalarial mode of action.* Biochem Pharmacol, 1998. **56**(10): p. 1305-13.
67. Patzewitz, E.M., et al., *Glutathione transport: a new role for PfCRT in chloroquine resistance.* Antioxid Redox Signal, 2013. **19**(7): p. 683-95.
105. Lehane, A.M., et al., *Degrees of chloroquine resistance in Plasmodium - is the redox system involved?* Int J Parasitol Drugs Drug Resist, 2012. **2**: p. 47-57.
106. Chun, E., et al., *Fusion partner toolchest for the stabilization and crystallization of G protein-coupled receptors.* Structure, 2012. **20**(6): p. 967-76.
107. Wang, L. and F.J. Sigworth, *Structure of the BK potassium channel in a lipid membrane from electron cryomicroscopy.* Nature, 2009. **461**(7261): p. 292-5.
108. Pang, S.S.B.-J., C.; Radjainia, M.; Spicer, B. A.; Law, R. H. P.; Hodel, A. W.; Ekkel, S. M.; Conroy, P. J.; Ramm, G.; Venugopal, H.; Bird, P. I.; Hoogenboom, B. W.; Voskoboinik, I.; Gambin, Y.; Sierecki, E.; Dunstone, M. A.; Whisstock, J. C., *The structure of Macrophage Expressed Gene-1, a phagolysosome immune effector that is activated upon acidification.* 2019.
109. Reyes, N., C. Ginter, and O. Boudker, *Transport mechanism of a bacterial homologue of glutamate transporters.* Nature, 2009. **462**(7275): p. 880-5.